EFFECTS OF LAYER BOUNDARIES ON FULL WAVEFORM ACOUSTIC LOGS

by

Benoit J. Paternoster

Ingénieur Civil des Mines
Ecole Nationale Supérieure des Mines de Paris
Paris, France
(1983)

SUBMITTED TO THE DEPARTMENT OF
EARTH, ATMOSPHERIC, AND PLANETARY SCIENCES
IN PARTIAL FULFILLMENT OF THE
REQUIREMENTS FOR THE DEGREE OF
MASTER OF SCIENCE

in

Earth and Planetary Science

at the

May , 1985

Signature of Author ....
Department of Earth, Atmospheric, and Planetary Sciences
May ,1985

Certified by ....
M. Nafi Toksoz
Thesis Advisor

Accepted by ....
Theodore R. Madden
Chairman
Departmental Committee on Graduate Students

EFFECTS OF FORMATION BOUNDARIES ON FULL WAVEFORM ACOUSTIC LOGS

by

Benoit J. Paternoster

Submitted to the department of Earth, Atmospheric and Planetary
Sciences on May, 1985 in partial fulfillement of the
requirements for the degree of Master of Science in Geophysics

Abstract

The first part of this thesis is concerned with reflection and transmission of acoustic waves at layer boundaries in boreholes. These scattering effects produce events that are oblique with respect to the main wavefield on iso-offset sections. Such events have been recorded by the full waveform acoustic logging tool EVA. Wave type conversions are also currently observed. Ray modeling reveals the sensitivity of the apparent velocity of such events to the dip angle of the interface. Two sections of real data are presented and interpreted : dip angles of the interfaces are estimated.

In thinly-bedded formations, the exact location and amplitude of velocity contrasts across boundaries are sometimes difficult to estimate. These features are greatly affected by the minimum spacing between the probe receivers. Improvements of the spatial resolution can be made, however, when the spatial sampling of the formation is less than the tool minimum spacing. The second part of this thesis proposes a recursive least squares inversion of travel times for formation slownesses based on the Kalman filter. This formulation emphasizes the noise content of the data as a factor limiting resolution. A data adaptive inversion scheme is also developped in order to sharpen large contrasts in formation properties. Results from synthetic data as well as real data processing are presented.

Thesis Supervisor : M.N. Toksöz
Title : Professor of Geophysics

à Brigitte et ...

Acknowledgements

I am indebted to my advisor, Professor M.N. Toksöz for allowing me to study in the rich and synergetic research environment of the Earth Resources Laboratory. His advice and insights were "adaptively" applied in the right direction and always at the right time and provided me with all the motivation necessary to complete this research.

I wish I could thank everyone personnally for the help,contribution, support, discussions on scientific and less scientific matters that enriched my stay at ERL.

Arthur Cheng's support and comments were helpful.

I thank Roger Turpening for the interest that he kindly shown for this study as well as for the many mechanical tips he gave me.

I thank Marc Larrère for providing me with the processed data used in chapter 2. His contribution is developped in appendix E.

My gratitude goes to Gilles Garcia for the many constructive discussions and continuous support especially throughout the third chapter of this thesis.

Many thanks go to Wafik Beydoun, Christophe Gonguet and Carol Blakway for their help and moral support.

Special thanks also go to Naida Buckingham for her kindly deciphering my "style" and turning it into readable scientific text.

I am particularely indebted to the company ELF AQUITAINE and its Well-Seismic Department. Beyond their administrative and financial support of which I am greatly appreciative, I would like to thank specially G. Henry, P. Staron, G. Arens and P. Arditty who made this "dream" come true and aroused my interest in Well-logging.

Finally, I wish to express my deep gratitude to my wife Brigitte for her continuous patience and the loving support she demonstrated for the strainuous rythm I and MIT imposed on our life throughout our stay.

This research was supported by the Full Waveform Acoustic Logging Consortium at the Earth Resources Laboratory. During this study, I was supported as a graduate fellow by ELF AQUITAINE

Table of Contents

Chapter 2. EFFECTS OF LAYER BOUNDARIES ON FWAL AND DIP ESTIMATION

CHAPTER 1 : INTRODUCTION

Acoustic wave propagation in a fluid-filled borehole has been extensively investigated by numerous authors (Biot, 1952, White and Zechman, 1968, Tsang and Rader, 1979, Cheng and Toksöz, 1981, Schoenberg and Marzetta, 1981). These studies succeded in describing and predicting the features of the wavetrain resulting from an impulsive source set on the borehole axis. Because of its sensitivity to the formation petrophysical parameters, Full Waveform Acoustic Logging tools proved to be very informative. The considerable amount of data provide very complete lithologic information. Recent developments extended investigations toward ever more complex borehole environments such as cased boreholes or permeable zones (Tubman, Cheng and Toksöz, 1984, Mathieu and Toksöz, 1984)

More recently, data recorded by the EVA tool from Société Nationale Elf Aquitaine (Production) showed that waves are scattered at acoustic discontinuities intersecting the borehole. Resulting events can be analysed in terms of reflection at and transmission through layer boundaries.

An important feature of these events is that some are their ability to be converted at interfaces from one wave type to another (i.e. P to S, S to P, Stoneley to S). Therefore, energy of individual modes, as can be deduced from the theory of propagation in homogeneous formation, is constantly re-distributed among all participating modes when propagating in a layered formation. For body waves, such phenomena cannot take place at interfaces intersecting the borehole normally. Therefore, an important part of the present study is to show the sensitivity of these events to the dip of the interface. The analysis shows that the dip of interfaces can be estimated from this information.

A simple and better-known example of transmission event is obtained when the propagation mode is preserved across layer boundaries when waves travel from source to receiver. Here, again, such phenomenon will be characterized by its apparent velocity as seen from the tool moving along the borehole. This apparent velocity strongly depends on the source receiver separation. In other words, the travel time of a given type of wave will not correspond to any of the individual layers travelled through but rather to a travel time average of all encountered layers.

In a second part a method to determine the velocities for individual layers is introduced. A reccursive least squares inversion of travel times for transit times (i.e. formation slowness) is proposed. The choosen formulation allows control over the depth resolution. It will be developped for single travel time determination tool and will be extended to incorporate multiple travel time determinations.

Although issues discussed in this work involve the same phenomena in essence, their study requires specific methods. Therefore, we choose to treat them under two separate chapters which will be formatted as two self- contained papers.

CHAPTER 2 : EFFECTS OF LAYER BOUNDARIES ON FULL WAVEFORM ACOUSTIC LOGS AND DIP ESTIMATION

Introduction

In September 1983, recordings were made in the Burch well in Michigan using the full waveform acoustic logging tool EVA of Societé Nationale Elf Aquitaine (Production). EVA is composed of 5 transmitters at the top spaced 25 cm apart. Twelve receivers are located below the transmitters, each separated by 1 meter. The uppermost receiver is 1 meter below the lowest transmitter. This original geometry achieves spacings between transmitter and receiver that range from 1 meter to 13 meters. The sources are fired in sequences of increasing spacing values. Shoots are triggered every 150 ms. The tool was run at the very slow speed of 6 ft per minute with only 12 combinations of transmitter and receiver, yielding a particularly dense spatial sampling of the formation. A convenient way to display the recorded data is to plot sections of only one combination of transmitter and receiver versus depth (see Figure 1). These iso-offset sections may be qualitatively read as conventional logs showing the various arrivals, headwaves (P and S), guided waves (pseudo-Raleigh and Stoneley), with their relative velocities and amplitudes. In addition, the records show rather unusual events: waves are scattered at the interfaces propagating with constant apparent velocities. Since they cut across the usual arrivals at an angle, these waves will be referred to as oblique arrivals. Figure 2 shows some examples from the Burch well. Such arrivals have been observed at other sites, (Koerperich, 1978; Serra, 1984). They are related to bed boundaries or other discontinuities intersecting the borehole. In this paper we study these events using ray theory.

An important aspect of these waves is that a P wave incident upon the interface has generated both P and S transmitted and reflected waves. Such a conversion cannot take place at a smooth boundary normal to the borehole. One explanation is that P to S conversion takes place because of the dip of the interface. The models we calculate show that both the generation of converted waves and the velocities of the "oblique" arrivals are sensitive to the dip. In fact dip can be calculated from oblique wave properties. In the next section we model the "oblique" arrivals using optical (high frequency approximation) ray theory. In the last section we analyze examples from the Michigan data and compare these with other logs.

1 Modeling oblique events

The generation of oblique events is related to acoustic discontinuities, either bed boundaries or fractures. First we use simple time-average representation to account for the slope of the events on iso-offset sections. This slope has the dimension of a velocity. We shall refer to it as an apparent velocity and use the notation v_a. Ray tracing provides us with a way to understand what is happening from the standpoint of arrival times. Amplitudes would be harder to determine, and this is not included in our present study. The source-receiver spacing is larger than a wavelength (a minimum of 1 m vs 30 cm), so that we can neglect near field effects. We shall also assume that Snell's law is applicable. Figure 3 shows the various geometric configurations of rays that are transmitted across and reflected at interfaces.

1.1 Horizontal interfaces

[A] Transmission across a bed boundary

In this case, the tool is astride the discontinuity. Only the waves transmitted through it are recorded. In the case of body waves, the direct arrivals are compressional waves emitted at the source in the borehole fluid and criticaly refracted in the formation. These travel as headwaves in the formation and are criticaly refracted back in the fluid to excite the receiver.

We now assume that a wave travelling in the formation with a velocity v_0 is converted at the interface into another type of wave travelling with a velocity v_1. This wave will arrive some time between the direct wave of velocity v_0 and the one of velocity v_1 such as P to S conversion. This conversion will give rise to an oblique event whose apparent velocity is :

$$v_a = (v_1^{-1} - v_0^{-1})^{-1} \tag{1}$$

Note that the apparent velocity is independent of the source receiver separation.

This phenomenon is somewhat similar to what happens at a sharp boundary between two different lithologies; the tool averages the velocities over its length and the record shows a linear gradient. The apparent velocity obeys the same formula as above. In this case no conversion occurs and the same type of wave is propagated through at a different velocity.

One should note that this phenomenon may yield very high apparent velocities. Let us consider, for instance, the case of a boundary between a carbonate with v_p = 22 kft/s and v_s = 12 kft/s and an evaporite such that v_p = 14.5 kft/s and v_s = 9 kft/s. In this situation the event will have a slope ($dz/dt = (1/v_0 - 1/v_1)^{-1}$) of 42.5 kft/s for the P to P wave transmission event and of 36 kft/s for the S to S wave event. Moreover, a conversion from P to S wave will have an apparent velocity of 15.2 kft/s, whereas the reverse, from S to P wave will reach a tremendous 69.6 kft/s.

[B] Reflection on a bed boundary

When the tool is completely above or below the interface, some of the rays are reflected back to the receiver. These waves are delayed relative to those following the direct path. With the geometry shown in Figure 3 the extraneous path travelled by the reflected waves is twice the separation between receiver and reflector, thus the apparent velocity is

$$v_a = v_0/2. \tag{2}$$

Since we shall discuss dipping interfaces later, let us consider the situation where a conversion occurs at the boundary. In that case, half of the path is travelled at v_0 and the other half at v_1, the velocity of the converted wave. Thus, the apparent velocity will be:

$$v_a = (v_1^{-1} + v_0^{-1})^{-1} \tag{3}$$

[C] General pattern

To illustrate the oblique events, we consider a simple geometry with one source and one receiver only. Let us consider a single horizontal interface as shown in Figure 4. As the tool moves toward and across the interface, different sets of transmitted and reflected events are generated.

When the recording tool is run up the hole, with the transmitters at the top of the tool, the source meets the discontinuity first. Before the source reaches the discontinuity the receiver sees only the direct arrivals and the reflections. When the transmitter is above the interface, the raypaths cross the interface. When the tool has been moved an amount equal to the spacing, the receiver is then above the discontinuity and reflections can occur again. Thus, from a single interface, two events will appear on the section at two separate depths when the depth interval is equal to source-receiver distance. Hence, on iso-offset sections, reflections will give rise to two symmetric patterns, a tool length apart, amidst which transmission patterns may be seen.

Oblique events start at discontinuities or at a tool length from discontinuities. To start an interpretation, one must look for paired events and locate the discontinuity. To do so, it is advantageous to compare sections with various spacings and correlate other logs with a section. One can discriminate between reflection and transmission and address the right model. We now understand that a single heterogeneity may give rise to a large number of oblique events, even when only a restricted number of wave types are involved. The theoretical pattern for two waves is shown in Figure 4.

1.2 Dipping interfaces

Dipping interfaces considered hereafter are plane interfaces intersecting the borehole with an angle α with respect to the vertical. We shall denote apparent theoretical velocities computed for horizontal interfaces with v_{90} and those for dipping interfaces with v_a.

[A] Transmission

Transmissions with conversion on a dipping discontinuity are modelled using simple ray theory. The details of the model are given in Appendix A.

A useful parameter is $V = v_0/v_1$. In the appendix calculations were carried out only for the case V < 1. In this case transmission occurs on the part of the plane nearest to the transmitter. This is the geometrical configuration displayed in Figure A-1. These results can be transposed to the case where V > 1. In this situation the geometry is that of the previous case where receiver and transmitter have been interchanged and the raypaths reversed. The travel time curve and apparent velocity remain the same.

For the geometry shown in Figure A-1 we consider two cases:

1) $V < \cos\alpha$. Over the span of the tool the arrival time of the transmitted wave varies between t_0, arrival time of the quickest body wave considered, and t_2 ,

$$\frac{t_2}{t_0} = V\cos\alpha + \sqrt{1 - V^2}\sin\alpha \tag{4}$$

The apparent velocity varies slowly with the position of the tool and one can approximate its value, v_a, with the following formula :

$$\frac{v_{90}}{v_a} = \frac{V\cos\alpha + \sqrt{1 - V^2}\sin\alpha - V}{1 - V} \qquad (5)$$

2) $V \geq \cos\alpha$ In this case, the situation is much the same as for a horizontal interface.

$$v_a = v_{90}$$

Those results are presented in Figure 5 as well as in Figure A-2. One should remember that, unless we deal with waves such that $\cos\alpha < v_0/v_1 < 1/\cos\alpha$, a dipping interface will increase the apparent velocity of any transmitted wave. In the case of conversion from P to S wave or vice versa, this phenomenon should only appear for values of α less than 55° , meaning a dip angle greater than 35°, if formation Poisson's ratio is $\nu = 0.25$ or $v_p/v_s = \sqrt{3}$.

[B] Reflection without conversion

Again, the tool is completely above or below the discontinuity. We modeled this case in Appendix B using the simple geometry of Figure A-3. An exact analytical solution can be worked out. As opposed to the horizontal interface case, the apparent velocity is now a function of the distance to the reflector and the dip angle. A useful parameter is obtained by scaling the vertical distance to the source receiver separations, let us then define z=Z/S. The angle α is taken with respect to the vertical.

$$\frac{v_a}{v_{90}} = \frac{\sqrt{1 + 4z(z-1)\sin^2\alpha}}{(2z-1)\sin^2\alpha} \qquad (6)$$

The travel time curves are non-linear, but their curvatures are small for small dips. The apparent velocity varies very quickly with dip angle. This phenomenon may yield very high apparent velocities, up to five times the formation velocity for an angle of $\alpha = 20^\circ$. Figure 6 presents a plot of v_a / v_{90} versus α. Figurè A-4 displays identical plots for various values of z. These curves are located between the curves $1/\sin\alpha$ and $1/\sin^2\alpha$, corresponding to the limiting cases of $z = \infty$ and $z=1$.

We shall take advantage of the sensitivity of the apparent velocity for the dip angle to determine dips. From the previous remarks, we expect to have a good angle resolution for medium to large dip angles.

[C] Reflections with conversion

A body wave travelling in the formation at the velocity v_0 impinges on a plane boundary, dipping from the vertical with an angle α, and is reflected back toward the receiver with the velocity v_1. Convenient parameters are $V = v_0 / v_1$ and z, the vertical distance from the source to the discontinuity normalized with respect to the source-receiver spacing, S. This case is modeled in Appendix C.

We computed the arrival time and apparent velocities in the situation where the tool is completely above the discontinuity. Using the symmetry of the problem, we can transpose the results to the situation where the tool is below the discontinuity at a distance $z < 0$ from it. In such a case, the results are similar to those in the previous case obtained for the parameters 1/V and 1 - z. That is : $v_a(\alpha,V,z) = v_a(\alpha,1/V,1-z)$. The general behavior of the apparent velocity is very similar to the case of reflection without conversion. Let us look at two cases.

1) $V < \cos\alpha$. In this situation, when the tool is completely above (or below) the discontinuity, the reflected wave arrives at the receiver along the interface at time t_2, as defined in equation (5), earlier than the direct arrival. The reflection point is some distance from the borehole. As the tool is pulled up, the reflection point moves back into the formation. The closer V is to $\cos\alpha$, the smaller the movement and the smaller the variation in arrival time. Hence, the apparent velocity will increase with V.

2) $V \geq \cos\alpha$. The reflected wave arrives at the receiver at the same time as the direct arrival, when the tool is completely above the interface and the reflection point is on the borehole wall. When the tool is pulled upward, this point recedes further into the formation; the greater the V, the further it recedes. The apparent velocity will then decrease.

Thus, for a given angle, the apparent velocity will present a maximum for $V = \cos\alpha$ as we can see in Figure 7. It follows that, for a given geometry, two different values of V will yield a single value for v_a/v_{90}. In Figure 8 we show v_a/v_{90} plotted versus α for a given V. These curves are shifted to higher apparent velocity as V increases. This trend is reversed for V ≥ 1. In this case we obtain slowly varying curves, very similar to those obtained when no conversion occurs. The curves are much more sensitive to V when $V < 1$ because of the possibility of having a grazing emergence in this situation. Moreover, these curves will intersect one another due to the occurrence of the maximum described previously.

Unlike the horizontal interface, for a dipping interface the apparent velocities of the reflections for a tool above or below the interface will not be the same. For large z the apparent velocities tend to decrease for a given angle of dip.

[D] Scattering point analogy

The problem of transmitted and reflected events can be viewed as a diffraction problem. In the case of an interface normal to the borehole, the loci of diffracting points are rings around the borehole. A scattering point becomes a secondary source when excited by an incident wave from the transmitter. Conversion phenomena can be taken into account by setting an outgoing velocity different from the incoming one.

When the scattering point sits right next to the borehole wall, the model yields a single hyperbolic arrival time curve (Appendix D) and one obtains at the limit exactly the same results as those discussed in the previous sections dealing with horizontal interfaces. That is, in the way analyzed previously - two reflection events "linked" by a transmission event. Figure 9 displays the travel time curves obtained with a scattering point embedded in the formation at one-tenth of the source-receiver spacing for three velocity ratios. If no conversion occurs, the transmitted event corresponds to the direct arrival. If a conversion occurs, we have two reflection branches with an apparent velocity close to $(v_0^{-1} + v_1^{-1})^{-1}$ and a transmission branch with an apparent velocity close to $(v_0^{-1} - v_1^{-1})^{-1}$. For a scattering point deeper in the formation (Figure 10) the travel time curve is shifted toward later times and becomes smoothed out yielding higher apparent velocities.

The point that we want to emphasize here is the continuity between the two reflections and the transmitted event. A similar analogy can be made for the dipping interface.

Since any type of wave can, theoretically, be converted into any other type, we expect complex features from real data. Surface, pseudo-Rayleigh, and Stoneley waves are, by definition, restricted to the borehole wall. However, at an interface they could scatter into both body (P and S) and guided waves. Such diffraction patterns have been observed where fractures intersect the borehole (Mathieu and Toksöz, 1984 report).

2 Analysis of real data acquired by EVA

In this section we analyze EVA data from the Burch well in Michigan. The tool was run at a slow speed that enabled us to study oblique events over a 1000 foot thick section of the well. We chose two examples for detailed analysis.

(1) The Brown Niagarian formation (see Figure 1) shows a number of oblique events that can be produced by a single discontinuity in a rather homogeneous formation.

(2) The second one consists of the sharp interface between the A-1 carbonate and the A-2 evaporite (see Figure 1).

Conventional logs corresponding to the section studied are presented in Figure 11.

Results of the processing developped by Marc Larrère (1984) at ELF AQUITAINE have been used. The processing has been designed to enhance the oblique events and to separate events with different apparent velocities. A detailed description of it has been reported in appendix E.

2.1 Example 1

The full waveform section of the Brown Niagaran formation is displayed in Figure 2. The source-receiver spacing is 12.75 meters. We shall concentrate on the events at depth 4900 ft, shown in enhanced form in Figure 12.

By comparing sections with various spacings we note that the events originating at about 4900 ft stay at the same location, whereas those at a depth of 4860 ft move with the different values of the spacing. Thus the complex pattern is generated by a single discontinuity located at 4900 ft. The events at depths deeper than 4900 ft and shallower than 4860 ft are reflections and the intermediate ones are transmissions. These transmissions are the first indication of a dipping interface.

These events start at the arrival time of either the P arrival or the S arrival at the 4900 ft depth, and end respectively at the S arrival or P arrival at 4860 ft a spacing length apart. Their measured apparent velocities are about 24.6 kft/s. With v_P = 20.8 kft/s and v_S = 11.3 kft/s, the theoretical apparent velocity is 24.7 kft/s. Several reflections can be seen originating either from the P or S arrival. We designate them by R_P or R_S. We have two R_P and two R_S reflections. They are defined by their apparent velocity in the table. In addition to the slight curvature affecting R_{P1} and R_{S2}, and the fact that some of the velocities are much higher than those we would get from reflections on a horizontal plane, we also infer the presence of a dipping boundary.

To determine the dip angle, we have to compute the v_{90}'s , apparent velocities yielded by a reflection on a horizontal reflector for each possible situation.

Reflection of a P wave without conversion : 10.4 kft/s

Reflection of an S wave without conversion : 5.65 kft/s

Reflection P to S wave and vice versa : 7.3 kft/s

Now, for each of the reflections, we determine the ratio of the apparent velocity to the corresponding v_{90} and then derive the angle α.

TABLE 1

		No Conversion	Conversion
	v_a	$v_a/10.4$	$v_a/7.3$ with V=1.8
R_{P1}:	13.0 kft/s	1.25→59°	1.78→38°
R_{P2}:	9.7 kft/s	0.93→90°	1.33→52°
		$v_a/5.65$	$v_a/7.3$ with V=0.5
R_{S1}:	11.1 kft/s	1.96→40°	1.52→53°
R_{S2}:	7.0 kft/s	1.24→59°	0.97→90°

Discussion

From the values in Table 1, we come up with a set of three possible angles. One set of data gives $\alpha = 90°$ (i.e., a horizontal interface). This case, which does not exclude having a dipping reflector, only means that the reflection occurred very close to the borehole wall.

The remaining angles are close to either 40° or 55° within reasonably small intervals. The question is : which of these two will account for ALL the measured apparent velocities ?

We notice first that angles close to 55° appear four times in the table whereas the other value is approached only twice. Furthermore, R_{P2} and R_{S2} can be explained in two ways, considering reflections either on a horizontal interface or on a 55° dipping reflector. Both events are also stronger than their faster neighbors. Finally, the transmission event matches very well the theoretical apparent velocity for the horizontal interface situation. From our modeling we know that this can only happen when $V=v_0/v_1$ is greater than, or equal to $\cos\alpha$. In our case, V=0.54 yields an angular limit of 57°. In conclusion, we believe that a correct estimation for α is 55°, meaning a dip angle of 35°.

The final results of the interpretation are indicated in the table below. The question mark underlines the ambiguity of having a conversion on a horizontal interface.

TABLE 2

event		wave type before		wave type after reflection	angle
R_{P1}	:	P	→	P	yes
R_{P2}	:	P	→	P	no
	:	S	→	P	yes
R_{S1}	:	P	→	S	yes
R_{S2}	:	S	→	S	yes
	:	P	→	S	no?

2.2 Example 2

Iso-offset sections for Example 2 are displayed in Figures 13 and 14. The offset is 12.75 meters. Figure 13 shows how the processing enhance oblique arrivals. We shall concentrate on all events related to the sharp boundary at depth 4750 ft.

The velocity of the compressional wave for the A-1 carbonate is about 21.7 kft/s, whereas, for the A-2 evaporite, it is 15.0 kft/s. The shear velocities are, respectively, 12.6 and 8.7 kft/s. The caliper log indicates a change in the borehole radius from 8 in to 14 in when passing from the carbonate to the evaporite (see Figure 11). This may account for the very strong events recorded.

Five reflections can be seen on the filtered section in Figure 13: from the P arrival an oblique event with the apparent velocity of 12 kft/s and a second one at about 5 kft/s. From the S arrival, one at 6.6 kft/s, a second at 4.2 kft/s and a third one at about 3 kft/s. A sixth event has been detected in the P arrival wavetrain using the technique of separation (Figure 15, event 3), with the apparent velocity 8.3 kft/s. These events have been sketched in Figure 16.

With the given formation velocities, the theoretical apparent velocities are : 10.85 kft/s for the P to P wave reflection and 6.3 kft/s for the S to S wave reflection. These values yield ratios v_a/v_{90} between 1.1 and 1.05 for the quickest events originating from the P and S direct arrivals. The corresponding events may then be interpreted as reflections on a dipping interface whose α is about 75°, meaning a dip angle close to 15°.

The event detected by applying the separation method corresponds to the S to P conversion, with the theoretical apparent velocity 7.97 kft/s. Again, the ratio v_α / v_{90} is greater than one, showing a non zero dipping value.

The remaining velocities are too low to be explained by reflections involving body waves only. We need to take into account slower surface waves which cause these reflections to occur in the vicinity of the borehole wall. We have reflections of the Stoneley wave converted into a P wave, yielding the apparent velocity of 5 kft/s, and also converted into a S wave, yielding the apparent velocity of 4.2 kft/s. The Stoneley wave is also reflected without conversion, explaining the event at 3 kft/s.

These velocities are a little high compared to the theoretical ones computed from a velocity of the Stoneley wave of 5.6 kft/s: respectively, 4.5, 3.9 and 2.8 kft/s. Nevertheless, they are not high enough to permit considering any body waves. An alternative would be to consider the first mode of the pseudo-Rayleigh wave. It happens in the laboratory. In either case, we should note the strong effect of the borehole radius variation on a surface wave. A non negligible amount of its energy is being reflected back, either directly or converted into body waves.

The properties of the evaporite do not fully appear as long as the receiver has not left the carbonate. This produces sloping events whose apparent velocities can be worked out in a similar fashion as for transmission with conversion. This part forms a "transition zone". We also find transmission with conversion events related to the sharp interface: A P to S wave conversion yielding a measured apparent velocity of 67 kft/s, compared to a theoretical 78.7 kft/s. The S- to P-wave conversion is also visible at about 12 kft/s, versus a theoretical 14.5 kft/s. The record presents also S to Stoneley wave conversions with a measured apparent velocity of 12.5 kft/s to be compared to a theoretical 15.7 kft/s for a velocity of the Stoneley wave of 5.9 kft/s. Here, the agreement is relatively poor. In addition to the fact that the theoretical expression for transmission events is particularly sensitive to small formation velocity variations, multiple interferences in the transition zone made the picking of the events difficult. In particular, events are generated at discontinuities located in the evaporite within a tool length of the sharp interface (see Figure 14). Such events are discussed in Appendix F.

3 Conclusions

After step by step modeling of different cases most likely to occur within a layered medium, we tried to show the consistency between transmission and reflection events in the case of a horizontal interface as well as in the case of a dipping interface. We also presented numerous events that can be associated with a single discontinuity. From our modelling of dipping interfaces, one should remember that they increase the apparent velocity of the events relative to the value obtained with a horizontal interface. One can take advantage of the relative increase to derive dip angles. It illustrates also that one can think of retrieving some lateral information from full waveform acoustic logging data, and could add to the on-going efforts of fracture characterization. Since oblique events are most likely to occur at interfaces with high impedance contrast, fractures could be studied by this method.

The examples presented here show that the real data could be very complex. Data processing, velocity filtering and separation of events enhance the oblique events and improve the accuracy of the results. We observed the general patterns that one can predict from theory. We were able to match the slopes of oblique events and determine the dip of each interface. These dips are consistent with dip-meter data as shown in Figure 17.

References

Biot, M.A., 1952, Propagation of elastic waves in a cylindrical bore containing a fluid: Journal of Applied Physics, 23, 977-1005.

Cheng, CH., and Toksöz, M.N., 1981, Elastic wave propagation in a fluid-filled borehole and synthetic acoustic logs: Geophysics, 46, 1042-1053.

Koerperich, E.A., 1978, Investigation of acoustic boundary waves and interference patterns as techniques for detecting fractures: J. Petro. Tech., 1199-1207.

Larrère, M., 1984, Etude des Evènements pentés observés sur les enregistrements de la sonde acoustique EVA. Rapport de fin d'Etude: I.S.T. Géophysique-Université Paris VI.

Mathieu, F. and Toksöz, M.N., 1984, Determination of fracture permeability using acoustic logs: Paper 47, proceedings, SAID, october 1984.

Panziera, J.P. and Arens, G., 1985, Three components vertical seismic profiles -- polarized waves separations: submitted to the 55th Ann. Meeting of the SEG.

Schoenberg, M., Marzetta, T., Aron, J. and Porter, R., 1981, Space-time dependence of acoustic waves in a borehole: J. Acoust. Soc. Am., 70, 1496-1507.

Seeman, B. and Horowicz, L., 1983, Vertical seismic profiling: separation of upgoing and downgoing acoustic waves in a stratified medium: Geophysics, 48, 555-568.

Serra, O., 1984, Fundamentals of Well-Logging Interpretation, vol. 1, The Acquisition of Logging Data: chap. 15, 247-250, Elsevier.

Tsang, L. and Rader, D., 1979, Numerical evaluation of the transient acoustic waveform due to a point source in a fluid-filled borehole: Geophysics, 44, 1706-1720

Tubman, K.M., Cheng, C.H. and Toksöz, M.N., 1984, Synthetic full waveform acoustic logs in cased boreholes: Geophysics, in press.

White, J.E., and Zechman, R.E., 1968, Computerized response of an acoustic logging tool: Geophysics, 33, 302-310.

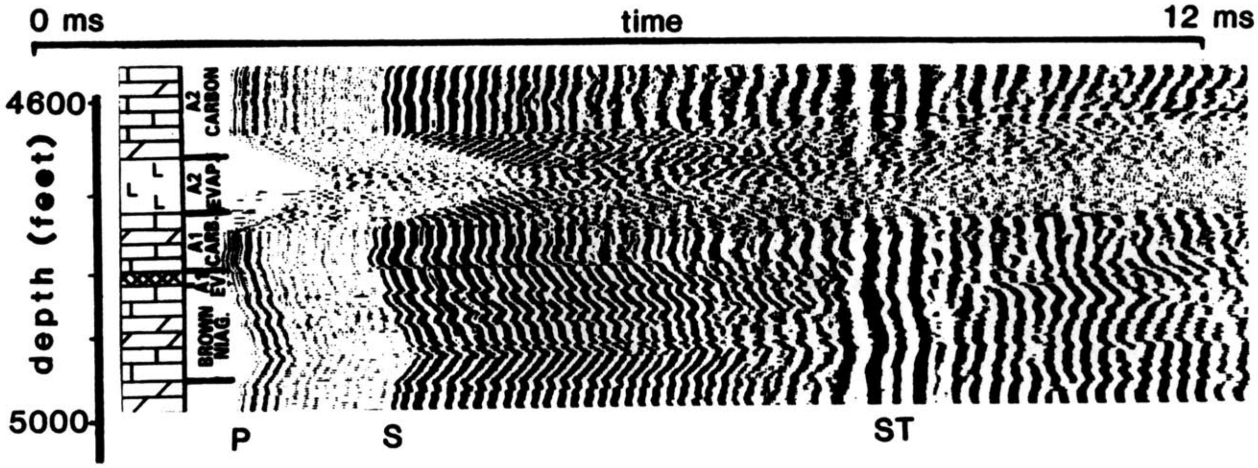

Figure 1. Iso-offset section from EVA tool. The spacing is 12.75 meters.

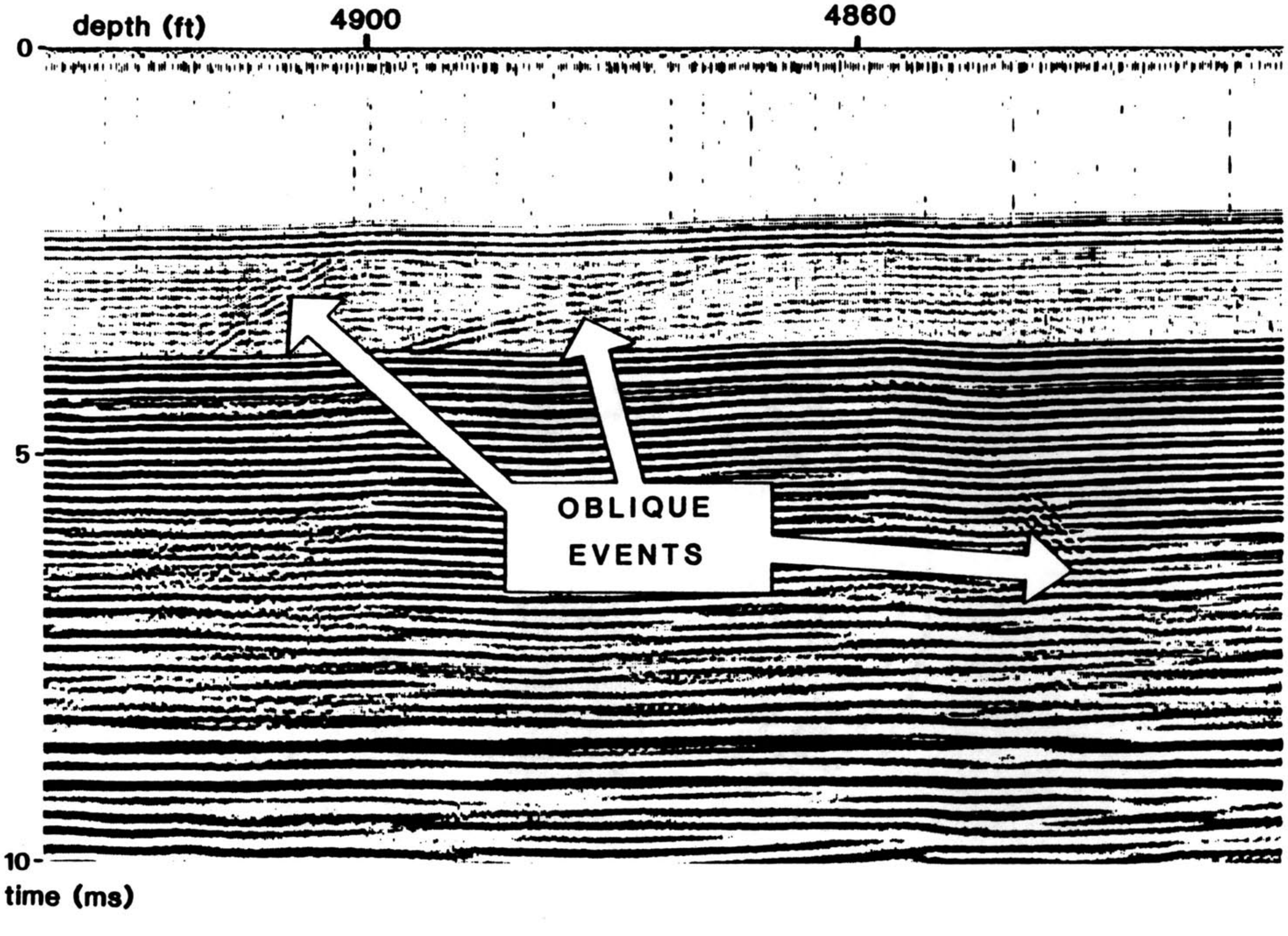

Figure 2. Oblique events on iso-offset section. Source receiver separation is 12.75 meters.

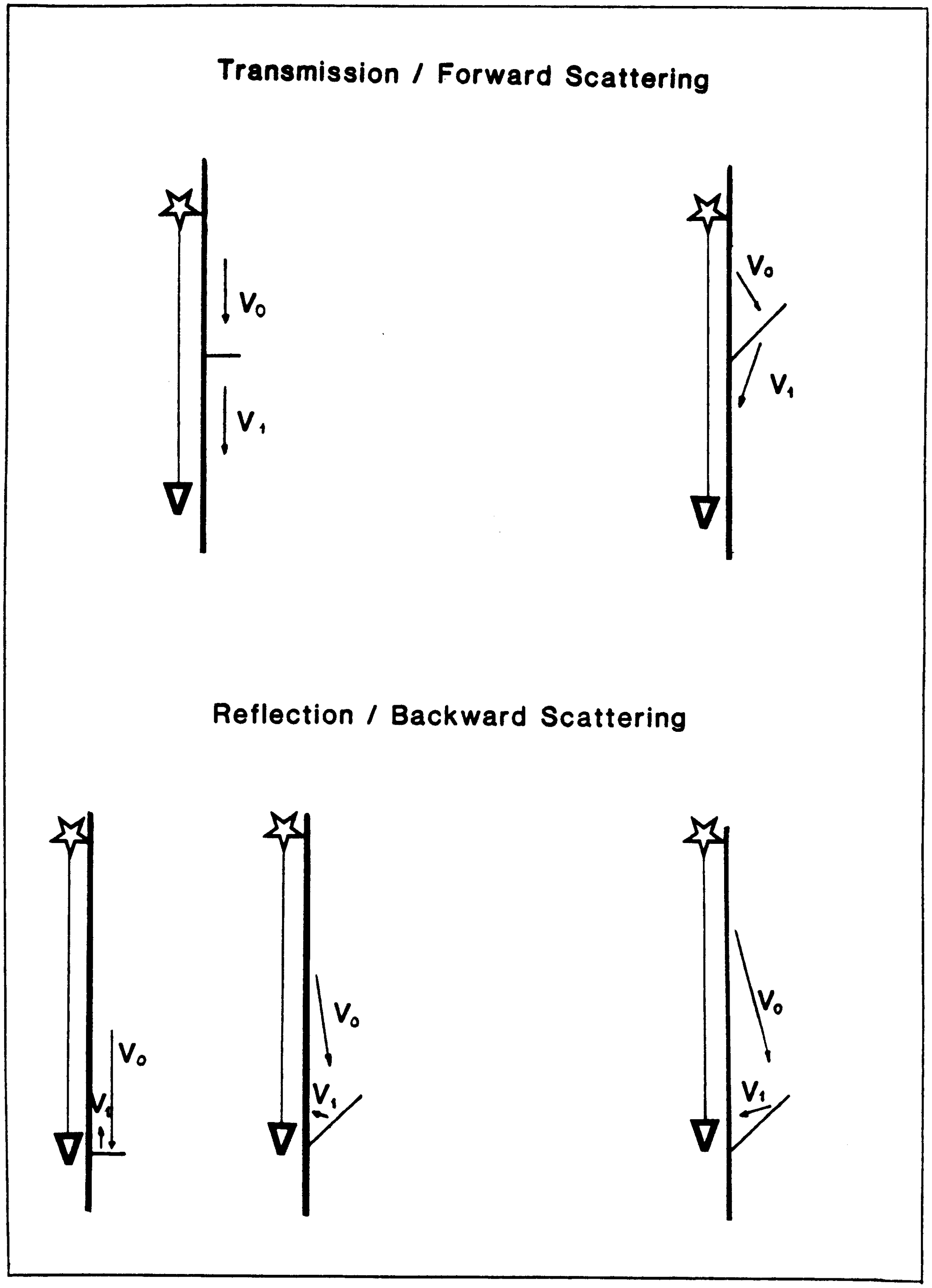

Figure 3. Geometric configurations modelled in this paper. The source is on top of the tool.

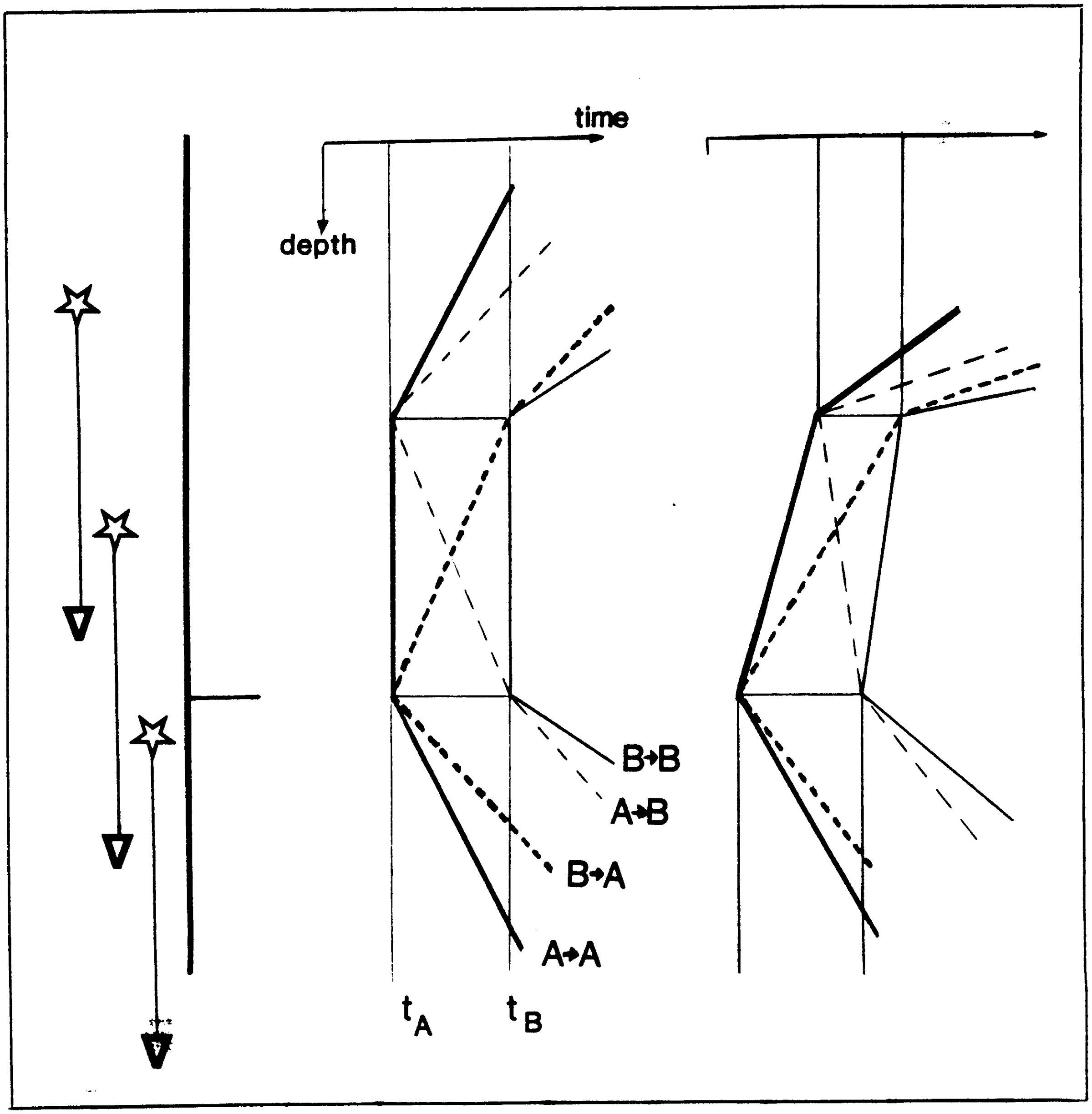

Figure 4. Schematic iso-offset sections displaying the events that can be produced by a single discontinuity involving all possible combinations between only two types of waves noted A and B. The lefthand side of the figure corresponds to an heterogeneity embedded in an homogeneous formation while the righthand side corresponds to the case of a sharp interface.

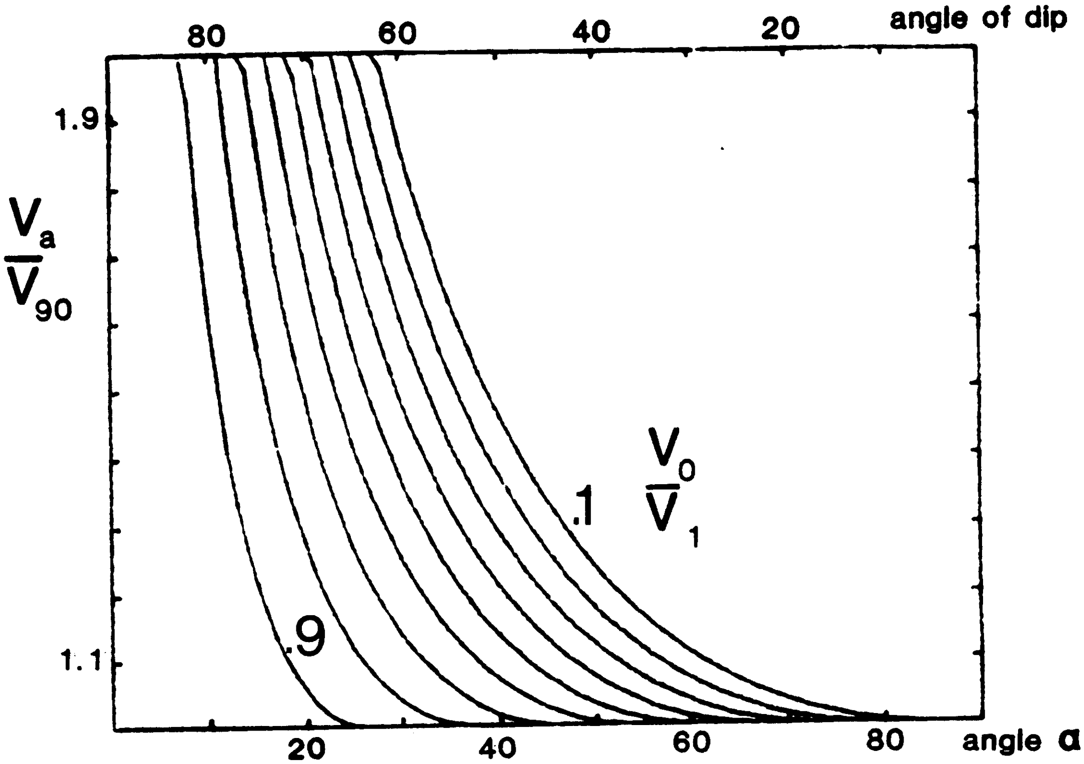

Figure 5. Normalized apparent velocity, v_a / v_{90}, resulting from the transmission with conversion through a dipping plane intersecting the borehole with an angle α to the vertical. Plots have been drawn for velocity ratios (velocity of the incoming wave over the velocity of the outgoing wave, v_0 / v_1) ranging from 0.1 to 0.9.

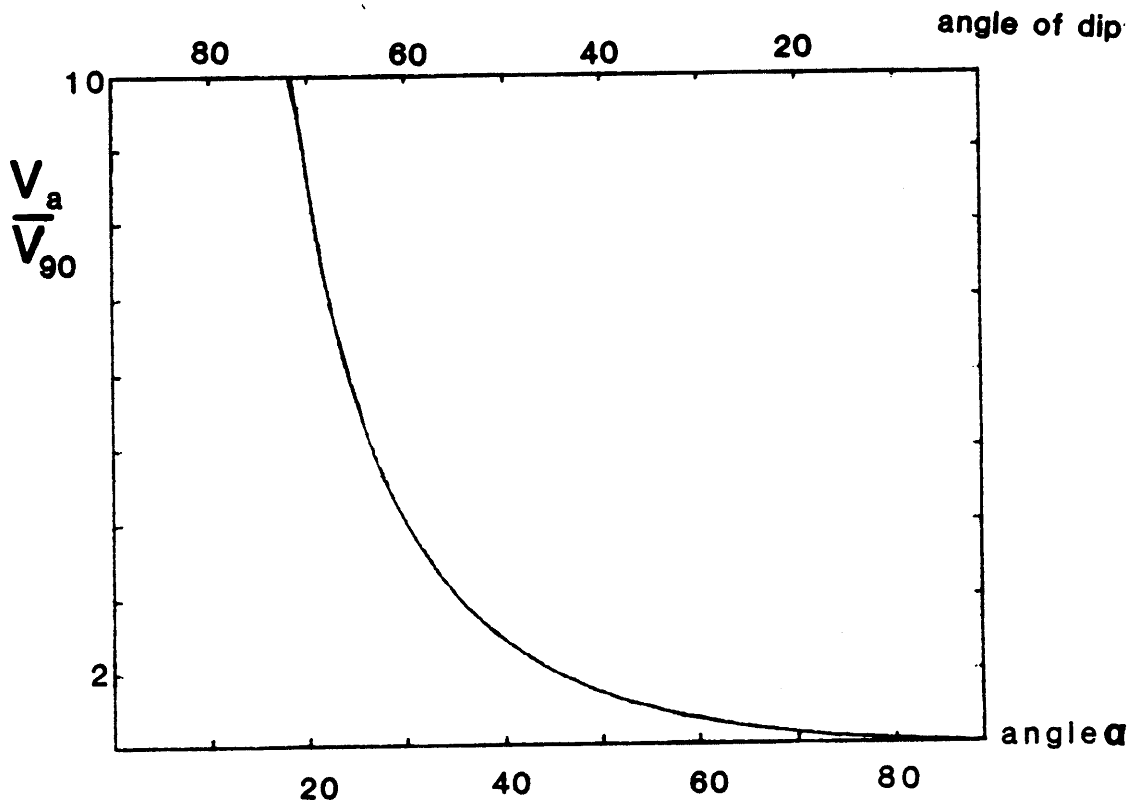

Figure 6. Plot of the apparent velocity v_a, normalized to half the formation velocity versus the angle of dip at z=1 for a reflection without conversion on a dipping plane interface.

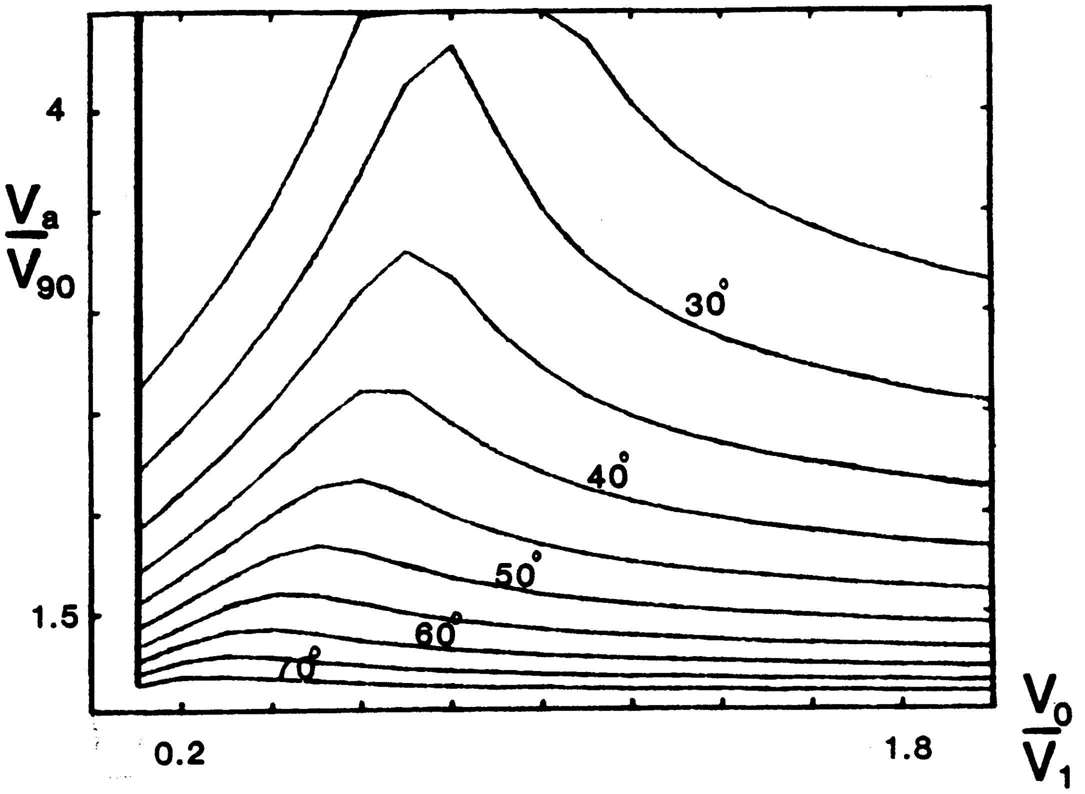

Figure 7. Normalized apparent velocities obtained for a reflection with conversion on a dipping plane interface. Velocities are plotted versus the velocity ratio determining the conversion, v_0/v_1, for given angles α ranging from 25° up to 70°. Each curve has a maximum at $\cos\alpha$.

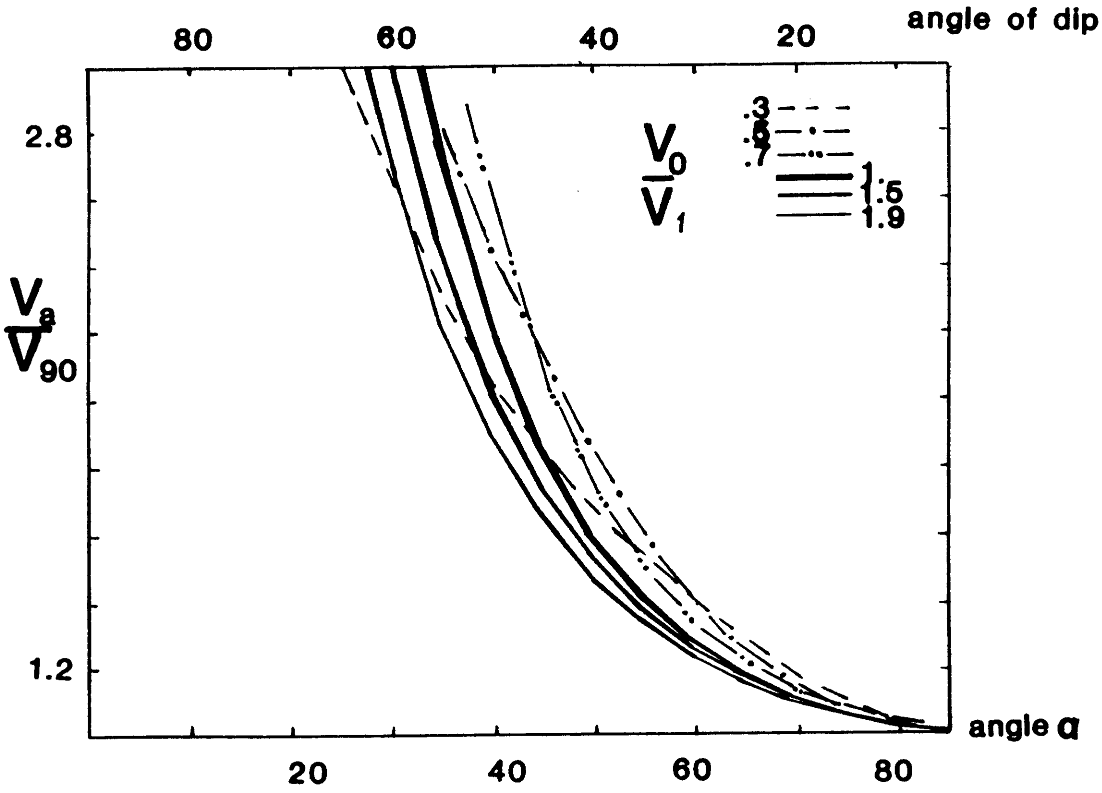

Figure 8. Plot of the apparent velocity obtained for a reflection with conversion on a dipping plane interface. The velocity is normalized with respect to the apparent velocity in the horizontal plane case and plotted versus the angle α for given velocity ratios determining the conversion.

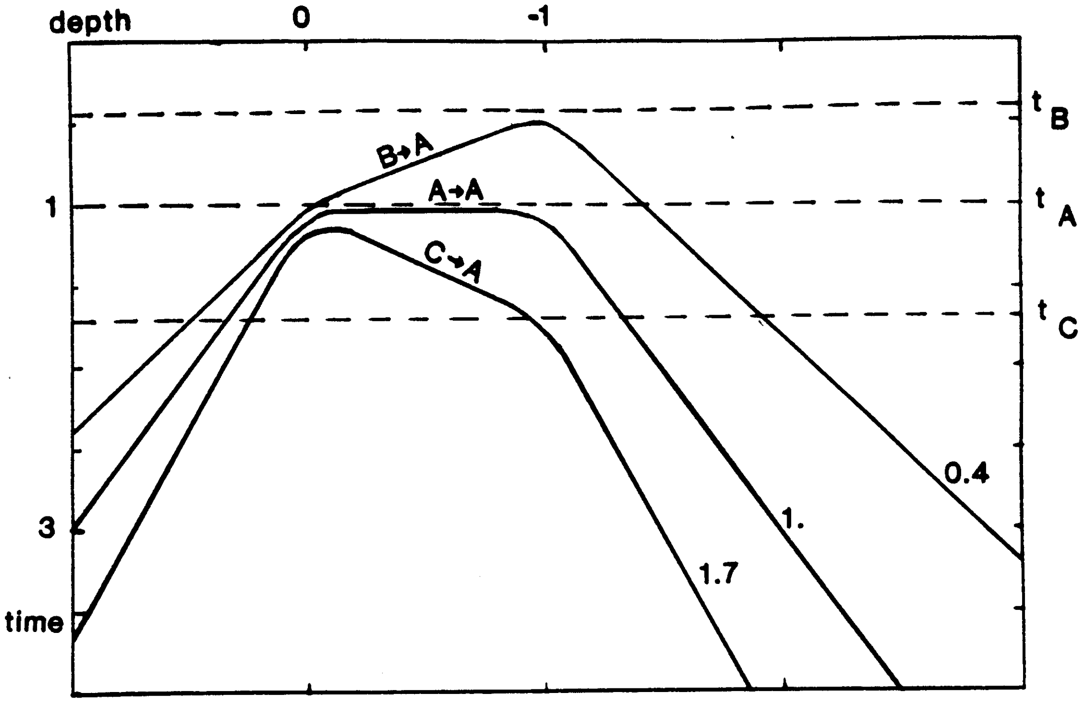

Figure 9. Travel time curves obtained from a scattering point in the formation. Depth units are in spacing length. The point is at depth 0 and .1 deep in the formation. Time units are in t_A, arrival time of the wave of type "A". Two types of conversion have been considered and noted $B \to A$ and $C \to A$, corresponding to velocity ratios, V, of 0.4 and 1.7.

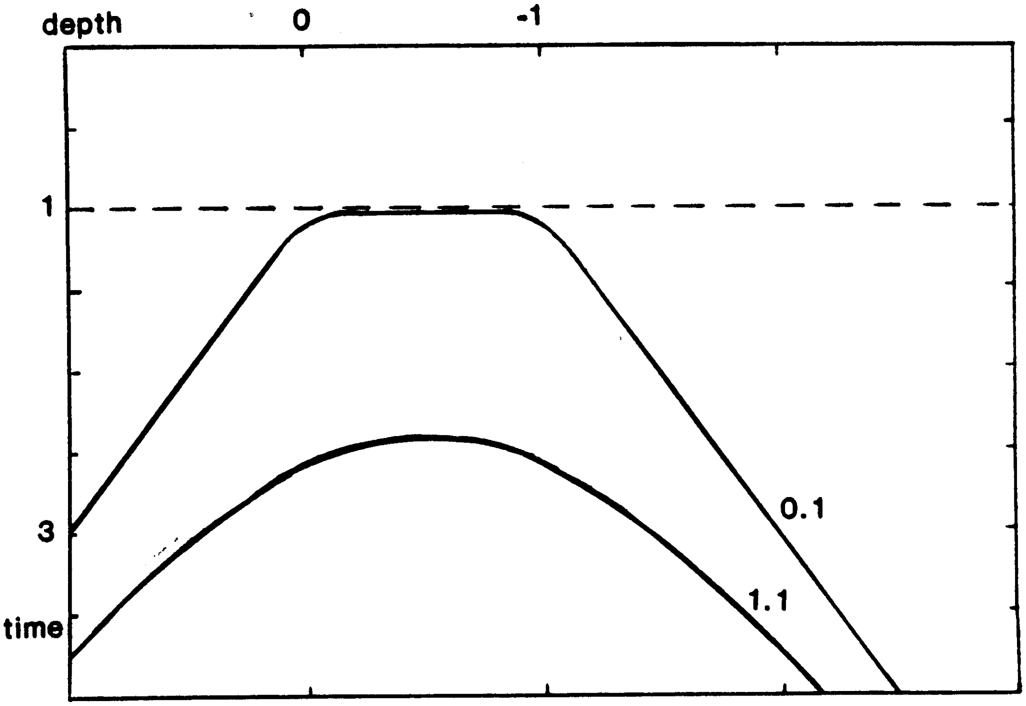

Figure 10. Travel time curves obtained from a scattering point. Conversions have not been considered. The point is 0.1 or 1.1 deep in the formation. The apparent velocities are smoothed out and increased.

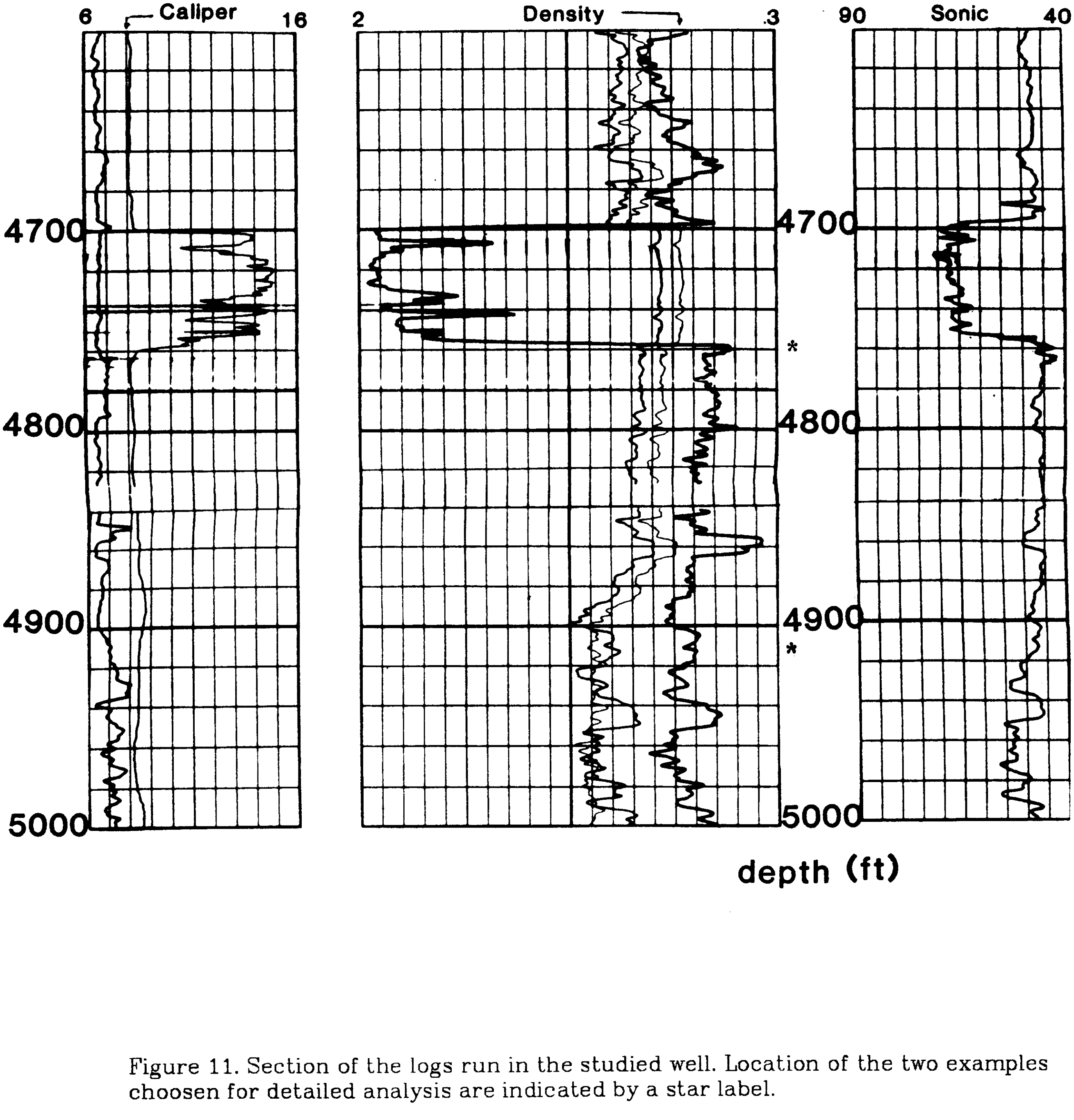

Figure 11. Section of the logs run in the studied well. Location of the two examples choosen for detailed analysis are indicated by a star label.

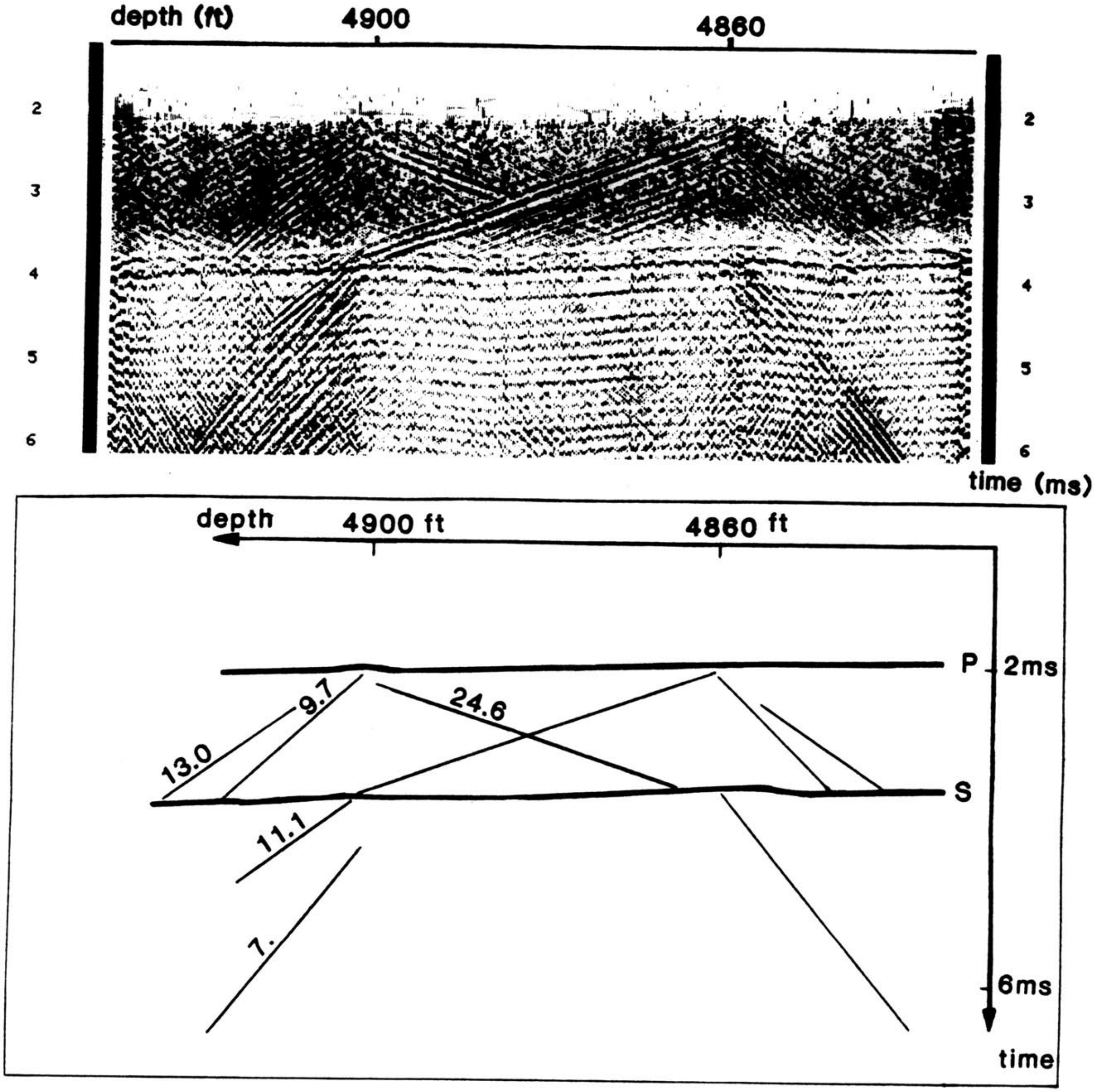

Figure 12. Example 1.Iso-offset section of Figure 2 after fan-filtering and schematic sketch of the events with apparent velocities in kft/s.

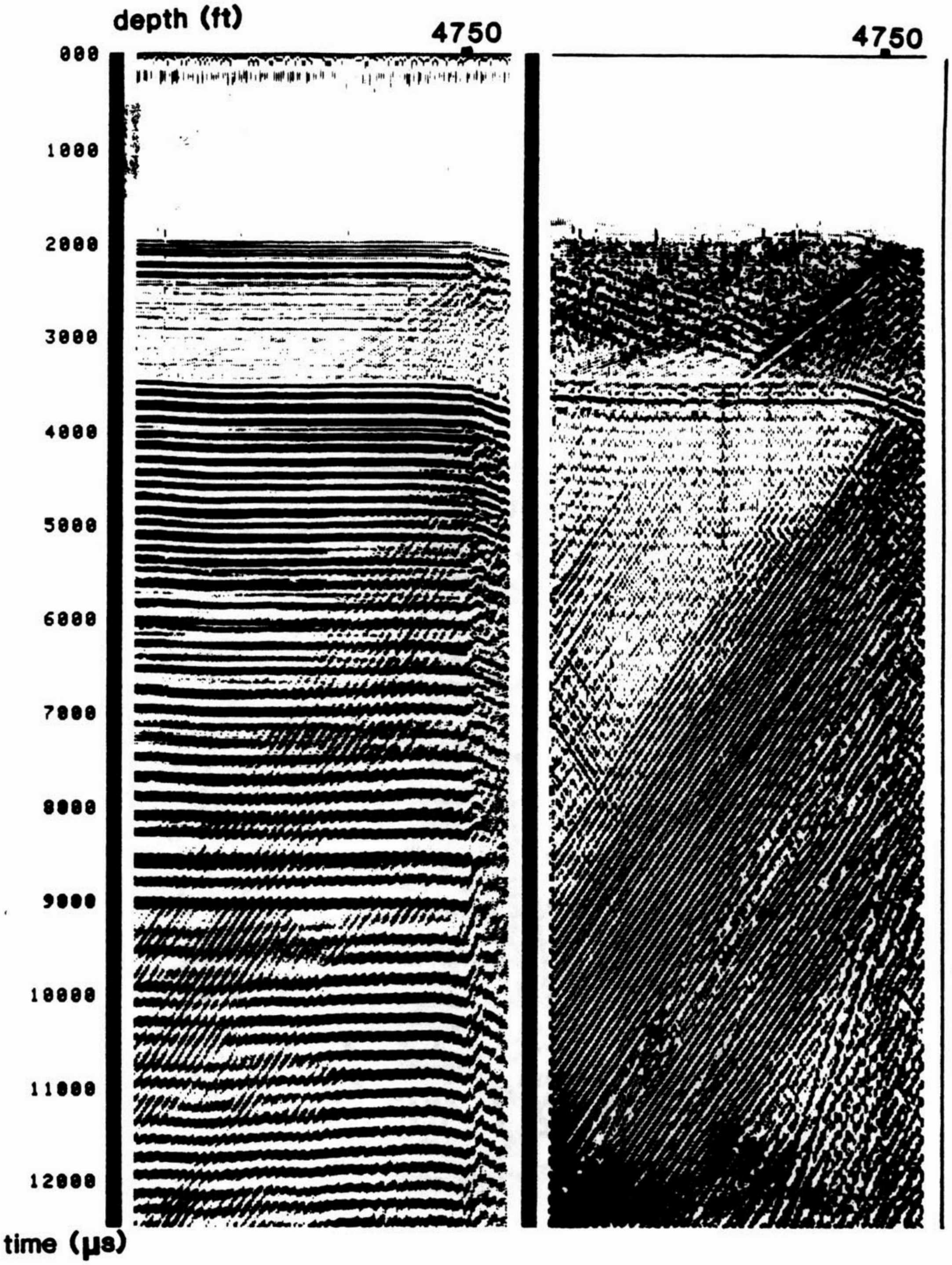

Figure 13. Iso-offset sections before and after fan-filtering corresponding to example 2.

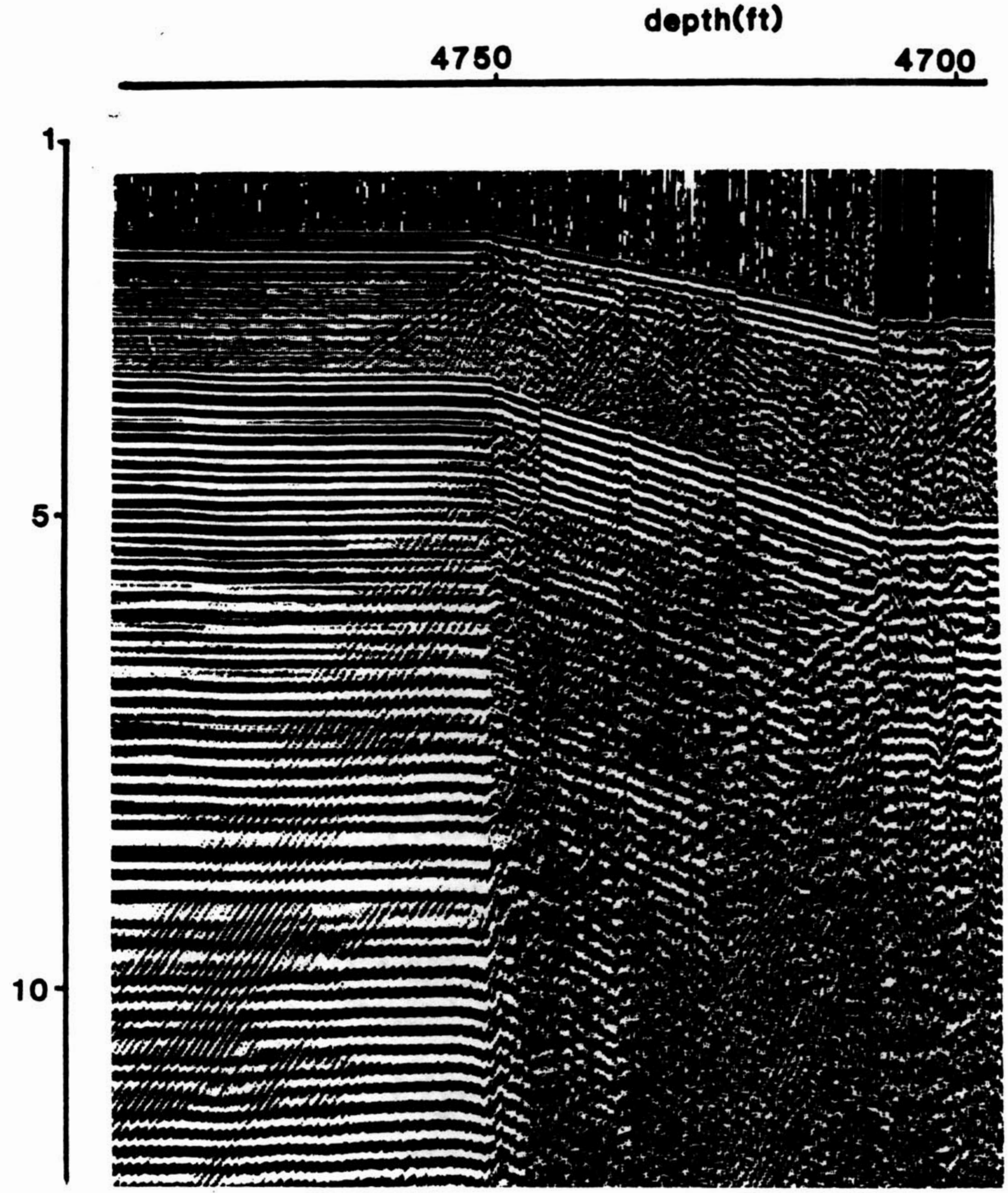

Figure 14. Example 2. Iso-offset section from EVA for a 12.75 meter source receiver separation.

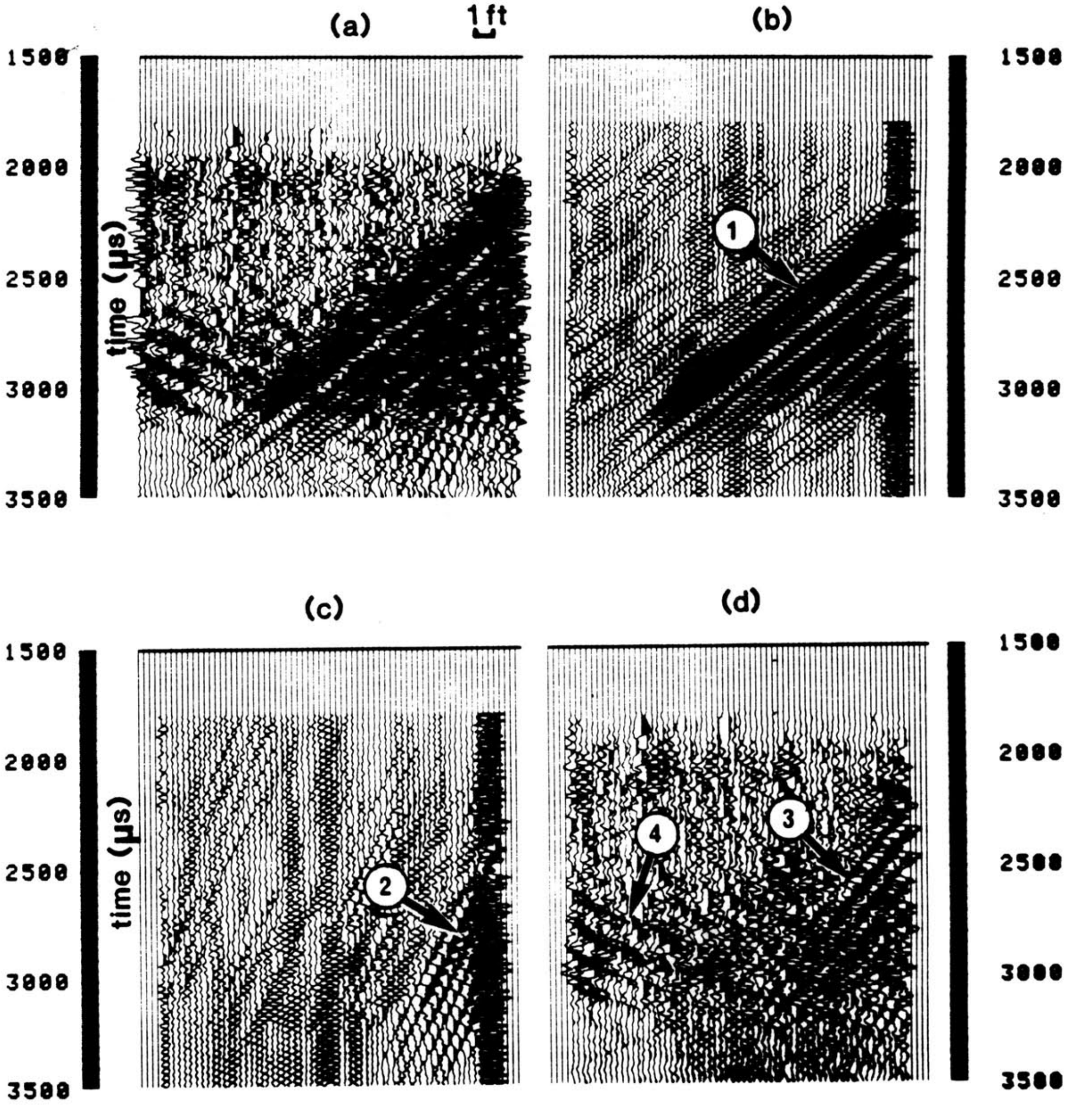

Figure 15. Example of separation. Events 1, in (b), and 2, in (c), are extracted from (a). The residual wavetrain (d) shows two weak arrivals. Notice that event 3 was invisible in (a). (Event 4 is related to a different discontinuity).

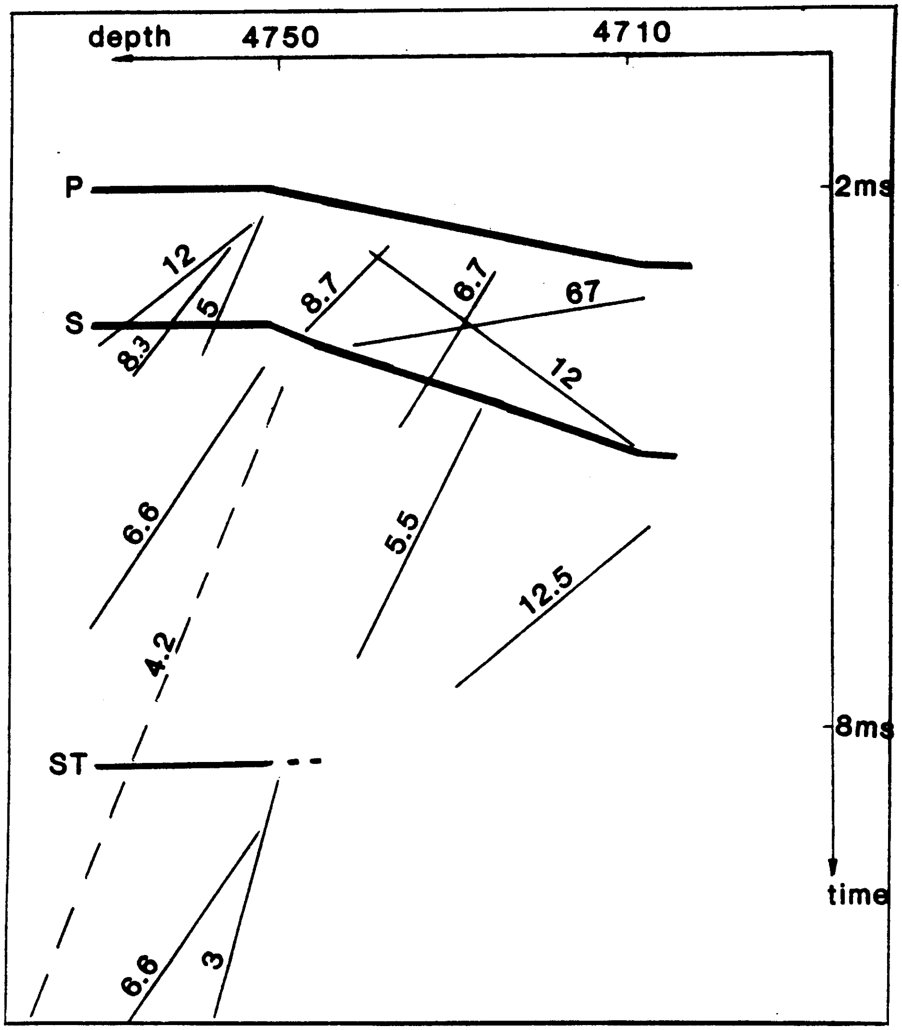

Figure 16. Sketch of the events presented in the text corresponding to the iso-offset section in Figure 14.

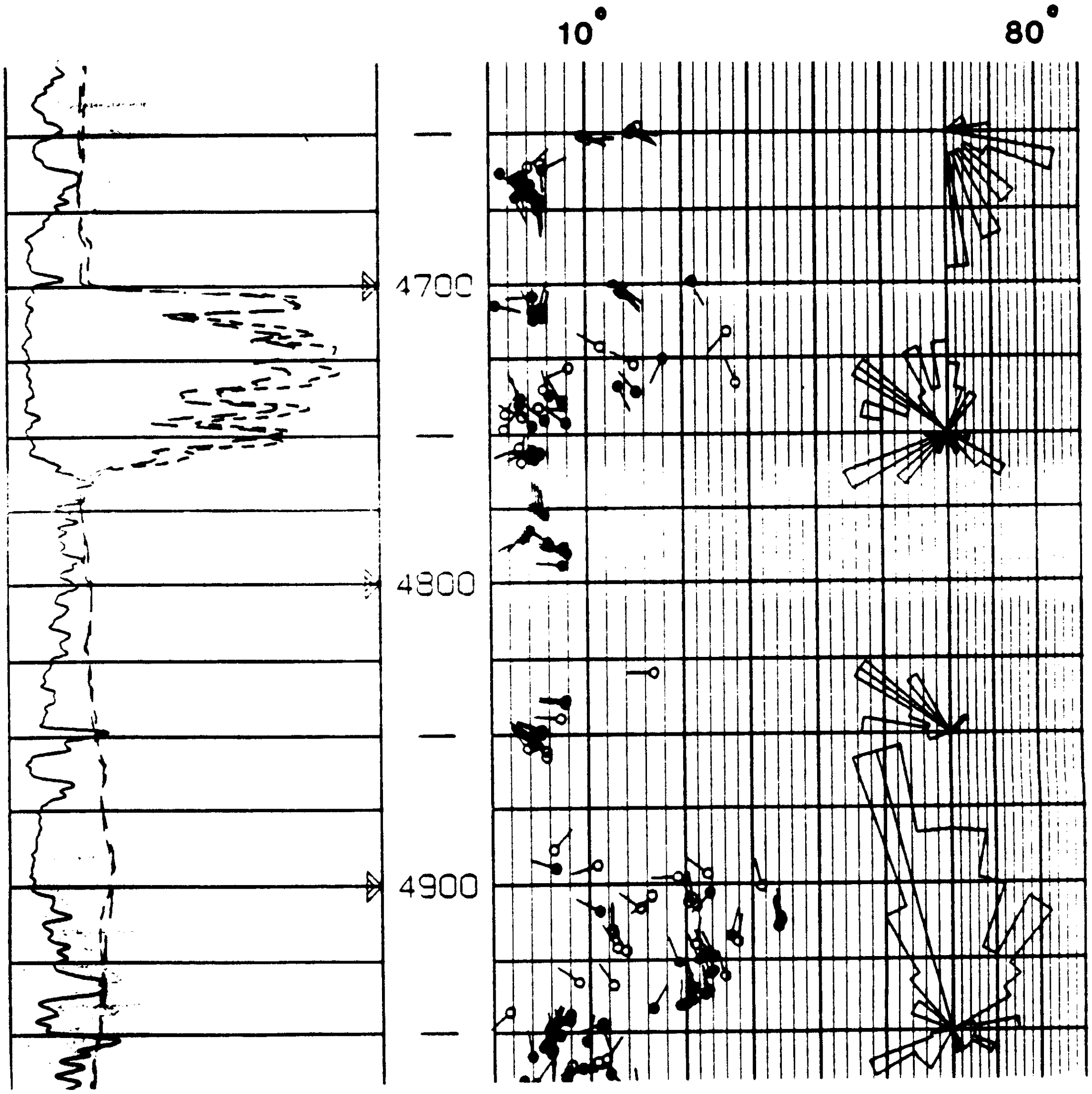

Figure 17. Dipmeter data for the section of the well covering examples 1 at depth 4900 ft and 2 at depth 4750 ft

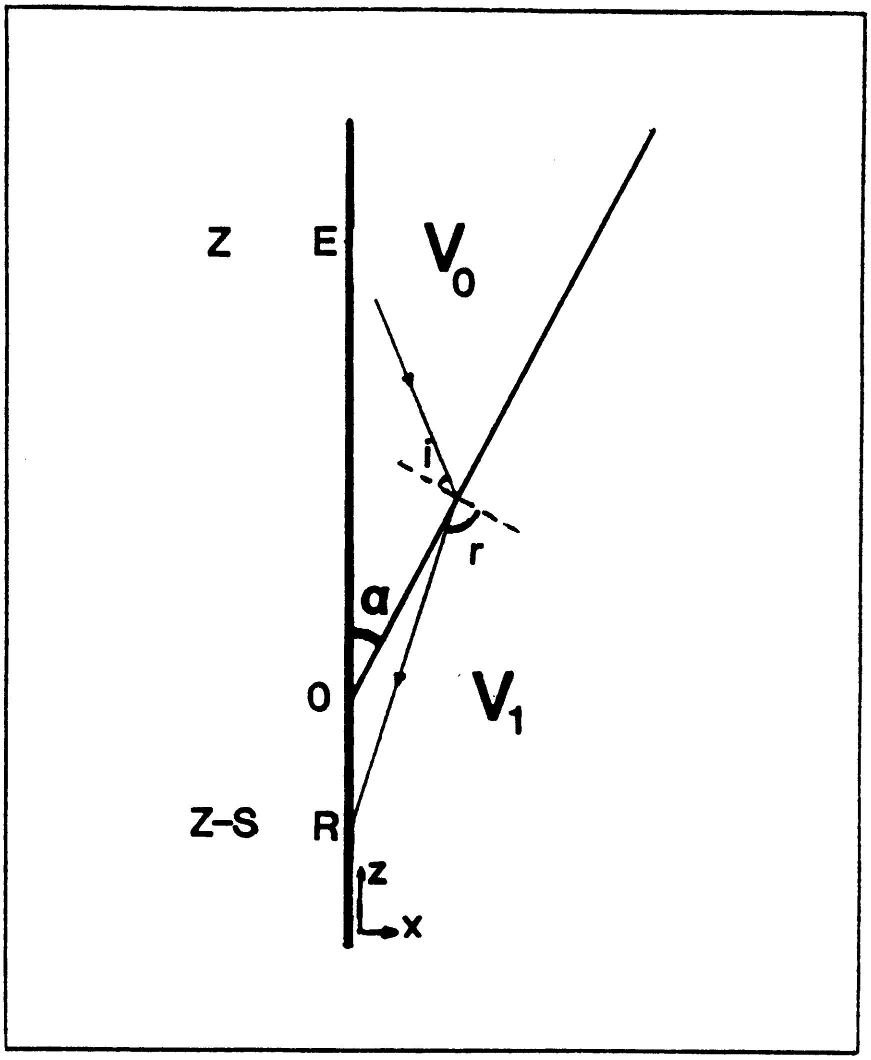

Figure A-1. Geometrical configuration in the case of Appendix A for a transmission with conversion through a dipping plane interface. The source is on top of the tool. In this situation, v_0 is larger than v_1.

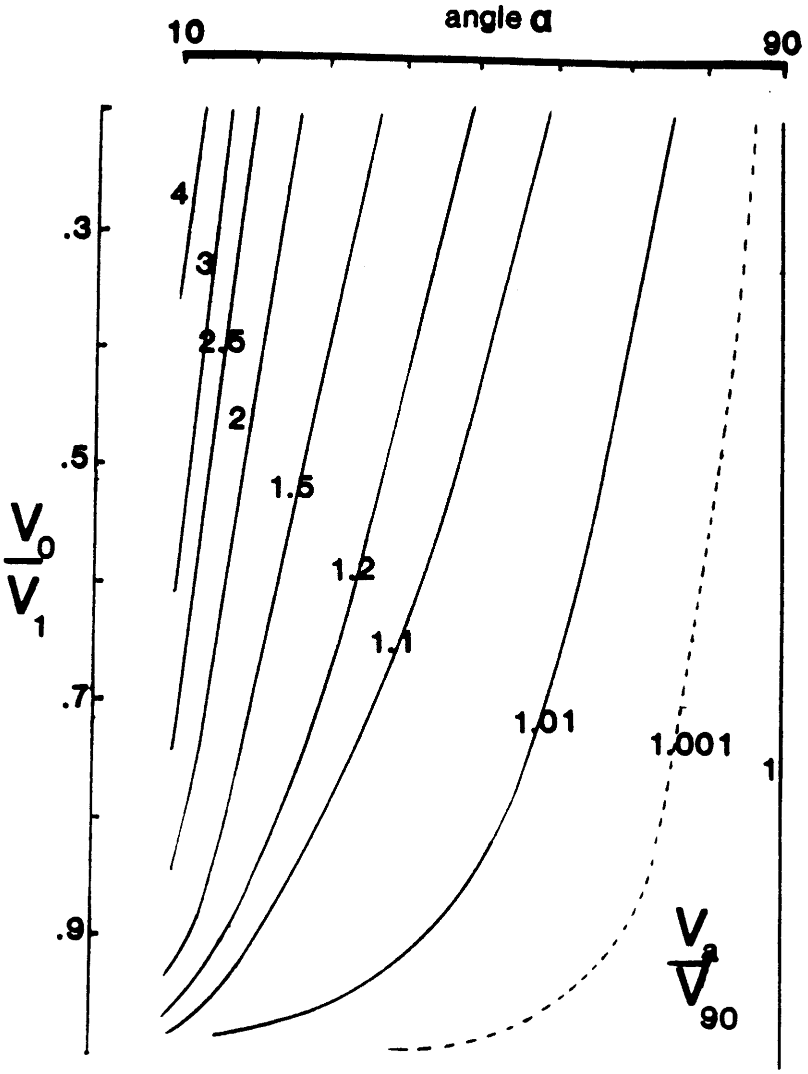

Figure A-2. Transmission with conversion through a dipping plane interface case. Isovalue curves for the average of v_a/v_{90} in the (α, V) plane, that is in the plane angle versus velocity ratio v_0/v_1. The average is taken for z varying from 0.0 to 0.8.

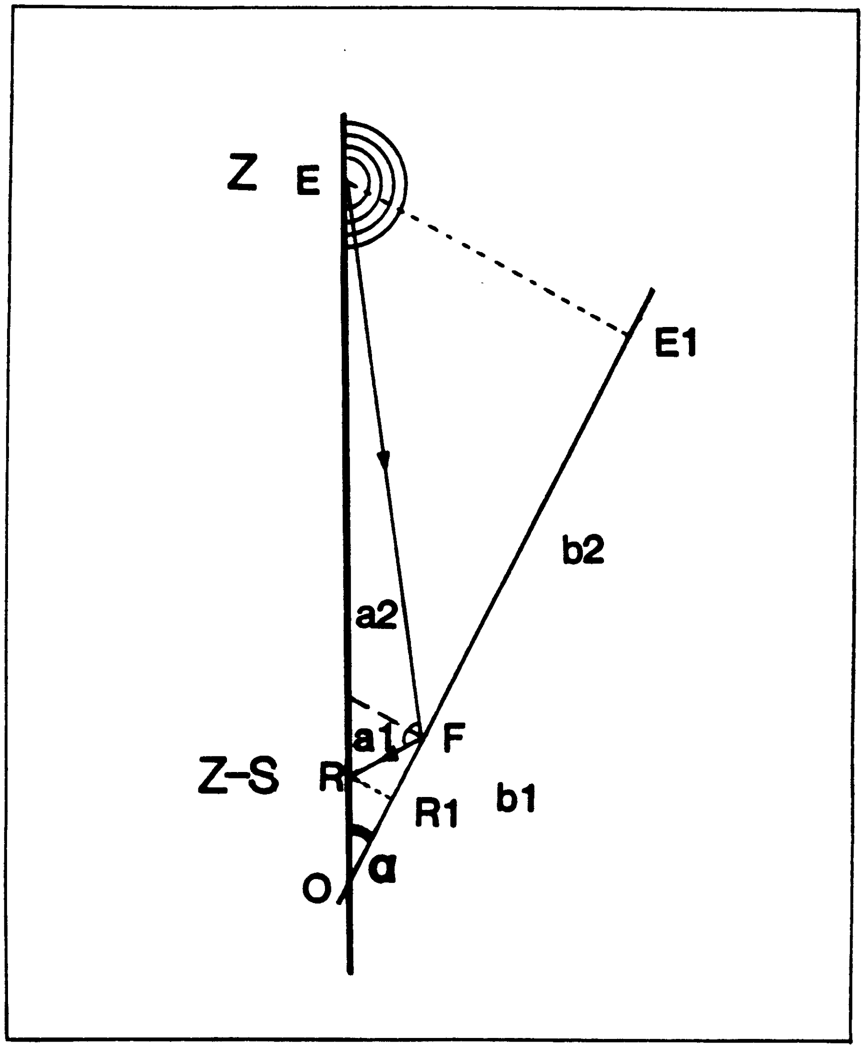

Figure A-3. Geometrical configuration and notations used in Appendix B for the case of reflection on a dipping interface without conversion.

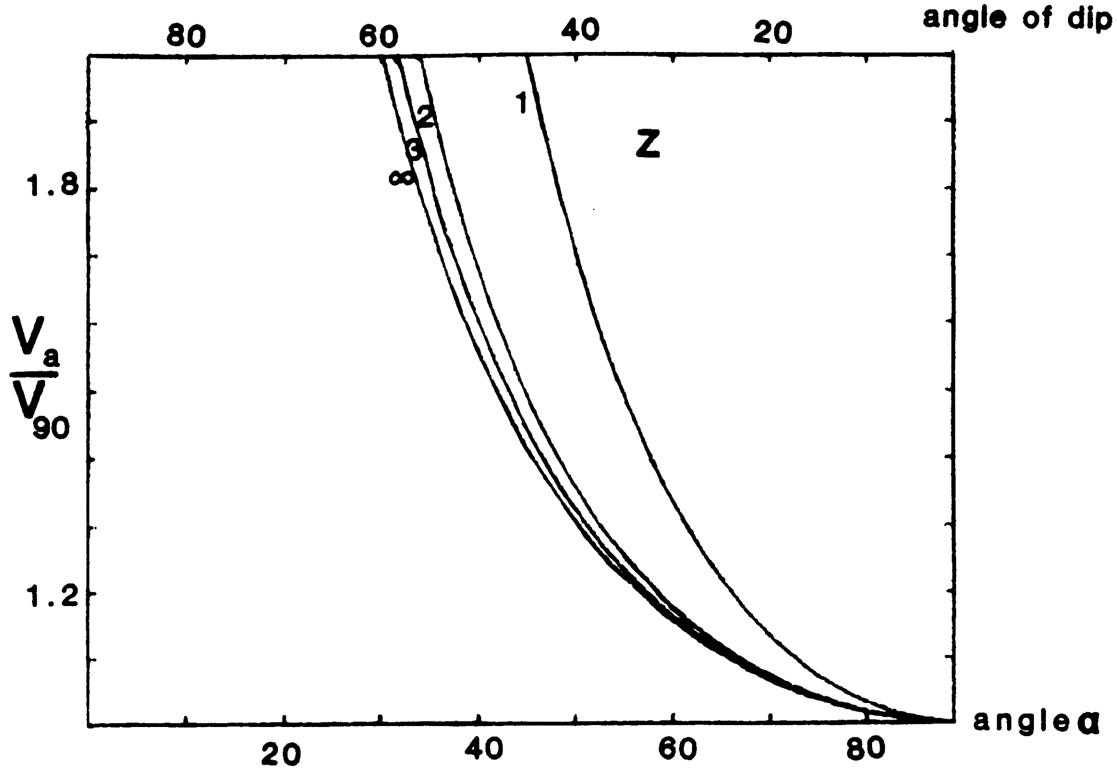

Figure A-4. Plot of the apparent velocity normalized to half the formation velocity against the angle of dip for a reflection on a dipping interface without conversion. Three positions of the tool have been considered, z = 1,2,3 and in the limit, ∞.

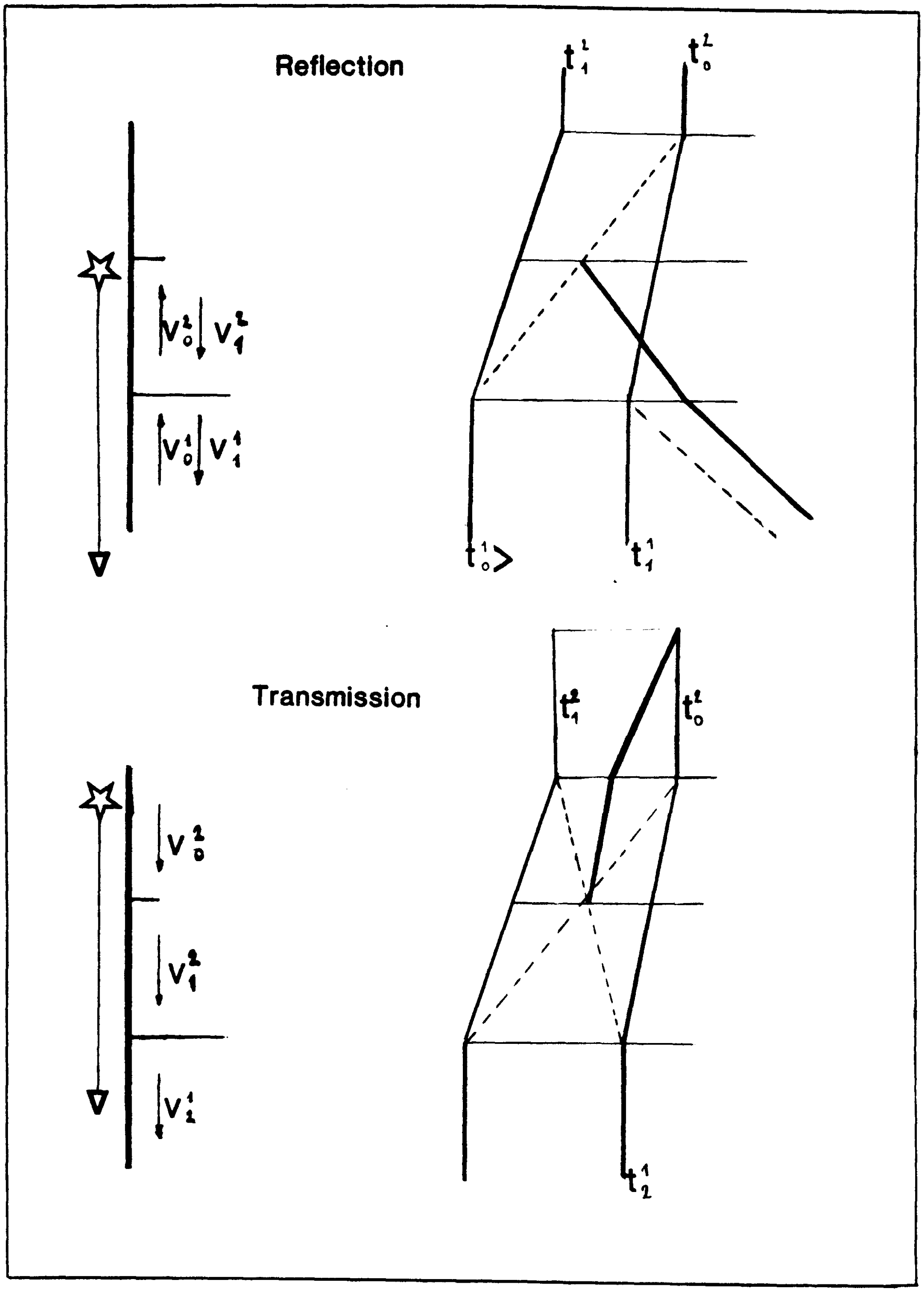

Figure A-5. Schematic iso-offset sections showing events produced in the case of a single discontinuity within a tool length of a sharp interface.Dashed lines indicate events strictly related to the sharp interface.

OBLIQUE EVENTS IN FULL WAVEFORM ISO-OFFSET SECTIONS :

Introduction to appendices A B C and D

In the following appendices we consider the simple case of a plane surface intersecting the borehole axis with an angle α. Note that α is the angle between the interface plane and borehole axis. The dip of the interface is $\vartheta = 90 - \alpha$.

The headwaves are refracted from the fluid into the formation. Regular arrivals observed in full waveform logging correspond to critical refraction, and thus to a downward propagation (in the case where the transmitters are at the top of the tool) along the borehole wall in the formation. Nevertheless, a certain amount of energy propagates away and may impinge on any discontinuity, such as a dipping surface. Using this simple geometry enables us to compute approximate raypaths for body waves travelling away from the borehole and being redirected back to it on the discontinuity.

The general scheme is to compute the arrival time using geometrical relations, and derive the apparent velocity differentiating the travel time curve. Whenever conversion occurs, the exact problem cannot be solved analytically and numerical solutions are necessary.

APPENDIX A : Transmission through a dipping interface

Computation of the arrival time

The tool is astride the discontinuity in the geometrical configuration of Figure A-1. This is also the case where $v_0/v_1 < 1$. Due to the conversion, the apparent velocity of that event cannot be computed in a straightforward manner. We have to define, at first, the point of the interface where transmission occurs. This point is at the intersection of three straight lines in the plane containing the borehole axis and the normal to the reflector. Those lines are :

- The incoming ray
- The outgoing ray
- The trace of the interface in the plane.

We may express the equations of those lines in a system of planar cartesian coordinates with its vertical axis (z) matching the borehole axis and originating at the intersection with the reflector, and an horizontal axis (x) In this system, our three lines are

$$\begin{gathered} z - Z = -tan(i + \alpha)\cdot x \ ; \\ z - (Z - S) = tan(\pi/2 - r - \alpha)\cdot x \ ; \\ z = tan(\pi/2 - \alpha)\cdot x \end{gathered} \qquad \text{(A-1)}$$

Where Z is the location of the source, and S, the source to receiver separation. The incident angle, i, and the reflection angle, r, refer to the normal to the reflector; whereas, α denotes the angular separation between, the vertical and the reflector. The lines having a common point, we have then :

$$(Z/S)(\tan(i+\alpha)-\tan(r+\alpha))=\tan(i+\alpha)+\tan(\frac{\pi}{2}-\alpha) \quad \text{(A-2)}$$

Following some trigonometric manipulations, we get :

$$\tan\alpha\,[\,(Z/S)\tan i+(1-Z/S)\tan r\,]=1 \quad \text{(A-3)}$$

Snell's law provides us with a second equation :

$$\frac{1}{v_0}\sin i=\frac{1}{v_1}\sin r \quad \text{(A-4)}$$

We found it more convenient to use V, the ratio v_0/v_1. In the numerical computations, the angles are worked out by tests using these two equations. Hence i and r are supposedly known in the following calculations. Consequently, the arrival time of the wave can be ruled out :

$$\frac{t}{t_0}=\sin\alpha[\frac{Z/S}{\cos i}+\frac{(1-Z/S)V}{\cos r}] \quad \text{(A-5)}$$

t_0 is the arrival time of the headwave, refracted in the formation under critical incidence and propagated in the formation with the velocity v_0 directly toward the receiver, that is, under the assumptions made here, S/v_0.

Apparent velocity of the arrival.

Equation (A-1) yields an expression (A-6) for the apparent velocity by differentiating both sides with respect to Z or more conveniently, with respect to Z/S. Let $z = Z/S$ vary between 0 and 1.

$$\frac{dt}{dz} = t_0 \sin\alpha \left[\frac{1}{\cos i} - \frac{V}{\cos r} - (z-1)V\frac{\sin r}{\cos^2 r}\frac{dr}{dz} + z\frac{\sin i}{\cos^2 i}\frac{di}{dz} \right] \quad \text{(A-6)}$$

The derivatives of i and r with respect to z can be solved by solving the linear system obtained by differentiating equations (A-3 and A-4). Thus, we have :

$$\cos r\frac{dr}{dz} = \frac{\tan r - \tan i}{\frac{zV}{\cos^3 i} + \frac{(1-z)}{\cos^3 r}} \quad \text{and} \quad \cos i\frac{di}{dz} = V\cos r\frac{dr}{dz} \quad \text{(A-7)}$$

Substituting those two equations in equation (A-6) leads to the final result :

$$\frac{v_{90}}{v_a} = \frac{\sin\alpha}{1-V}[\cos i - V\cos r] \quad \text{(A-8)}$$

Where v_a is the apparent velocity that we have been looking for, and v_{90} the velocity reached for an horizontal interface, namely $v_{90} = (v_0^{-1} - v_1^{-1})^{-1}$.

Discussion

In the different algebraic simplifications made to get equation (A-1), we avoided difficulties arising as the receiver approaches the discontinuity; a situation where r reaches $\pi/2$. This yields numerical instabilities as z tends to 0 and, sometimes, invalidity. Two cases are to be considered:

$v \geq \cos\alpha$

The possible range for incident angles i does not allow r to reach $\pi/2$ and the computation can be done. The converted wave arrives at the same time as the direct arrival : $t = t_0$ at $z = 0$ whereas $t = t_1 = S/v_1$ at $z = 1$. The computation shows that v_a is always near unity. This remains consistent with the fact that for large values of V, the point where transmission occurs stays in the vicinity of the borehole.

$v < \cos\alpha$

Equation (A-1) does not allow r to be equal to $\pi/2$ which happens in this case at $z = 0$. The converted wave arrives earlier than t_0 yielding higher apparent velocities. While the tool moves along the borehole, the transmission point remains somehow at the same place, thus leading to a slowly varying apparent velocity. This enabled us to compute a meaningful average of v_a computed over a limited range of z with the numerical procedure described above.

The results of this computation, restricting z to the interval [0,0.8], are drawn in Figure (A-2) under the form of an iso-value chart for v_a in the plane α, V. Note that the values should be slightly excessive since the apparent velocity decreases continuously, and since we have averaged over the first part of that small variation.

A second way to present results is to consider that v_a is constant. In such a case, one may use the arrival time at $z = 0$, t_2 :

$$\frac{t_2}{t_0} = V\cos\alpha + \sin\alpha\sqrt{1 - V^2} \qquad \text{(A-9)}$$

Hence the apparent velocity :

$$\frac{v_{90}}{v_a} = \frac{V\cos\alpha + \sin\alpha\sqrt{1 - V^2} - V}{1 - V} \qquad \text{(A-10)}$$

These results, presented in Figure 4, are consistent with those of Figure A-2.

APPENDIX B: Reflection on a dipping surface without conversion

The tool is completely below or above the discontinuity. The geometrical problem can be solved directly. Refer to Figure A-3 for all notations in the following section.

Computation of the arrival time.

Because of Snell's law on reflection angles, the geometry presents two isometric triangles. FRR_1 and FEE_1 yield the relation :

$$\frac{b_1}{b_2} = \frac{(Z-S)\sin\alpha}{Z\sin\alpha} \qquad \textit{that is :} \qquad b_1 = (1-\frac{S}{Z})b_2 \qquad \text{(B-1)}$$

We also have:

$$b_1 + b_2 = S\cos\alpha \qquad \text{(B-2)}$$

We may solve those two equations for b_1 and b_2, and substitute into the following equations to get a_1 and a_2:

$$a_1^2 = b_1^2 + (Z-S)^2\sin^2\alpha \qquad \text{and} \qquad a_2^2 = b_2^2 + Z^2\sin^2\alpha \qquad \text{(B-3)}$$

After some easy algebra, we end up with:

$$a_1 + a_2 = \sqrt{S^2\cos^2\alpha + (2Z-S)^2\sin^2\alpha} \qquad \text{(B-4)}$$

This formula yields the trivial result, $2Z - S$ when α is taken to 90° We choose to express the result in terms of the nondimensional ratio of the arrival time of the reflected wave, t, over the arrival time of the direct wave, $t_0 = S/v_0$ and the ratio of the distance, Z, over the spacing S. Let $z = Z/S$. The final result is:

$$\frac{t}{t_0} = \sqrt{1 + 4z(z-1)\sin^2\alpha} \qquad \text{(B-5)}$$

Computation of the apparent velocity of the reflected arrival

Differentiating the two squared terms of the previous equation with respect to t leads to :

$$\frac{1}{2}\frac{t}{t_0^2} = \frac{dz}{dt}(2z - 1)sin^2\alpha \tag{B-6}$$

Let $d(S.z)/dt$ be v_a, the apparent velocity of the reflected wave. We express this equation in terms of non dimensional ratios as v_a/v_{90}, where v_{90} is the velocity for a horizontal interface, namely, $v_0/2$.

$$\frac{v_a}{v_{90}} = \frac{t}{t_0}\frac{1}{(2z - 1)sin^2\alpha} \tag{B-7}$$

Substituting the expression of t/t_0 yields :

$$\frac{v_a}{v_{90}} = \frac{\sqrt{1 + 4z(z - 1)\sin^2\alpha}}{(2z - 1)sin^2\alpha} \tag{B-8}$$

This result is consistent with a velocity of $v_0/2$ obtained for a horizontal plane, that is for $\alpha = 90^o$. For increasing z, the apparent velocity decreases. We note that for large z, v_a/v_{90} behaves as $1/\sin\alpha$ and for z=1, it behaves as $1/\sin^2\alpha$. Figure A-4 presents plots of v_a/v_{90} for $z = 1$, $z = 2$, $z = 3$ and for $z \rightarrow \infty$.

APPENDIX C : Reflection on a dipping surface with conversion

With the same geometrical configuration as in Appendix B, we shall work out the apparent velocity of a headwave traveling in the formation at velocity v_0 impinging on our plane surface and being reflected with velocity

v_1. The apparent velocity of the wave cannot be computed in the same straightforward manner as in Appendix B.

The geometrical problem is very similar to that of Appendix A, except for some sign changes. Following those developments, we first define the reflection point as the intersection of three straight lines analytically defined in a cartesian system of coordinates.

Arrival time

The system is solved, yielding the equation :

$$\tan\alpha\,[\,(Z/S)\tan i + (Z/S - 1)\tan r\,] = 1 \qquad \text{(C-1)}$$

Snell's law provides us with a second equation, which, together with equation (C-1), defines uniquely the angles, and thus the point of reflection.

$$\sin i = V\sin r \qquad \text{(C-2)}$$

where $V = v_0/v_1$. In the numerical computations, the angles are worked out by trying successive values until they satisfy both equations (C-1) and (C-2).

Once i and r are known, the arrival time of the reflected event can be ruled out. Let $z = Z/S$:

$$\frac{t}{t_0} = \sin\alpha\left[\frac{z}{\cos i} - \frac{(1-z)V}{\cos r}\right] \qquad \textbf{(C-3)}$$

t_0 is the arrival time of the headwave, refracted in the formation under critical incidence and propagated in the formation with the velocity v_0 directly toward the receiver, that is, under the assumptions made here, $t_0 = S/v_0$.

Apparent velocity of the reflection arrival

By differentiating both sides of equation (C-3) with respect to z, we obtain an expression for the apparent velocity:

$$\frac{dt}{dz} = t_0\sin\alpha\left[\frac{1}{\cos i} + \frac{V}{\cos r} + z\frac{\sin i}{\cos^2 i}\frac{di}{dz} - (1-z)V\frac{\sin r}{\cos^2 r}\frac{dr}{dz}\right] \qquad \text{(C-4)}$$

The derivatives of i and r with respect to z can be obtained by solving the linear system obtained from differentiating equations (C-1) and (C-2). Thus, we have:

$$\cos r\frac{dr}{dz} = -\frac{\tan r + \tan i}{\frac{(z-1)}{\cos^3 r} + \frac{zV}{\cos^3 i}} \quad \text{and} \quad \cos i\frac{di}{dz} = V\cos r\frac{dr}{dz} \qquad \text{(C-5)}$$

Substituting those two equations in equation (C-4) leads to the final result :

$$\frac{v_{90}}{v_a} = \sin\frac{\alpha}{1+V}[\cos i + V\cos r] \qquad \text{(C-6)}$$

where v_a is the apparent velocity that we have been looking for, and v_{90} the velocity reached for a horizontal reflector, namely, $(v_0^{-1} + v_1^{-1})^{-1}$.

Again, as described in Appendix A, problems are to be expected because of the simplifications made to reach the last result. Two cases are discussed in the text. We escaped the numerical difficulties by computing the apparent velocity at some distance from the interface through an accurate determination of the angles (equations C-1 and C-2). Namely, we took $z = 1.1$ to generate Figures 8 and 9.

APPENDIX D : Scattering point in the formation

In this model we consider a point in the formation at the distance E from the borehole axis. Body waves coming from the transmitter at a velocity v_0 encounter this point and are re-emitted instantaneously with a velocity v_1 toward the receiver. The point acts as a "perfect" scatterer. The algebra is very straightforward.

Arrival time

Let Z be the location of the source; $Z - S$ that of the receiver. The distance from the source to the scattering point is $Z^2 + E^2$, while $(Z-S)^2 + E^2$ is that from the point to the receiver. Normalizing all the distances with respect to the spacing S, and the time with respect to the arrival time of the direct wave at the velocity v_0, we can write:

$$\frac{t}{t_0} = \sqrt{z^2 + e^2} + V\sqrt{(z-1)^2 + e^2} \qquad \textbf{(D-1)}$$

where $z = Z/S$; $e = E/S$.

Apparent velocity

As done previously, we differentiate the travel time curve to get the apparent velocity, v_a.

$$\frac{v_0}{v_a} = z\left[\frac{1}{\sqrt{z^2 + e^2}} + \frac{V}{\sqrt{(z-1)^2 + e^2}}\right] \qquad \text{(D-2)}$$

We can check that as $z \to \pm\infty$, $v_a^{-1} \to \pm v_0^{-1} + v_1^{-1}$

APPENDIX E : Data processing n

(by Marc Larrère)

Since oblique events are the result of reflection, conversion, and transmission travel paths, they are generally weaker in amplitude than "regular" arrivals. In order to achieve an accurate detection and a good determination of the slope of these events we need to separate them from the main wavefield. In formations where velocities vary slowly with depth, the main wavefield is roughly horizontal (infinite apparent velocity) whereas reflection and transmission events show finite apparent velocity. The F-K filtering technique allows us to extract the oblique events that interest us. We can go further and extract two given types of waves using the method of separation described by Seeman and Horowicz (1983).

Velocity filtering

Velocity filtering is a widely used technique in seismic processing that can be readily applied to iso-offset sections. However the following conditions have to be satisfied.

1) Constant logging speed is required in order to achieve constant spatial sampling.

2) Cut-off velocities must be chosen in order to preserve the highest finite apparent velocities. The optimization may be different for different formations and at different arrival times on the section.

3) Spatial aliasing must be avoided to guarantee accurate results from filtering algorithms. This leads to the constraint that the spatial sampling must be less than $\Delta Z(Nyquist) = V_a / 2Fmax$ for all types of waves. This condition requires generally a very dense spatial sampling.

Let us consider, for example, reflections from a horizontal interface involving P and Stoneley waves in a hard formation. The upper frequency of the P wave is close to 25 kHz whereas the Stoneley frequency is less than 6 kHz. The P and Stoneley wave velocities are 20 kft/s and 5.6 kft/s which yield reflected events with apparent velocities 10 kft/s and 2.8 kft/s. In both cases the theoretical minimum sampling rate is close to 2.5 inches.

However, a practical upper bound of 4 inches still provides good numerical results.

Figure 12 shows results obtained when appling a symmetrical fan filter to the EVA section of Figure 2. Despite the high cut-off velocity required to preserve the transmission events, the filtering has strongly enhanced oblique events. A second example is presented in Figure 13. Again, velocity filtering allows us to pick oblique arrivals more precisely.

Separation of waves

Unambiguous interpretation of interfering events sometimes requires further processing to separate the events with different velocities. A good approach is the method used in VSP to separate the up- and downgoing waves. The method is based on the assumption that each recorded signal is the superposition of two coherent waves with different apparent velocities and a random component. The solution is obtained by a least square minimization of the residual wavefield in the frequency domain. This technique requires the picking of travel times of the two events we want to separate.

Figure 15 shows results of this separation applied on previously dip-filtered data. As expected, the two main signals we were able to pick are well separated. Furthermore, the residual error shows two weak events we were unable to detect even on filtered data.

Separation techniques are very useful to study a given type of wave and to detect possible weak events. The method can be extended to any number of waves (Panziera and Arens, 1985), and therefore would be more appropriate in our case.

APPENDIX F: Multiple interfaces effects

In this appendix we consider the data of example 2 (as in Figure 14). Events originate from the "transition zone". Here, the presence of several discontinuities, next to the sharp interface and within a tool length, is expressed by intermingled oblique events. Each one of these originates from a discontinuity that can be found on the conventional logs. These are mainly variations in borehole diameter and in density (see Figure 11).

The proximity of the nearby sharp interface implies that the apparent velocity of any event visible in the transition zone will be a function of the two different media. In our reasoning, the tool is not yet completely above the sharp interface. Furthermore, reflections occuring on such discontinuities, but recorded in the first medium will, naturally, involve properties of this medium.

Let us consider only plane interfaces as in figure A-5. A sharp interface separates two media, the "first" and the "second" media. A wave emitted in the first medium with the velocity v_0^1 propagates upward toward the interface. At this point, it is transformed into a wave with a velocity v_0^2. Propagating in the second medium, it is reflected back with conversion on a secondary discontinuity with the velocity v_1^2, and is finally transformed through the first boundary into a wave with the velocity v_1^1. This complex event will have the apparent velocities :

$((v_1^1)^{-1} + (v_0^2)^{-1})^{-1}$ in the zone between the two interfaces.

$((v_1^1)^{-1} + (v_0^1)^{-1})^{-1}$ before the sharp interface.

In other words, reflections on a farther discontinuity observed through a nearer one, may appear on the records with exactly the same velocity as direct reflections on the nearer interface, with only a time lag. This phenomenon may account for the strength and extent of the reflections with an apparent velocity of 6.6 kft/s.

We now consider apparent velocities within the "transition zone". Some of them are 8.7, 6.7 and 5.5 kft/s. Those are to be compared, respectively, to :

$$8.9 = (15.0^{-1} + 21.7^{-1})^{-1}$$

$$6.8 = (15.0^{-1} + 12.6^{-1})^{-1}$$

$$5.1 = (8.7^{-1} + 12.6^{-1})^{-1}$$

The first velocities used in these formula belong to the A-2 evaporite, while the second ones correspond to the A-1 carbonate. Considering the time at which those events take place, one can work out the type of conversion occuring on the second discontinuity. They can start at the P- to P-wave transmission arrival time curve, the S- to S- wave, or the S- to P-, or the P- to S- curve, due to the sharp interface.

Transmission patterns due to a second discontinuity may be also affected by the sharp interface (see figure A-5 for notations). Let us consider a wave travelling in the second medium at the velocity v_0^2, then converted, after transmission through the second discontinuity, into a wave with the velocity v_1^2, and, again, changed at the sharp interface into a wave travelling in the first medium at the velocity v_2^1. The resulting oblique event will have the apparent velocities :

$((v_0^2)^{-1} - (v_2^1)^{-1})^{-1}$ in the transition zone.

$((v_0^2)^{-1} - (v_1^2)^{-1})^{-1}$ before the transition zone.

CHAPTER 3 :

INVERSION OF TRAVEL TIME FOR VELOCITY USING MULTI-SPACING SONIC TOOLS

Introduction

In full waveform acoustic logging, the general trend has been to increase the source to receiver separation as well as the receiver spacing, in order to obtain a deeper penetration of the unperturbed formation and to measure velocity more accurately. The increases of the spacing between receivers and the length of the receiver array have the undesirable effect of smoothing out the variation of velocities over short depth increments. This could cause reduction in spatial resolution, especially in cases where thinly layered stratigraphic units are present. In this study we introduce a method to help resolve the velocities and thicknesses of the thin beds.

Willis (1983) introduced a least squares inversion scheme to determine the transit times and velocities for individual beds. This inversion method is relatively slow and can become cumbersome when applied to large sections. We propose a stochastic formulation that enables us to recursively solve for the transit times. This procedure amounts to removing the effect of the tool length, which acts as a running sum filter. It can also be viewed as a deconvolution process of the tool response. In the following sections we describe the method and its applications to synthetic as well as real data.

1. Forward problem

The travel time of acoustic waves is a function of the borehole radius, the velocity of compressional waves in the fluid and the formation body waves, as well as the length of the tool.

As a first approximation, let us neglect the borehole effects, and calculate the travel time for a wave propagating vertically in the formation between the source and the receiver :

$$T(Z) = \frac{1}{S} \int_{Z-S}^{Z} t(z) dz \qquad (1)$$

where S is the source receiver separation, $t(z)$ the formation slowness, and $T(Z)$ is the travel time per unit length at depth Z, assuming that source and receiver are located at depths Z and $Z - S$, respectively.

As seen in Figure 1, a sharp interface between two formations would appear, basically, as a ramp of the tool length. A thin layer would be spatially "smeared" so that its exact location, as well as its "true" transit time, would be hard to resolve. There is a need for improving the spacial resolution of acoustic logs.

Following Foster et al. (1962), we believe that a finer resolution can be gained from logs where measurements are repeated at every fraction of the source receiver separation. In this case the problem can be set in a straightforward manner using the discrete depth version of equation (1):

$$T_j = \frac{1}{N} \sum_{i=j-N+1}^{j} t_i \qquad (2)$$

In this equation, discrete depth intervals are taken to be the fraction of the tool length by which it is shifted between successive source firings. N is the number of discrete depth intervals over which the tool stretches. Again, t_i is the transit time of the i^{th} depth interval and T_j the travel time scaled to one discrete depth interval when the top of the tool is at depth j. Depth indices start at bottom.

2. Single-space travel time inversion

2.1 Exact inverse

When the tool is run from depth 0 up to depth n, we can set a linear system of equations such as :

$$N.T_0 = t_{1-N} + t_{2-N} + \cdots \qquad \cdots + t_{-2} + t_{-1} + t_0$$

$$N.T_1 = t_{2-N} + t_{3-N} + \cdots \qquad \cdots + t_{-1} + t_0 + t_1$$

$$N.T_N = t_1 + t_2 + \cdots \qquad \cdots + t_{N-2} + t_{N-1} + t_N$$

$$N.T_n = t_{n-N+1} + t_{n-N+2} + \cdots \qquad \cdots + t_{n-2} + t_{n-1} + t_n$$

This system has $n+N$ unknowns and n equations and is therefore underdetermined. If we know the first $N-1$ transit time values, then the system can be exactly inverted for the remaining unknowns. However, we shall show that this solution is not acceptable in practical situations.

Let us assume that we have obtained the true transit time series up to depth $m-1$. We add an extra observation T_m and solve for t_m using :

$$t_m = N.T_m - t_{m-1} - \dots - t_{m-N+1} \tag{3}$$

Let us Z-transform both series, $T(Z)$ and $t(Z)$, with $Z=e^{j\omega}$.

$$t(Z)(1+Z^{-1}+\cdots+Z^{-N+1}) = N.T(Z) \tag{4}$$

We can solve for $t(Z)$:

$$t(Z) = \frac{N(1-Z^{-1})}{(1-Z^{-N})}.T(Z) \tag{5}$$

The transfer function obtained is precisely the inverse of the Z-tranform of the tool response. Therefore, we have designed the exact inverse filter. Such inverse filter presents $N-1$ poles at the frequencies : $\omega = \pi(k/N)$ for $k = 1,...,N-1$. In the ideal case where exact travel time readings are made, $T(Z)$ does not contain any energy at these frequencies and the poles should not perturb the inversion. We should be able to recover the true transit time series with the exception of the contribution of the frequencies at the pole locations. However, in a real case, measurement noise contributes to the travel time values. Consequently, the series T_j may contain a significant amount of energy at these frequencies. The exact filter applied to that data would infinitely amplify the noise content at these pole locations so that noise would dominate the output. Foster(1962) pointed out that the exact filter for this problem was useless.

From that discussion, we may conclude that in real world situations the measurement noise will significantly limit the depth resolution we may hope to reach. In order to attenuate this effect, more equations need to be added to the system of equations. Hence, we shall have an over-determined system of linear equations that will require a least squares solution.

When dealing with multi-source and multi-receiver tools, extra constraints are naturaly provided by the other travel time measurements. Inverting the whole resulting system is, basically, the solution proposed by

Willis (1983). However, if we are to invert for a large section of the formation, this inversion scheme requires, unfortunately, the handling of large matrices. Moreover, assuming that the problem has been solved for the first n depths, the question is whether the whole system should be inverted again if we add one extra observation ?

These remarks apply to our present single spacing inversion problem. Therefore, in the following, we shall seek constraints that can be added to our problem, and also be looking for a least squares solution of the resulting over-determined system that can be computed recursively.

2.2 Recursive least squares inversion formulation

A look at any section of sonic logs shows the vertical sequentiality of the physical characteristics in a sedimentary section.

In order to transform this piece of information into analytical constraints for our inversion problem, we recast the whole problem in terms of a stochastic process. The transit times and the travel times will be considered as random variables. Their depth series can be viewed as stochastic processes. We chose an independent increment process to represent the behavior of the depth sequence of the t_j's. That is,

$$t_{j+1} = t_j + w_j \tag{6}$$

In this equation, w_j is assumed to be a zero mean white noise process independent of t_j. Testing on real and synthetic data have shown that acceptable results can be obtained with equation (6). The word "noise" should not mislead the reader. w_j represents the departure from a homogeneous formation. It is characterized by a variance q_j. This variance is a measure of the variability of the formation. Large variances (several orders of magnitude larger than the measurement error variance) will indicate that equation (6) is not a good representation. On the other hand, small variances denote that little variation is expected in the formation. Finally, we understand that q_j represents an *a priori* knowledge we may have of the formation and how it can be weighted gradually.

At this point, let us perform some formal changes which will not affect the generality of our discussion :

$$\text{Let} \quad \bar{t}_j = \begin{bmatrix} t_j \\ \cdot \\ \cdot \\ t_{j-N+1} \end{bmatrix} \quad , \quad h = \begin{bmatrix} 1/N \\ 1/N \\ \cdot \\ 1/N \end{bmatrix} \quad \text{and} \quad F = \begin{bmatrix} 1 & 0 & 0 & 0 \\ 1 & 0 & 0 & 0 \\ 0 & 1 & \cdots & \cdots \\ \cdots & \cdots & 0 & 0 \\ 0 & 0 & 1 & 0 \end{bmatrix}$$

Then, our transit time depth sequence is ruled by :

$$\bar{t}_j = F\,\bar{t}_{j-1} + \bar{w}_j \tag{7}$$

The original system of equations can be re-created by successive applications of :

$$T_j = h^T \bar{t}_j + v_j \tag{8}$$

where h^T is the transpose of matrix h. v_j is the noise due to reading errors. Assume v_j is white noise with covariance R_j. The covariance matrix, $Q_j = E[\overline{w}_j \overline{w}_j^T]$ characterizes $\overline{w}_j$. Its only non zero entry is the first one in the first row: q_j.

Our present specific problem is to estimate, or invert, for n successive values of $\bar{t}_j$ given n successive measurements or observations T_j related to the $\bar{t}_j$'s through equation (8), under the n linear constraints of consecutive equations (7). In addition to its better constrained nature, the structure of this problem yields estimate computations that can be organized conveniently in a recursive algorithm. This is the Kalman filter.

Kalman filter formulation :

The remainder of this section will be devoted to the Kalman model formulation.

Two equations define the model :

$$\bar{t}_j = F(j)\, \bar{t}_{j-1} + G(j)\, \overline{w}_j \tag{9}$$

$$\overline{T}_j = H(j)\, \bar{t}_j + \bar{v}_j \tag{10}$$

Notations are explained hereafter.

Equation (9) represents the time dependent behavior of a linear dynamic system. The system is completely characterized by its state vector $\bar{t}_j$. Matrix $F(j)$ linearly relates the two successive state vectors at time j and $j-1$. It is also driven by the input $\bar{w}_j$ which, in this application, is a white noise with covariance Q_j . This matrix expresses the confidence we have in this finite difference equation. Matrix $G(i)$ allows the input vector $\bar{w}_j$ to be linearly transformed before acting on the state vector $\bar{t}_j$. Following Control Theory terminology, this equation, as well as its counterpart in our present problem, equation (7), will be referred to as the **State equation.**

We perceive the dynamic system only through periodic measurements. The vector of observations, $\bar{T}_j$, is linearly related to the state vector via matrix $H(j)$ in equation (10). Moreover, the measurement is corrupted by a white noise $\bar{v}_j$ of covariance R_j. R_j is related to the confidence we have in those measurements. This equation will be referred to as the **Measurement** or **observation equation.**

As for any linear system described by a recursive equation, the initial state has to be known. Here, it is specified through the mean and covariance of $\bar{t}_0$. Additional assumptions regarding the independence of the various stochastic processes are to be made. Namely, the noises $\bar{v}_j$ and $\bar{w}_j$ are to be independent of $\bar{t}_0$. Moreover, at a given time both noises are uncorrelated and each, taken at two different times, presents values that are uncorrelated. Figure 2 summarizes the different filter inputs.

The estimate of $\bar{t}_j$, $\hat{t}_j$ which minimizes the error covariance $E[(\hat{t}_j - \bar{t}_j)(\hat{t}_j - \bar{t}_j)^T]$, is $E[\bar{t}_j \mid \bar{T}_j, \ldots, \bar{T}_0]$, the conditional expectation of $\bar{t}_j$ given all past and present observations. This estimate is a linear function of the observations when all random variables are Gaussian. However, when this is not valid (probably our case), the linear function obtained in the Gaussian case still yields the minimum of the error covariance in the set of all possible linear estimators. This is the linear least squares estimator. In the following, $E[X \mid Y]$ is used as the linear least squares estimator of X given Y.

Given the model (equations (9) and (10)) and the related assumptions described previously, the problem solved by Kalman is to provide $\hat{t}_j$, the linear least squares estimate of $\bar{t}_j$ given the measurements $\bar{T}_0$ through $\bar{T}_j$. Basically both the estimate $\hat{t}_j$ and its error covariance are propagated in time through a two step recursion. We first define some notations to differentiate between the two steps :

$$\hat{t}(j \mid j-1) = E[\bar{t}_j \mid \bar{T}_{j-1}, \ldots, \bar{T}_0]$$

and $$P(j \mid j-1) = E[\,(\,\bar{t}_j - \hat{t}(j \mid j-1)\,)\,(\,\bar{t}_j - \hat{t}(j \mid j-1)\,)^T\,]$$

$$\hat{t}_j = \hat{t}(j \mid j) = E[\bar{t}_j \mid \bar{T}_j, \bar{T}_{j-1}, \ldots, \bar{T}_0]$$

and $$P(j \mid j) = E[\,(\,\bar{t}_j - \hat{t}(j \mid j)\,)\,(\,\bar{t}_j - \hat{t}(j \mid j)\,)^T\,]$$

The state equation is fruitfully employed to propagate the estimate from time $j-1$ to the next time increment using the same set of observations. Thus a prediction of $\hat{t}_j$ is made: $\hat{t}(j \mid j-1)$. This estimate of $\hat{t}_j$ is based on the first j observations. The measurement at time j then adds a new piece of information that is decomposed into a predictable part and an innovative part, which helps correct the prediction through a gain factor $K(j)$ and yields the corrected estimate $\hat{t}(j \mid j)$. For the sake of clarity we omitted the possible time dependence for the matrices F, G and H. The recursion is as follows:

Step (0) : initialization

$\hat{t}(0 \mid -1)$: guess of the initial "true" transit times

$P(0 \mid -1)$: confidence we have in this guess.

Step (1) : correction

$$\hat{t}(j \mid j) = \hat{t}(j \mid j-1) + K(j)\nu(j);\ P(j \mid j) = P(j \mid j-1) - K(j)\ H\ P(j \mid j-1);$$
$$K(j) = P(j \mid j-1)\ H^T[H\ P(j \mid j-1)\ H^T + R_j]^{-1};\ \nu(j) = \bar{T}_j - H\ \hat{t}(j \mid j-1).$$

Step (2) : prediction

$$\hat{t}(j \mid j-1) = F\ \hat{t}(j-1 \mid j-1);\ P(j \mid j-1) = F\ P(j-1 \mid j-1)\ F^T + G\ Q_j\ G^T.$$

These equations can be directly programmed with the matrices defined for equations (7) and (8) to solve our problem.

2.3 Synthetic results

Let us test our processing to illustrate the relevance of the various filter inputs. We modelled first the case of a tool with N=5. This may correspond approximatively to a 2' 5'' spacing tool shooting at 1/2 foot intervals.

The tool has been moved across a sharp interface between two homogeneous layers. They are characterized by transit times of 100 and 150 units respectively. Time units are arbitrary since all time measurements have been scaled to the same unit length. The resulting noise free travel time data is displayed Figure 3. Numbers of discrete depth intervals have been reported on the horizontal axis.

[1] The noise free data set is filtered. Outputs for various parameters Q and R are displayed in Figure 4. Q has been kept at a constant value of 1000. while R has been decreased from 10000. down to .01. Results of the least squares processing vary from a smooth and slowly rising curve (a), to somehow noisier and quicker rising curves (b) and (c), and, finally to the exact initial model (d). Keeping R constant at the value of .01 and decreasing Q from 1000. down to .001, in order to achieve the same ratios Q/R as in the previous figure would yield exactly the same results

respectively. It suggests that the result of the least squares inversion depends uniquely on the ratio of expected formation variability to expected noise variance in the data (Q/R ratio).

[2] Observations of Figure 3 have been corrupted by a random additive perturbation with a maximum amplitude of 7 arbitrary units. Figure 5 displays the results of the least squares inversion for the same four Q/R ratios as in Figure 4. Curve (a) is similar to its counterpart in Figure 4, while the remaining ones are much noisier. The same general trend can be noted : Curves vary from a smooth and slow rise to a quick but noisy rise with increasing Q/R ratio. However, this time the exact model has not been inverted and the corresponding curve (d) is very noisy.

[3] Let us try to understand the meaning of the ratio Q/R.

For a high Q/R ratio, the result is mainly affected by the noise content of the data. No *a priori* knowledge of the formation is input and even a large variability is expected. The filter gives more weight to the data and merely uses the state equation. It responds quickly to the step input but shows a high noise content. This is the *quick Kalman filter* case. In the limit, for an infinite ratio, the state equation is ignored and only the observations are used. This case corresponds to the exact inverse filter developped section 2.1 : A noise free data set yields the exact model whereas an inversion performed on noise corrupted data blows up the noise content.

For a small Q/R ratio, the result is a smoothed version of the original model. One does input a more or less valid *a priori* knowledge : Given that the formation velocity is V at depth i, it is very unlikely that a much smaller or greater velocity than V comes up at depth $i+1$. The filter gives more weight to the state equation and smoothes out the noise. The noise content is small, the resolution poor. This is the *slow Kalman filter* case.

These considerations underline a trade-off between noise reduction and resolution. The filter will determine a real variation in the transit times for which we invert only if the variations in the data set are *more likely* to be due to formation variability (given specification of Q) than to noise corruption (given R).

2.4 Real data results

In this section, this formulation is tested on real data. A sonic log has been recorded by a 2' 5" spacing Schlumberger probe. Spatial sampling of the formation is 1/2 foot. The length of the discrete response function of the tool is taken to be 5.

Figure 6 displays four transit time curves ordered by increasing spatial resolution. Curve (b) is the original data and the remaining ones are outputs of recursive least squares processings for different state noise specifications, Q. R has been kept at a value of 10, while Q has been increased from 10 (a), to 100 (c), up to 1000 (d). From (a) to (d), bed boundaries are sharper and more details are available to the interpretor. These results are consistent with our discussion in section 2.3 : As resolution increases, measurement noise is amplified and it becomes difficult to discriminate between noise contribution and very thin layering.

A 200' of a thinly layered section from the same well is analysed. Figure 7 displays the original data (b) as well as outputs of recursive least squares processings. As previously, the error measurement variance, R was kept constant at 10 and Q was varied. This time, Q was pushed even further up to 10000. In this case, as expected, noise dominates the resulting log (e). The same general remarks as in Figure 6 can be made.

2.5 Steady states

Kalman filtering is computationally time consuming. However, one could compute and store the gains $K(j)$ and error covariances $P(j|j)$ ahead of time. In doing so, one would quickly notice that for Q and R parameters kept constant in the computation, the gain vector and the covariance matrices converge toward constant vector and matrices. Moreover, these constant values do not depend on the initial state covariance input, $P(0|-1)$. Erroneous initial guesses also are corrected. This shows that the filter reaches a steady state which uniquely depends on Q/R.

A steady state would enable the user to apply a constant gain K. The resulting process would no longer be optimal in terms of minimizing the error covariance, but, after some time, it would be very near optimality. The steady state approximation would be a more computationally efficient process to apply and just as quick as any finite response filtering. Appendix A investigates the conditions under which a steady-stade filter exists. Spatial resolution of such filters are also considered.

2.6 Data adaptive filtering

[1] In all results presented here, we have kept R and Q constant. Nevertheless, it must be remembered that this is not a limitation of the method, only a choice made for the sake of greater simplicity. We can vary the R and Q values in the course of the algorithm without any change. Doing so would amount to designing an *adaptive* filter. This is one of the most appealling features of Kalman filtering as opposed to Wiener filtering for instance.

[2] What is the meaning of changing Q and R during an inversion ? Usualy, one would expect the error measurement characteristics to remain stationary. On the other hand, it seems natural to expect characteristics of the transit time series to vary. In particular, it is a common knowledge that large sections of formation can be decomposed into smaller units with similar physical characteristics. These may correspond, for instance, to stratigraphic or geologic units or, at a smaller scale, to homogeneous

layers. At the boundary, major changes occur and produce a "sharp" interface. In this case, the increment between consecutive transit time values across the interface is large compared to the increments within each unit. Modelling the transit time series as a random walk with increments of constant value would be an erroneous assumption and would prove to over-smooth the interface as we have seen in the previous examples (Figure 4). A better model would be to localy increase the variance of the state noise, Q, at the level of the sharp interface.

An histogram of the increments between successive transit time values is clearly non gaussian. However, it is not unrealistic to consider the observed distribution as resulting from a mixture of two distributions. The most frequent one would be characterized by a small variance and correspond to small increments within a same unit. The other one would characterize increments across sharp interfaces and present a larger variance. This analysis is conceptually similar to some studies conducted on the statistical distribution of reflection coefficients in surface seismic.

From a more prosaic point of view, varying Q means that we do not have the same confidence in the state equation everywhere. We do not wish to always input the same *a priori* knowledge into the inversion. As a result of this, we might expect an even better resolution of sharp interfaces without increasing the noise content everywhere on the log. In other words, once we have decided on a given resolution/noise-reduction trade-off, we do not have to stick with it until the inversion is done, as we would in the case of a damped least squares inversion of the whole system.

[3] The difficulty in designing an adaptive inversion scheme consits of finding an efficient criterion that will trigger variations in the Q and R specifications at the right location. It seems natural to focus our attention on the discrepancies between measurements and predictions. These are characterised by the innovations, $\nu(j)$, as computed in Step (1) of the algorithm in section 2.2. Locally, a high innovation denotes the innacuracy of the previous prediction step. One might expect then a large formation change. In certain cases, especially when processing large sections of data, it might be desirable to refer that quantity to a data dependent knowledge that has been previously acquired in the course of the inversion. For instance, the sample variance of the innovation series may be used to scale innovations.

Consequently, the state vector is predicted first ($\hat{t}(j \mid j-1)$) and the corresponding innovation evaluated. The ratio of the squared innovation at the current depth (j) to the sample variance of the innovation computed up to this depth may be calculated. Comparing this ratio or the squared innovation to a pre-determined threshold set by the user will determine which state variance is to be used in predicting the current error covariance ($P(j \mid j-1)$). Whenever, it passes the threshold a larger state variance, Q, is used.

[4] Let us see how does these considerations stand with our simple configuration used in 2.3-[3]. A step-shaped formation change is observed by a tool with N=5 and measurements are corrupted by a random additive perturbation with a maximum of 5 units. Our filter triggers a change in the Q value from 0.1 to 1000 whenever the squared innovation passes four times its variance. The output is displayed Figure 8 as a continuous curve. Results of processings with constant Q and R have been reported for comparison. R is kept constant at 1 for all curves. As a result of the adaptability, the initial model is nearly exactly inversed. Resolution of the interface is very good and the noise content is greatly reduced. In fact, spatial resolution is even better than that of the quick Kalman case (short dashed line). In the adaptative case, when a larger state variance is locally input, correction gain coefficients are perturbed and the first coefficient that applies to the first component of the state vector is suddenly increased so that the corrected estimate catches up the error made in the prediction. Even though, we specified the value of Q to be 1000 in both cases the local gain in the adaptive case is that of the transient state for Q equal to 1000 and corrects more the first component of the state vector than does the constant Q and R quick Kalman case that was already close to steady state when it reached the interface. These details will help in understanding some of the features associated with adaptive filtering namely, its tendancy to overshoot corrections.

A second synthetic example was run to show the filter ability to pick a thin layer. A small layer of two discrete depth interval thickness was embedded into a homogeneous formation after a sharp interface. The model is represented Figure 9-(a). The same tool and same error measurement as previously have been used to simulate field data (b). The thin bed is smoothed out. A slow Kalman filter is first used (c). Resolution is poor but the noise content is small. A quick Kalman filter (d) amplifies the noise and does a better job in locating interfaces. Finally, an adaptive filter is set to have the same Q value as the latter filter when the squared innovation passes five times its sample variance and that of the former elsewhere. This filter (e) resolves the thin layer in a better way than any of the other filters without increasing the noise content everywhere. We shall note the spike after the step as an example of over-shooting.

[4] We applied this type of filtering to the real data examples of Figure 6 and 7. In the first case, we set the adaptive filter to use a larger value for Q when the absolute value of the squared innovation passes a given threshold. Figure 10 displays output curves corresponding to the first real data example. Logs (a) and (e) are the original field log and the least squares processed log for Q and R set to 1000 and 10 respectively. We investigate the effect of lowering the threshold from 10 to 5 in (b) and (c) when Q is either 1000 or 10. As expected, more sharp interfaces are picked. At those interfaces sharp angles are observed. These are related to over-shooting as described before. The noise content after each sharp

interface in very small. In appendix A we define an "instantaneous resolution". We also show that, with this definition, the resolution produced by the transient state first increases at sharp interfaces beyond that of the steady state for Q set to 1000 and then decreases after the interfaces below that of the steady state for Q equal to 10, before reaching steady state. This produces clear-cut interfaces. In (d), we set Q to be either 1000 or 100. Consequently, we reduced the amplitude of the perturbation and avoided some of the previous features.

Figure 11 corresponds to the second real data example. The field log is curve (a). The adaptibility criterion is the same as previously with a threshold set at 50 for curves (b) and (c). In all three examples R is kept constant at 10. Q value is set at 10 except when discripancies are detected in which case it is increased to 100 in (b) and up to 1000 in (c) and (d). Instabilities seems to develop when passing from curve (b) to (c). This is due the higher Q value used in (c) which thin layering triggers more often. In (d) the criterion uses the ratio of the squared innovation to its sample variance with threshold set at 30. Q and R specifications are the same as (c). Instabilities are somehow removed together with a loss in spatial resolution toward the deeper end of the log. Actually, this is caused by a sudden increase of the current variance when the inversion arrives at the thinly layered section of the log, it artificially increases the level at which discrepancies trigger a state variance change.

[5] In these examples appeared the advantages as well as the drawbacks of using adaptive filters. We also saw how results could vary depending on the *a priori* knowledge input through the specifications set and the criterion employed. However, it should be remembered that criterion used are the simplest ones and that only two different Q are used. We would expect some improvements using more reffined criterions as well as Q values proportional to the observed discrepancy. Going any further in that direction would require from log analysts a better definition of the objectives to reach.

3. Multiple-space travel time inversion formulation

3.1 Extension to multiple spacings

The first two paragraphs of part 2.2 showed how we could bring our inversion problem in the case of a single spacing tool to a somewhat improved constrained problem. We then presented the formulation in a more general situation, in particular that of multiple observations. This showed that our inversion could easily be extended to multi-source, multi-receiver tools. To do that we only have to arrange equation (8) where the T_j's become column vectors with as many entries as off-sets to be considered, and h has to be turned into a matrix according to the tool configuration. Assuming it has an integral value, N will be equal to the length of the largest source receiver separation divided by the change in depth of the tool between two completed firing sequences.

Although formation variability and noise covariances can be depth dependent, we kept them at a constant value throughout subsequent applications, in order to simplify the problem and aid in the understanding of the process.

To use this inversion scheme we had to choose a tool configuration. We modelled the case of a two source/two receiver tool such as the one shown in Figure 12. Two sources are placed 2 ft apart at the bottom of the sonde, and two receivers are placed 2 ft apart at the top of the sonde. The distance between the lower receiver and the upper source is 8 ft. This configuration provides source-receiver separations of 8, 10, 10 and 12 ft for each firing sequence. We also assumed in all examples that a complete sequence of shots was fired at 1/2 ft intervals.

3.2 Least squares processing

With these specifications our state vector $\bar{t}_j$ has 24 entries. H is a 4 by 24 matrix to accommodate four measurements at every depth increment. The observation equation (8) becomes :

$$\bar{T}_j = H\bar{t}_j + \bar{v}$$

$$\bar{T}_j = \begin{bmatrix} T_j(10') \\ T_j(8') \\ T_j(12') \\ T_j(10') \end{bmatrix} ;$$

$$H = \begin{bmatrix} 1/20 & 1/20 & 1/20 & 1/20 & 1/20 & .. & 1/20 & 0 & 0 & 0 & 0 \\ 0 & 0 & 0 & 0 & 1/16 & .. & 1/16 & 0 & 0 & 0 & 0 \\ 1/24 & 1/24 & 1/24 & 1/24 & 1/24 & .. & 1/24 & 1/24 & 1/24 & 1/24 & 1/24 \\ 0 & 0 & 0 & 0 & 1/20 & .. & 1/20 & 1/20 & 1/20 & 1/20 & 1/20 \end{bmatrix}$$

We remember that our Kalman filter provides us with vector estimates of $\bar{t}_j$. The scalar function of depth estimates presented next will be the last entry of each state vector estimate. This means that we "wait" until the tool has been completely pulled above the corresponding depth before keeping the estimate. In other words, in order to estimate the formation's "true" transit times, we use the maximum of observations this formulation permits. Formally, the selected estimate will be :

$$E[t_j \mid \overline{T}_{j+N-1}, \ldots, \overline{T}_j, \ldots, \overline{T}_0]$$

3.3 Conventional processing

A conventional processing of the travel times from all four source-receiver combinations could :

(1) Consider all four possible common source and common receiver combinations and compute the Δt's corresponding to 2 ft intervals.

(2) Refer each Δt to the middle 1/2 ft layers in the 2 ft interval.

(3) Average all Δt's corresponding to the same 1/2 ft layer.

Note that in this case, each transit time determination will involve only 8 travel time measurements. We also expect the resolution of such processing to be limited to the smallest spacing, no matter how densely the formation is sampled. We are now ready to try both processes on synthetic travel time data.

3.4 Synthetic results

[1] Figure 13 displays synthetic travel time curves versus depth for the four source-receiver combinations in a sharp interface case. The time scale is arbitrary since all travel times have been scaled to a unique reference length. All transit time estimations will be scaled to that same reference length in order to ease comparisons. Numbers of discrete depth intervals of 1/2 ft have been plotted on the horizontal axis.

The four curves have been processed by both the conventional and recursive least squares methods. Outputs from both methods are shown in Figure 14.

The conventional processing has an effective resolution equal to the smallest source or receiver separation while the least squares processing inverts exactly for the transit time model discretized every 1/2 ft when input parameters Q and R specify that very little noise is expected in the data.

[2] We corrupted the travel time data of Figure 13 with a random additive perturbation having a maximum amplitude of 20 arbitrary units. In the resulting data set, shown in Figure 15, travel time curves are indistinguishable one from another.

The least squares inversion scheme was tried first. In Figure 16-(a) we kept the input parameter R at a constant value of 20, and increased parameter Q, which describes the formation variability, from a value of 0.1 up to a value of 300, ending with the dashed curve. The filter response to the step change in transit times varies from a slow and smooth change to a quick but noisy rise. Next, in Figure 16-(b), we started from the last Q and R specifications that yielded the dashed curve and progressively increased R, the observation noise variance, from a value of 20 up to 1000. The filtered output deformed back to a slow rising and smooth curve.

These results confirm the discussion in section 2.3. Results of the least squares processing depends mainly on the Q/R ratio specification. This ratio sets a choice in the noise reduction versus resolution trade-off.

[3] Figure 17 compares results of the conventional processing for that same noise corrupted data set with those of a quick Kalman filter case (note the slight change of scale from previous figures). The two are very similar. In other words, they depend greatly on the noise content of the data set. This suggests that, in terms of noise reduction, it is possible to do better with the help of some *a priori* knowledge than one can with conventional processing. Both cases have good spatial resolution of the sharp interface, but include variations that do not exist. A slower Kalman filter would not show any variation, unless given likely state/noise variance specifications.

We shall also note that measurement errors are more drastic than for the single spacing synthetic simulations. The longer spacing used as well as the number of different spacings yield more equations that help stabilizing the inversion in noise corrupted situations.

3.5 Role of initial guesses: Steady-state filter

Figures 18-(a) and 18-(b) investigate the consequences of starting the recursion with erroneous guesses in the case of a noise free data set and in a noise corrupted situation respectively. In both situations the filter corrects the error. The only difference is the time it takes to do so. As for single spacing filters, this is related to the existence of a steady state which depends only on the ratio Q/R. (See Appendix A for details). In this case, controllability is verified. Moreover, assuming observations are made in such a way as to involve all entries of the state vector at least once, observability is always guaranteed. (This last condition is sufficient but not necessary). Given our choice for a tool, we may conclude the existence of a steady-state filter.

3.6 Other synthetic examples

Figures 19 and 20 display results for three and four layer models respectively, involving thin layers of 5 ft and 2.5 ft thicknesses (note the change of depth scale in Figure 20). In all the cases presented, least squares inverses show a better noise reduction than their conventional counterparts.

It appears that recursive least squares inverses tend to under estimate transit time variations. Moreover, even in the case of a symmetric contrast such as in Figure 19, the inversion does not keep that feature. This is related to the causal nature of the Kalman filter. However, better estimates could be obtained by combining both forward and backward Kalman filters (Smith, 1975).

3.7 Real data example

We processed a 150 foot limestone section of travel time data. The tool configuration is that of Figure 12. Firing rate and logging speed are the same. Figure 21 displays one 10 ft offset travel time data scaled in $\mu s / ft$. (We had only one of the two 10 ft offset travel time determination available and we duplicated it with the correct shift of 2 ft).

Figure 22 shows results of the "conventional" processing. Outputs of least squares processings for various statistical specifications are presented in Figures 23, 24 and 25. Each one of these needs about 10 sec of cpu time to complete 50 depth increments on a VAX 11/780 with a non-optimized program. Statistical specifications are kept constant throughout the inversion. The expected formation variability, Q, is 100 for all three figures. The noise variance, R, is 1, 10 and 100 for Figures 23, 24 and 25 respectively.

As for inversions conducted on synthetic data, outputs of conventional and least squares processings are similar for a small value of R (quick Kalman filter case) except for differences in the sharpness and magnitude of some of the picks. The three least squares processings further illustrate the resolution/noise rèduction trade off discussed earlier and the need for an adaptive processing. In particular, the moderate resolutions obtained show that resolution is critically limited by the noise content of the data. Each one of these output curves corresponds to different hypotheses concerning the relative importance of the noise content versus the formation variability. Obviously, knowledge of the actual noise content prevents exaggerated smoothing out of the results. Still, even knowing its actual characteristics will not help the filter to discriminate between real formation changes and noise corruption.

4. CONCLUSIONS

As one can see from these examples, there is a need for a better definition of resolution. Resolving power is usually taken to be the smallest layer thickness one can distinguish in a homogeneous formation. This is also the ability of the output to rise promptly when a step function is input. This is true in noise-free situations. Nevertheless, resolution through noise corrupted data is a more complicated matter as underlined by the few examples presented in this study. Resolving a thin layer is important, but not showing a layer when there is none is also important. This is part of a well known trade-off that occurs in any estimation problem.

Least squares inversion provides us with a reliable way of obtaining reasonable answers to this problem using probabilistic constraints. It takes into account a very general piece of geological information -- the vertical sequentiality of physical parameters. It uses the best of the statistical redundancy that is not used normally in the case of a single spacing tool, and is poorly used in the case of multi-spacing tools.

The Kalman filter formulation makes processing affordable from the standpoint of storage size, and its great flexibility makes it a very powerful and promising approach. However, further work is needed to design an inversion process which would include borehole radius and would also be adaptable to large formation changes.

References

Foster, M., Hicks, W., and Nipper, J., 1962, Optimum inverse filters which shorten the spacing of velocity logs: Geophysics, 27, 317-326.

Jaswinski, A.H., 1970, Stochastic processes and filtering theory: Academic Press.

O'Doherty, R.F. and Anstey, N.A., 1971, Reflections on Amplitudes: Geophysical Prospecting, 19, 430-458

Sandell Jr., N.R. and Shapiro, J.H., 1976, Stochastic processes and applications, notes for subject 6.432, Department of EECS, Massachusetts Institute of Technology, Cambridge, Massachusetts.

Smith, P.L., 1975, Backward-Forward Smoothing Interpretation of the *A Posteriori* Process Noise Estimate, IEEE Trans. on Automatic Control.

Willis, M.E., 1983, Inversion of travel time for velocity : Annual Report of the Full Waveform Acoustic Logging Consortium, Earth Resources Laboratory, Department of EAPS, Massachusetts Institute of Technology, Cambridge, Massachusetts.

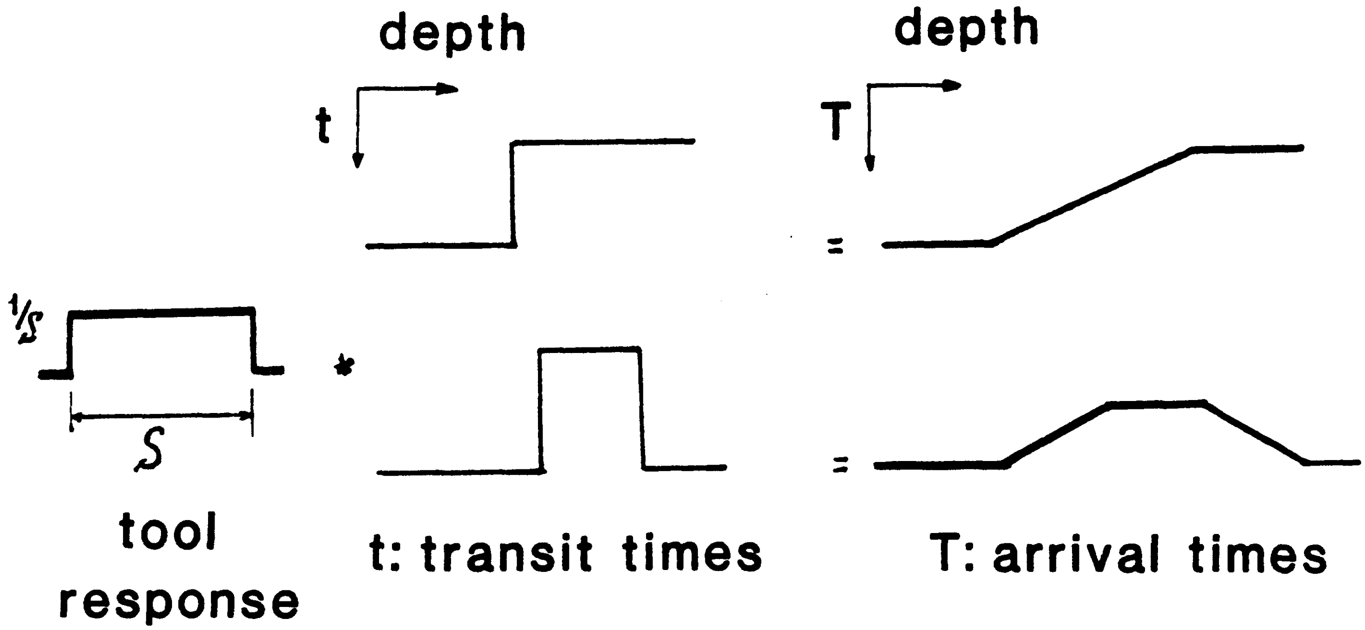

Figure 1 : Smoothing effect of the source-receiver separation on travel times in the cases of a sharp interface and a thin layer.

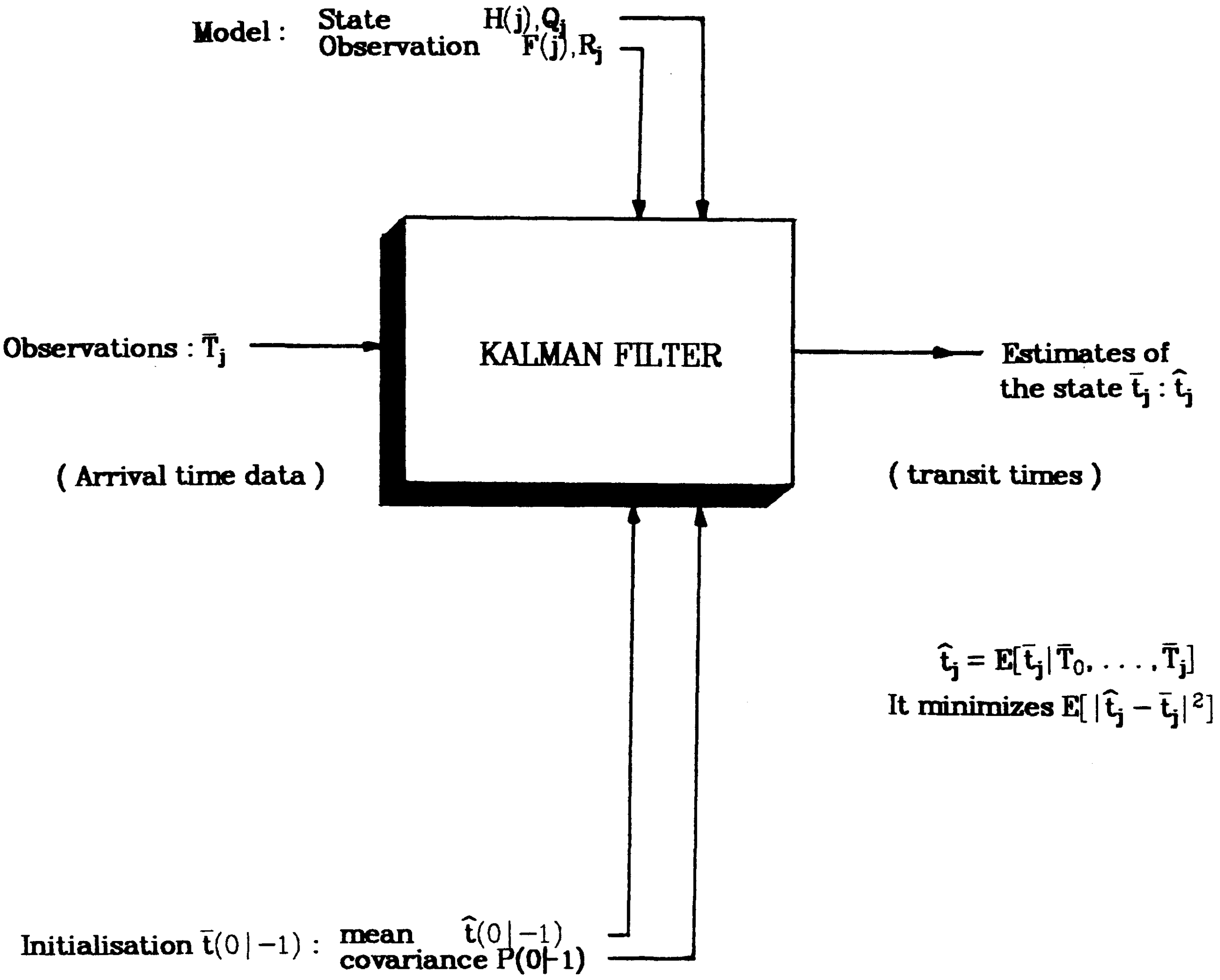

Figure 2 : Summary of the different inputs and initial specifications for Kalman filtering.

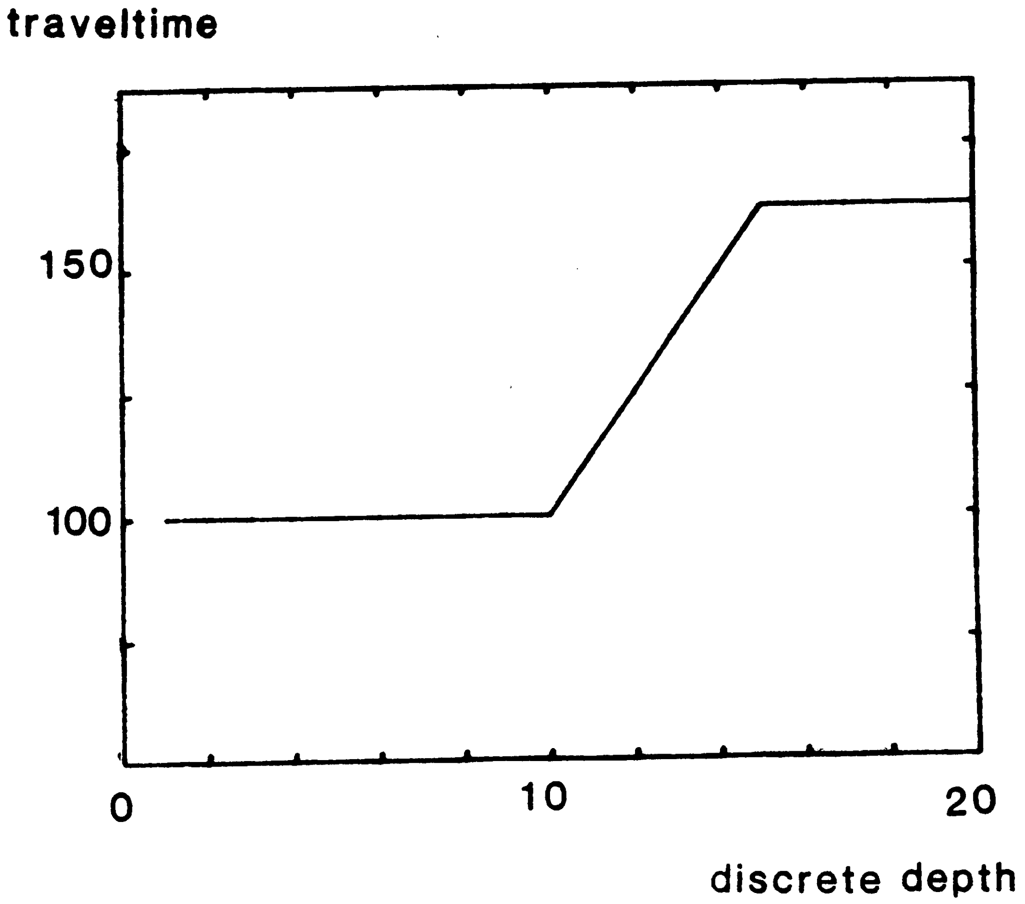

Figure 3 : Synthetic noise free travel time data simulated for a tool of length 5 ran across a sharp interface. Horizontal axis is in discrete depth interval number and the vertical axis is in time units scaled to an arbitrary reference length.

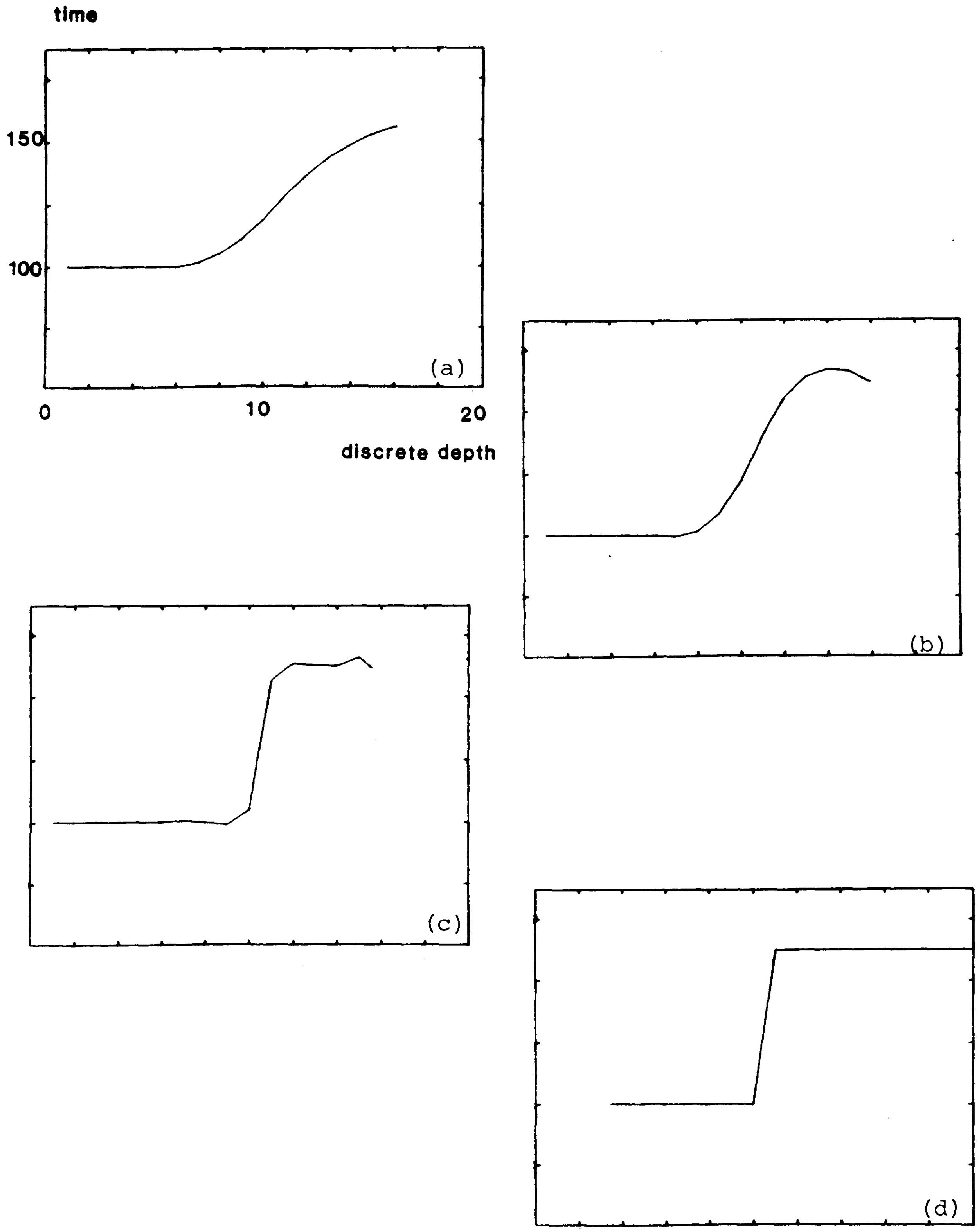

Figure 4 : Outputs of recursive least squares processings with the state variance, Q set at 1000. The error measurement variance, R is 10000, 100, 1 and .01 in (a), (b), (c) and (d) respectively. (d) is also the exact initial model.

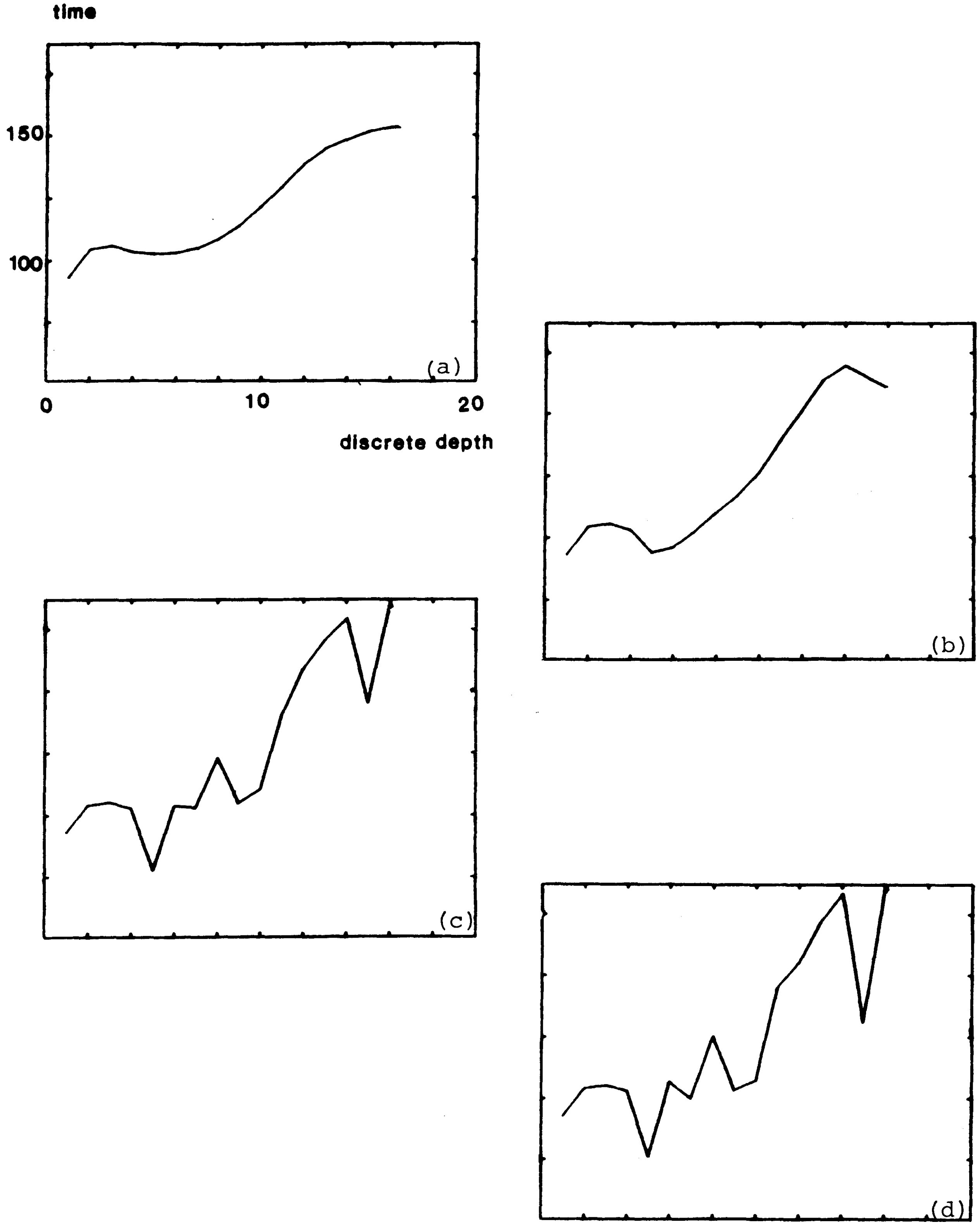

Figure 5 : Same as Figure 4 but with an additive random perturbation of maximum amplitude 7.

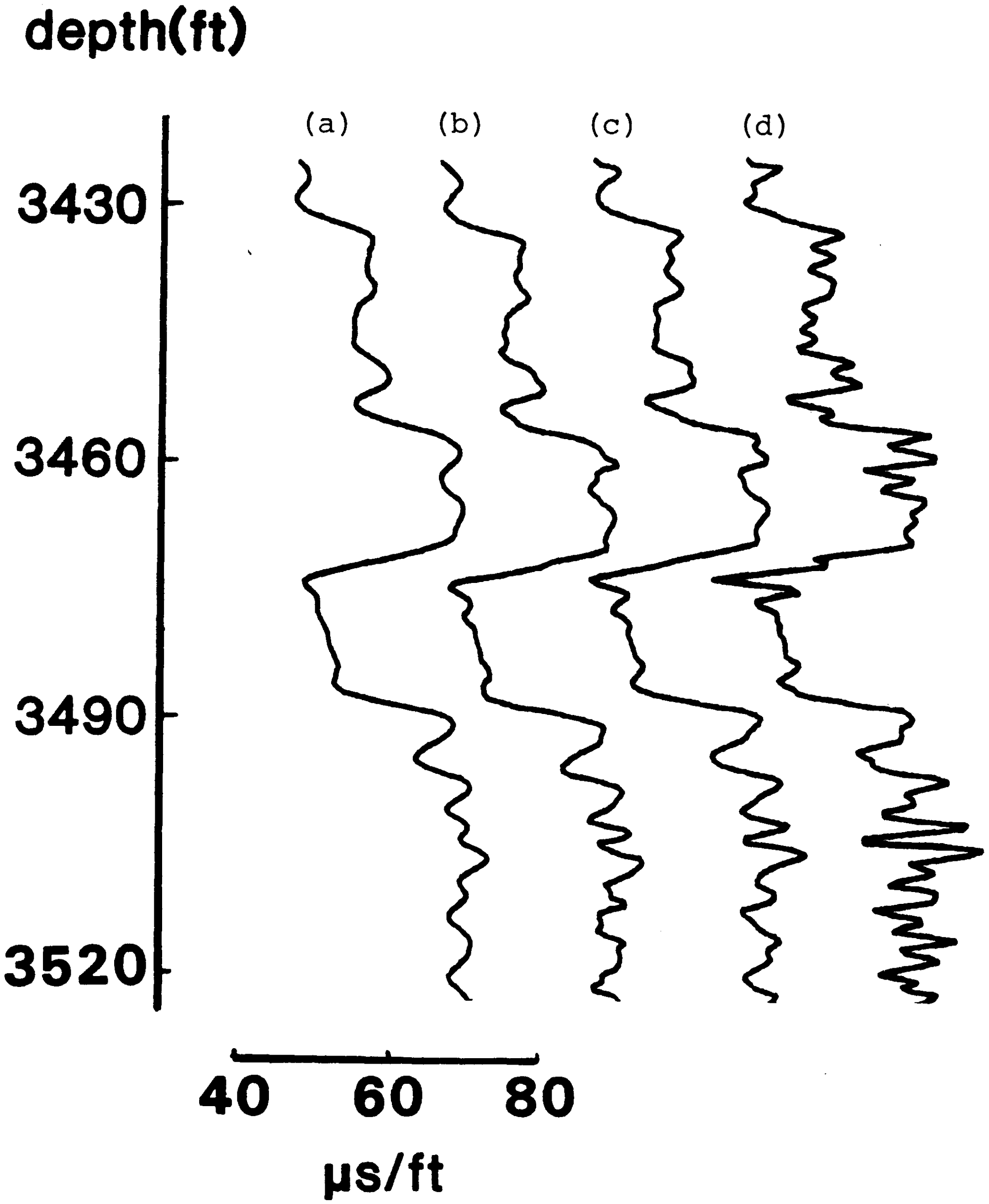

Figure 6 : Real data example(1). Original field log (b) and recursive least squares outputs (a),(c), and (d). R is kept at 10 in all three and Q equals 10 (a), 100 (c), 1000 (d).

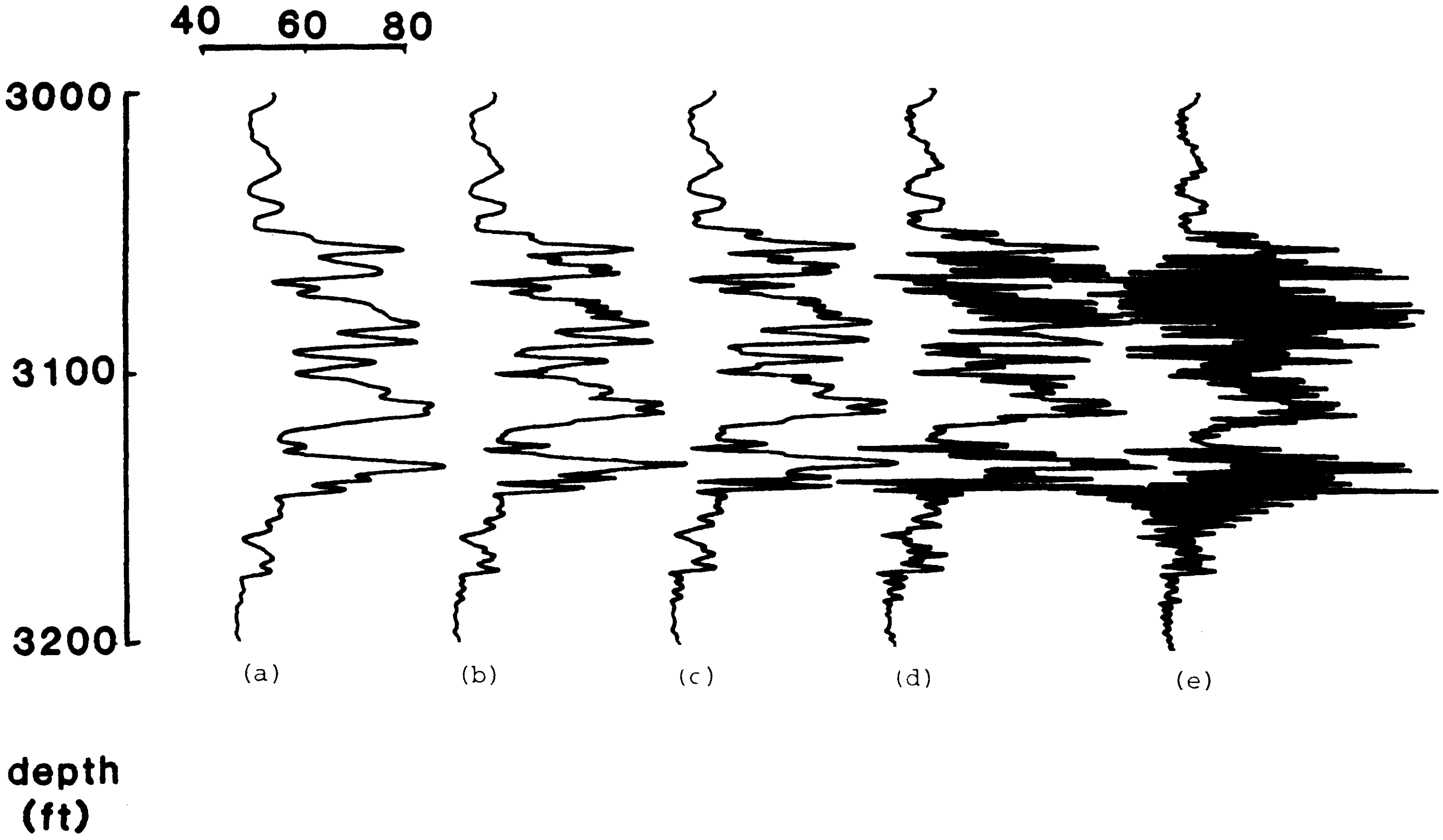

Figure 7 : Real data example(2). Original field log (b) and recursive least squares outputs (a),(c),(d) and (e). R is kept at 10 in all four and Q equals 10 (a), 100 (c), 1000 (d) and 10000 (e). In (e) the amplitude scale has been compressed a little.

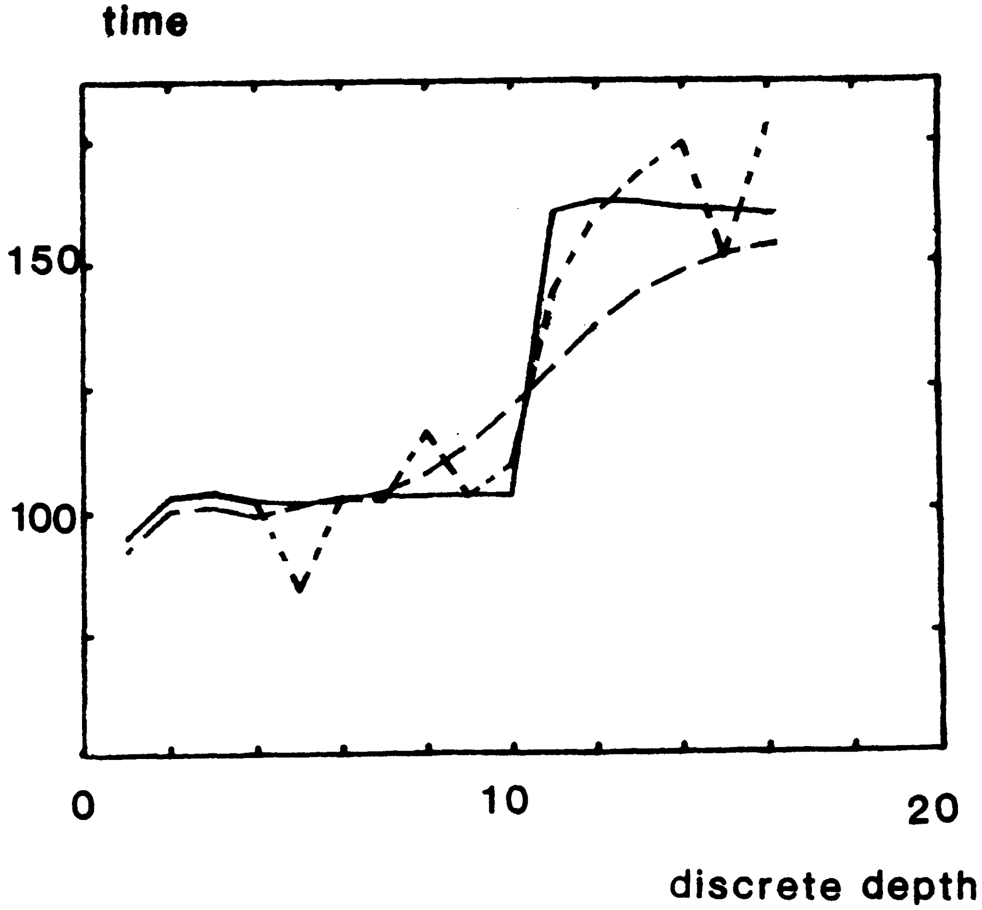

Figure 8 : Data adaptive filtering of the synthetic data of Figure 3, corrupted by a perturbation with a maximum amplitude of 5. R is kept constant at 1 in all three curves. Q is 0.1 everywhere except at the interface where it take the value of 1000 in the continuous curve. Q is kept constant at 0.1 in the long dashed curve. Q is kept constant at 1000 in the short dashed curve.

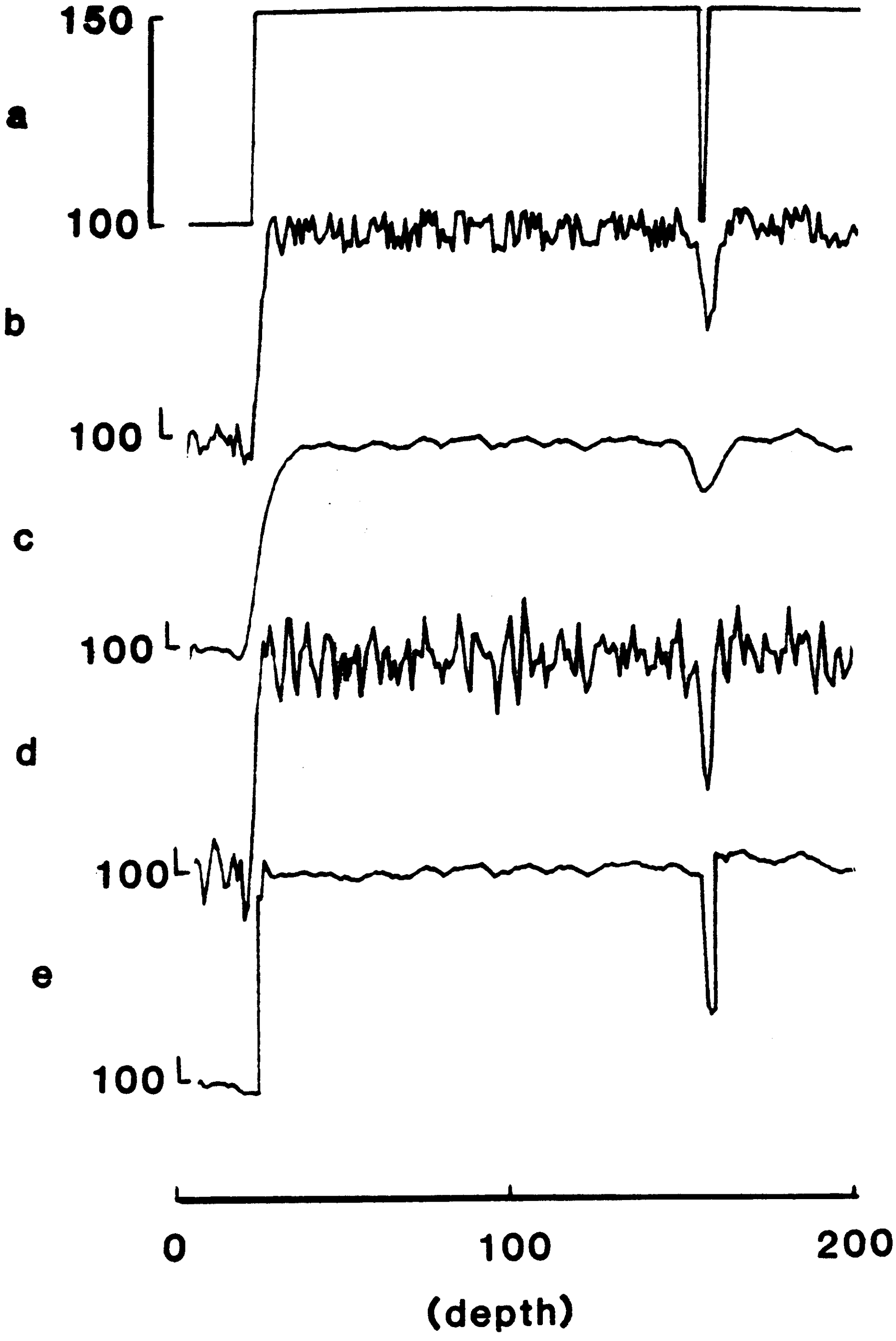

Figure 9 : Synthetic model with a thin layer. (a) Model, (b) Simulated recorded data for a tool of length 5 with a measurement noise error of maximum amplitude 5, (c) Output of slow Kalman filtering with Q/R set at 1/20, (d) output of quick Kalman filtering with Q/R set at 1000/20 and (e) data adaptive filtering with R set at 20 and Q either 1 or 1000.

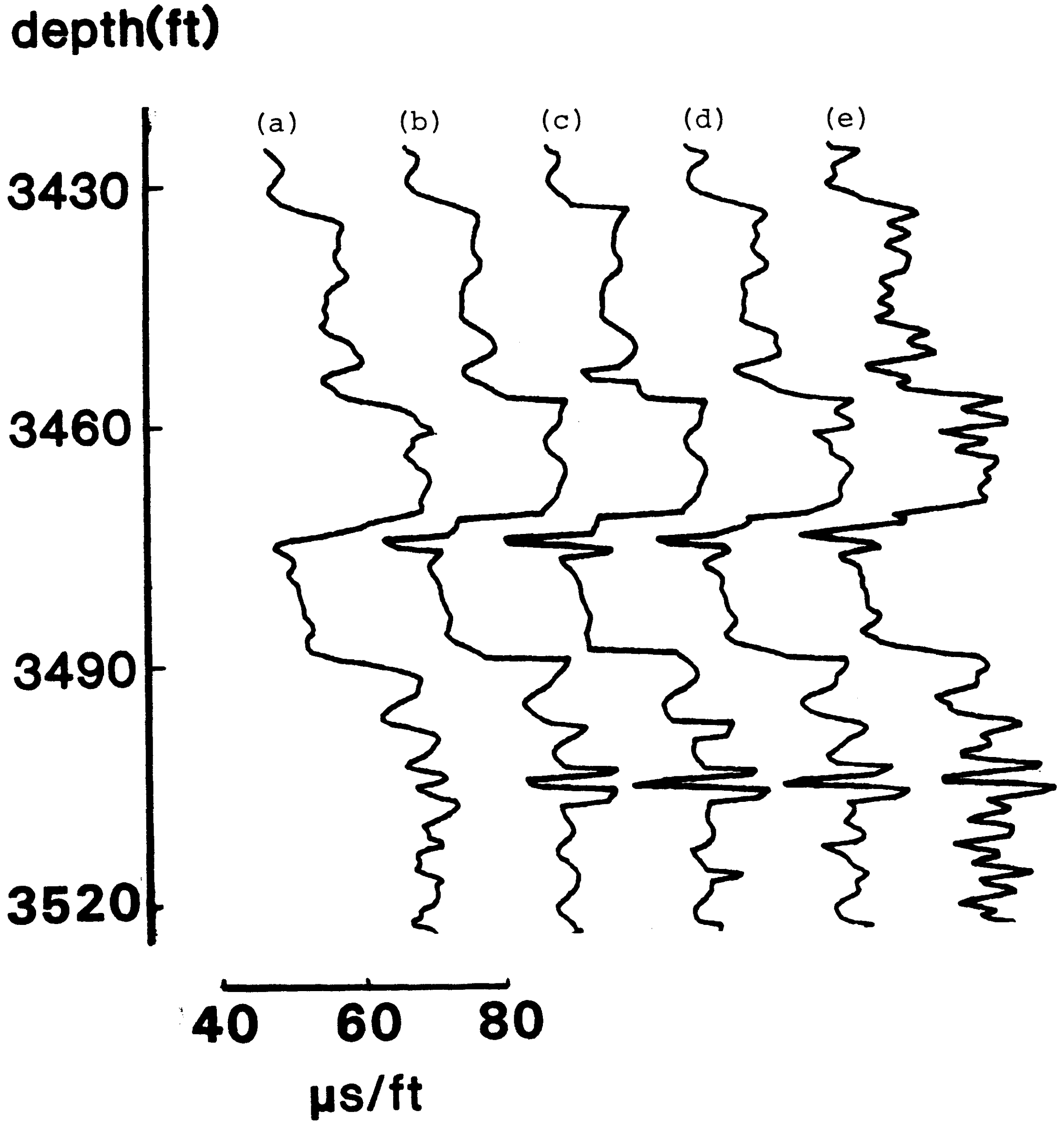

Figure 10 : Real data example (1). (a) original field log and (e) least squared processed log with Q/R set at 1000/10. R is 10 for all others. Q is either 10 or 1000 depending on the value of the squared innovation compared to a threshold value set at 10 in (b) and 5 in (c). In (d) Q is either 1000 or 100 with the latter threshold.

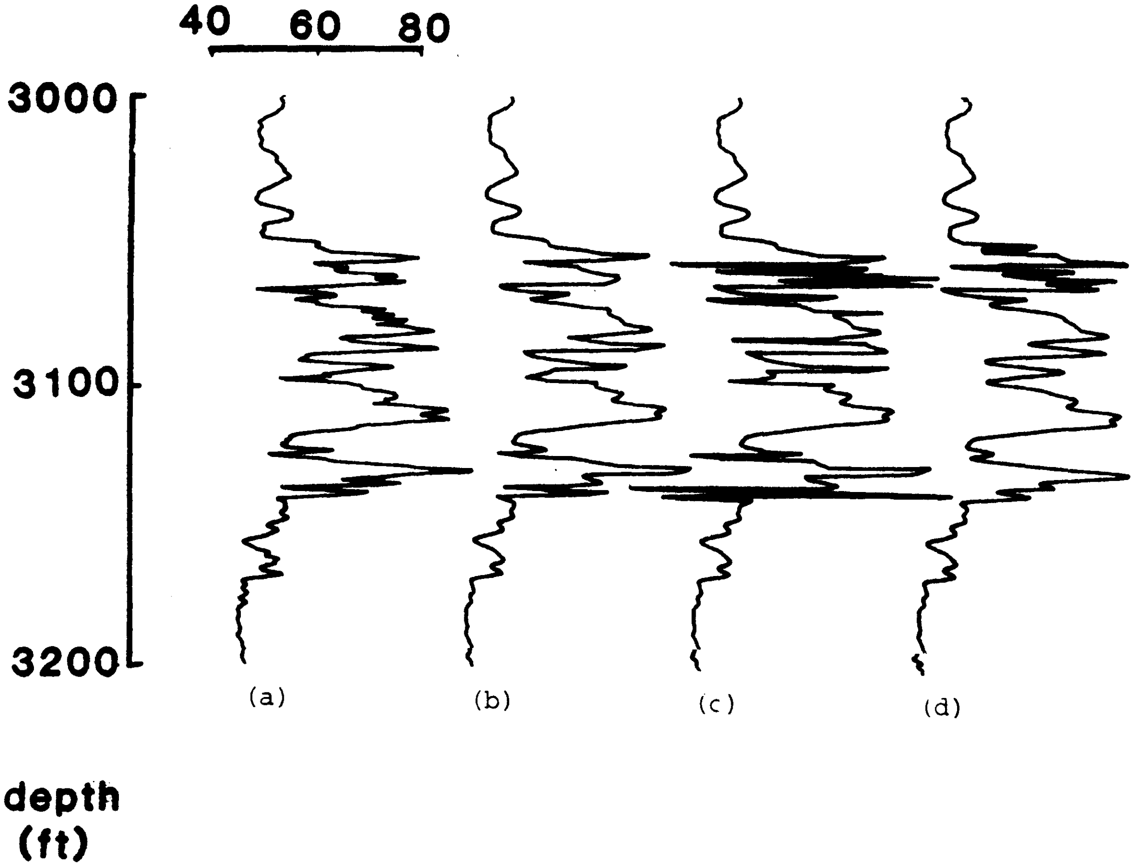

Figure 11 : Real data example (2). (a) is the original field log and the remaining ones are outputs of data adaptive Kalman filtering with R equal to 10. In (b) Q is either 100 or 10 depending on the value of the squared innovation compared to a threshold value of 50. (c) same criterion and same threshold but Q is either 1000 or 10. In (d) Q is allowed the same variations but a different criterion is used : the innovation is divided by its sample variance up to the current depth and then compared to a threshold value of 30.

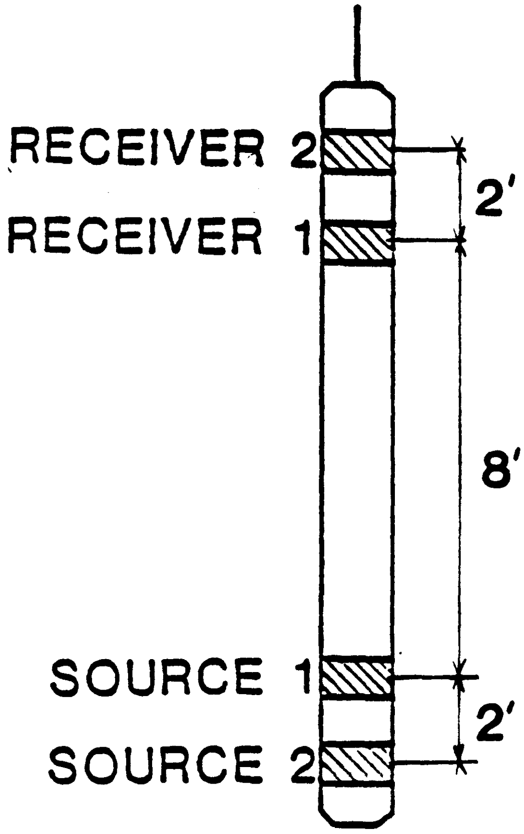

SPACINGS : 10' 8' 12' and 10'

A complete sequence is fired every 1 /2'

Figure 12 : Tool geometric configuration used for synthetic data.

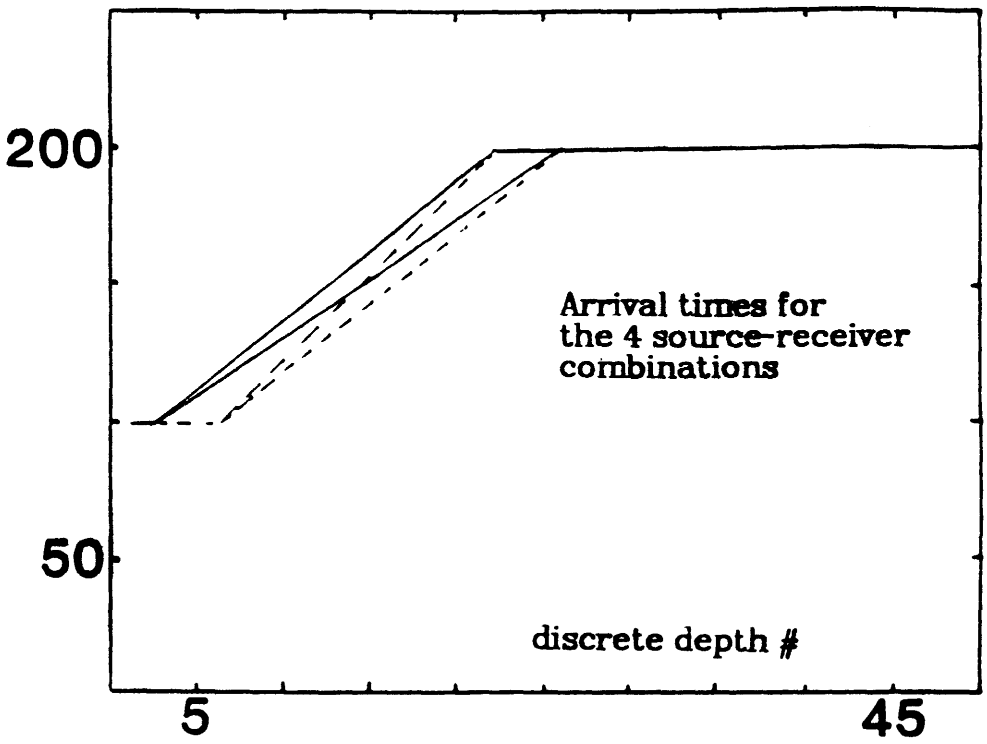

Figure 13 : Synthetic arrival-time curves for the tool of Figure 12 in the case of a sharp interface. Scale units are explained in the text.

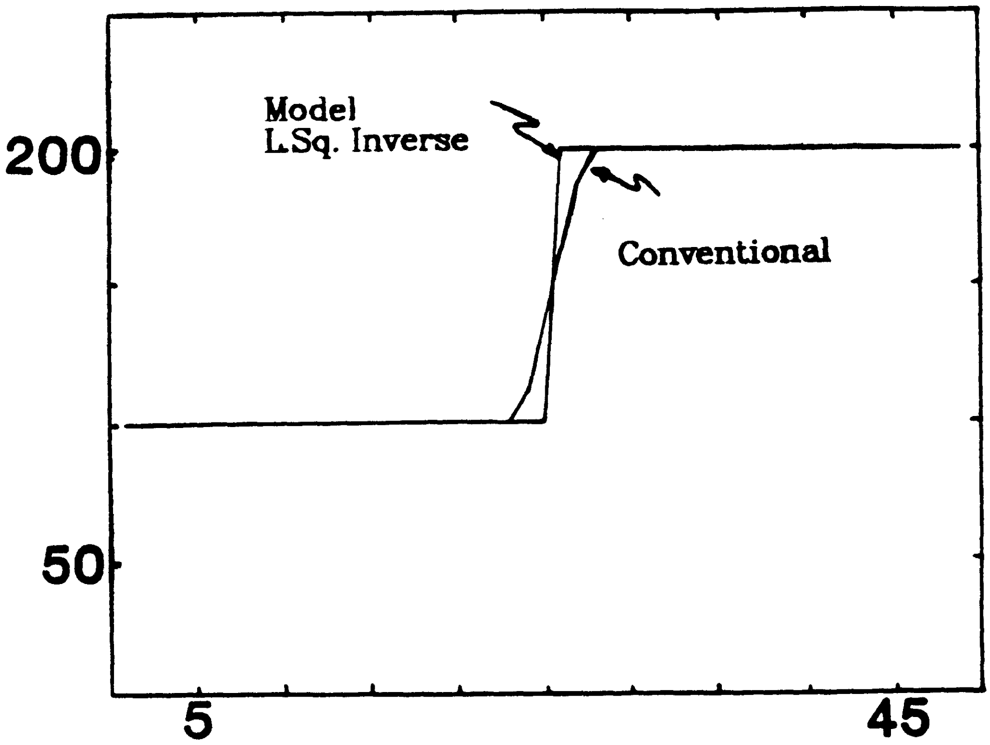

Figure 14 : Outputs of conventional and recursive least squares processing in the case of the noise-free data set of Figure 4.

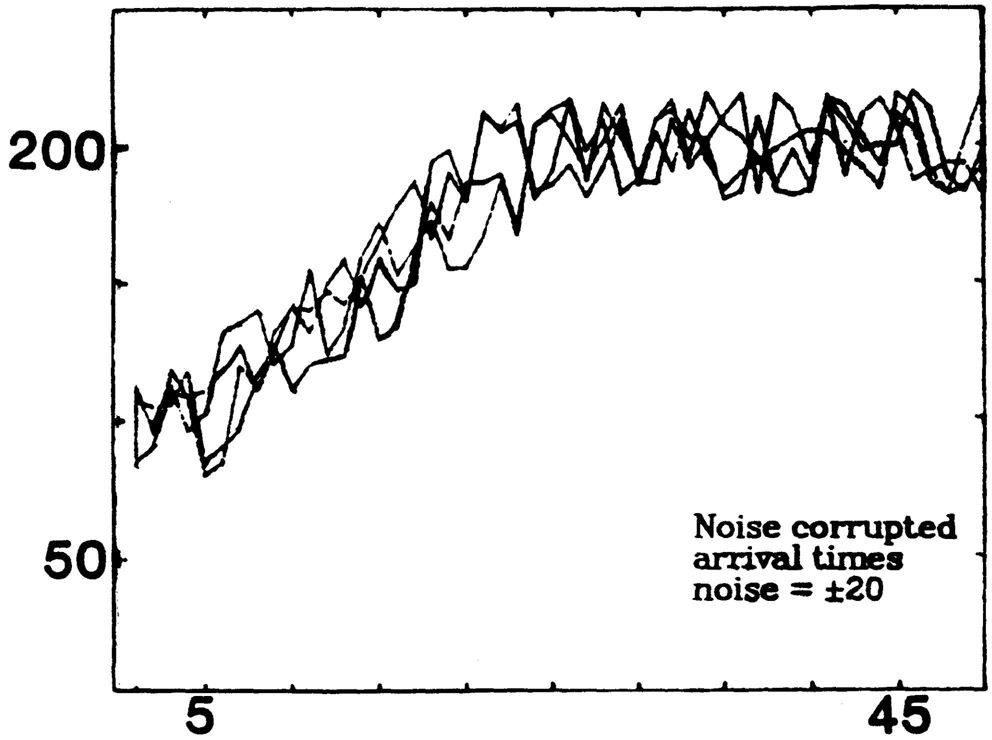

Figure 15 : Synthetic arrival-time curves of Figure 13 have been corrupted by an additive random noise of maximum amplitude 20.

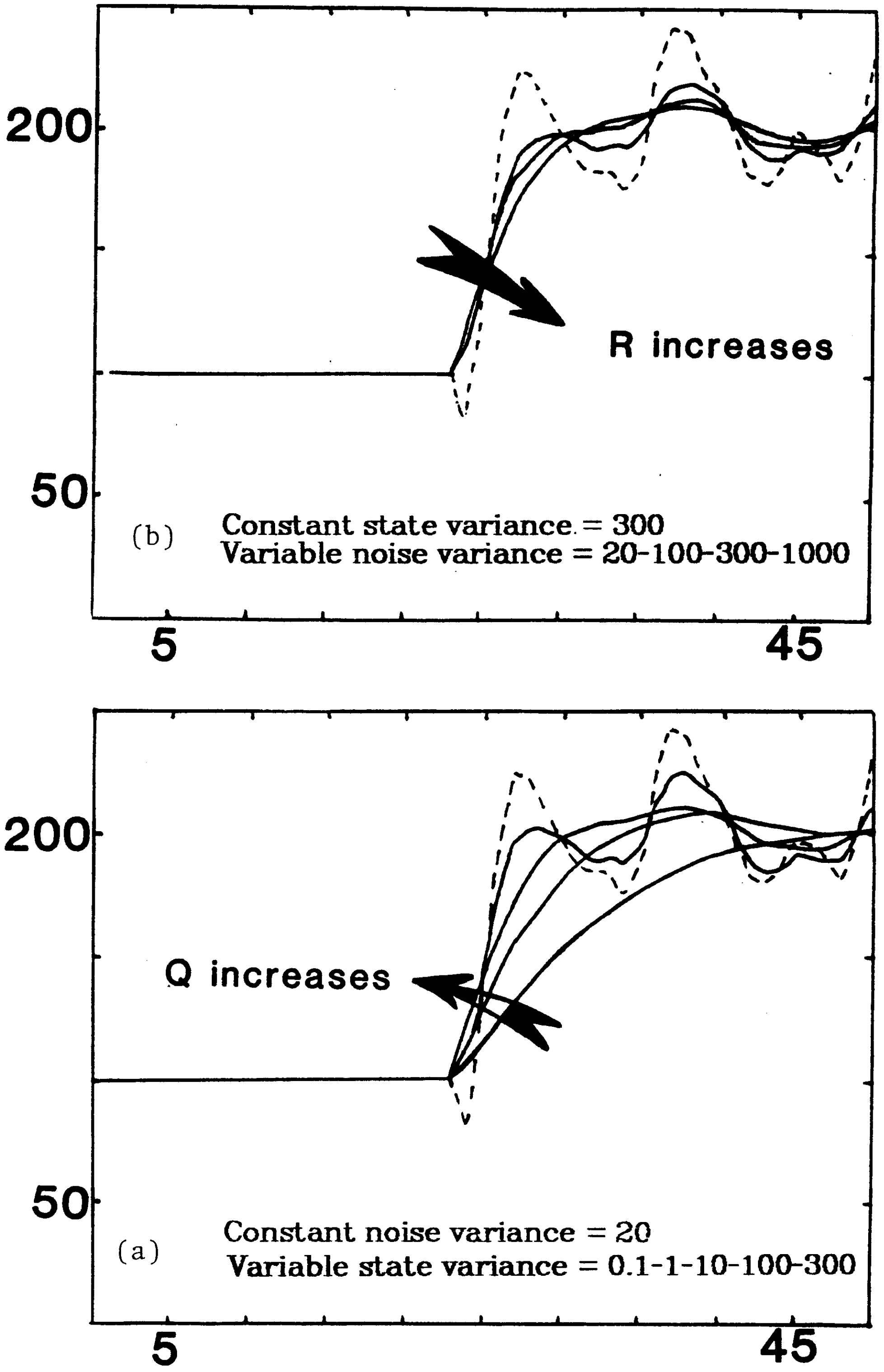

Figure 16 : Outputs of the recursive least squares processing for various noise specifications (Q and R). A correct initial guess has been assumed.
(a) R, the observation noise variance is kept constant, Q increases
(b) Q, the "expected" formation variability is kept constant, R increases
In both figures, the dashed curve is obtained with the same R and Q.

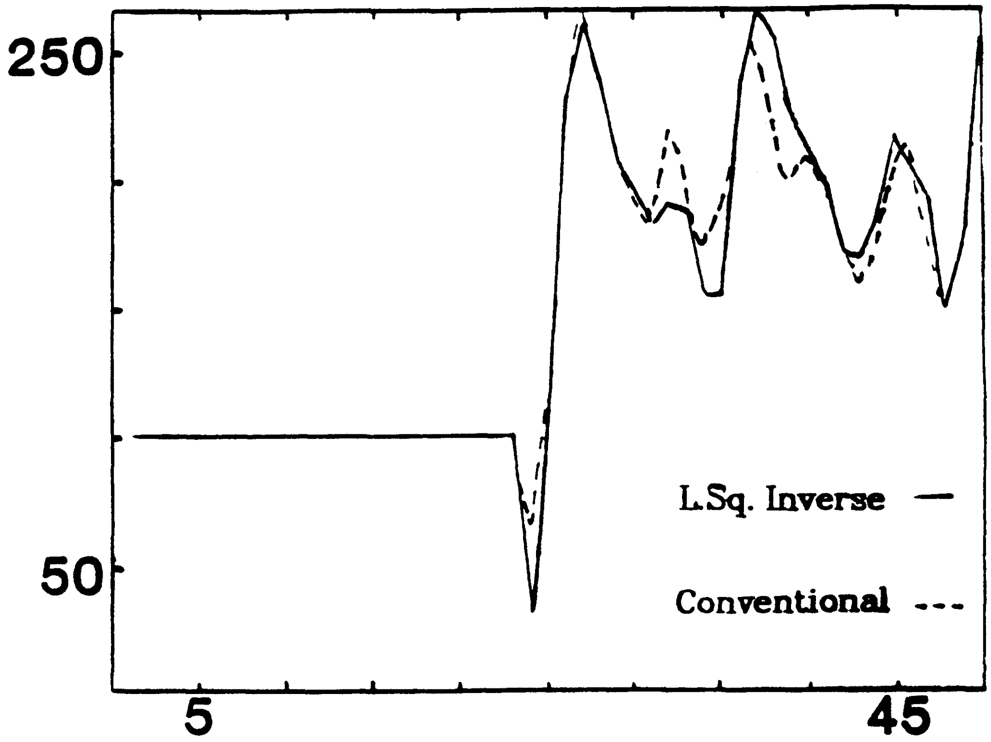

Figure 17 : Outputs of both conventional and quick Kalman processing.

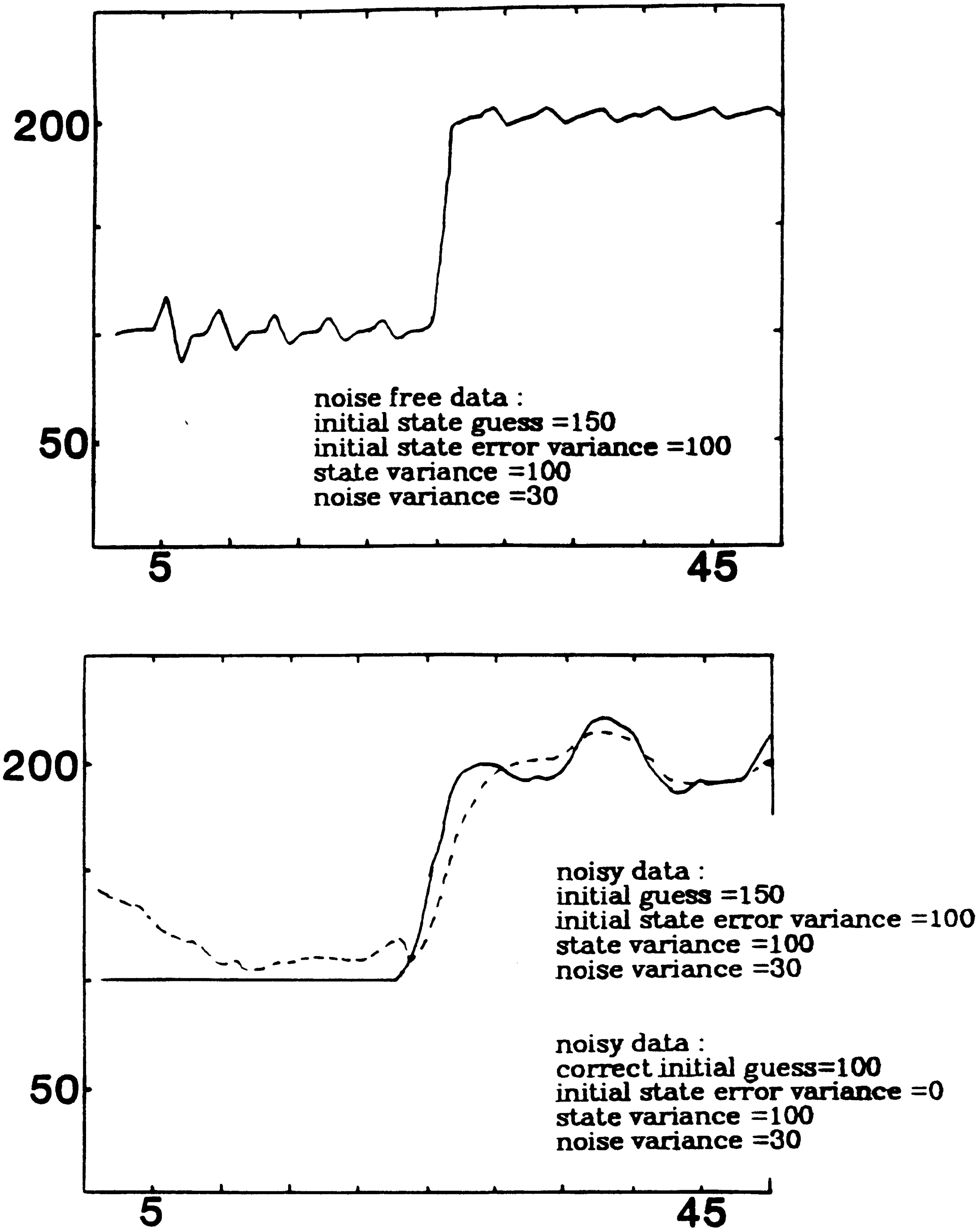

Figure 18 : Output of recursive least squares processing in the case of erroneous initial guesses.
(a) with the noise-free data set. (b) with the noise-corrupted data set.

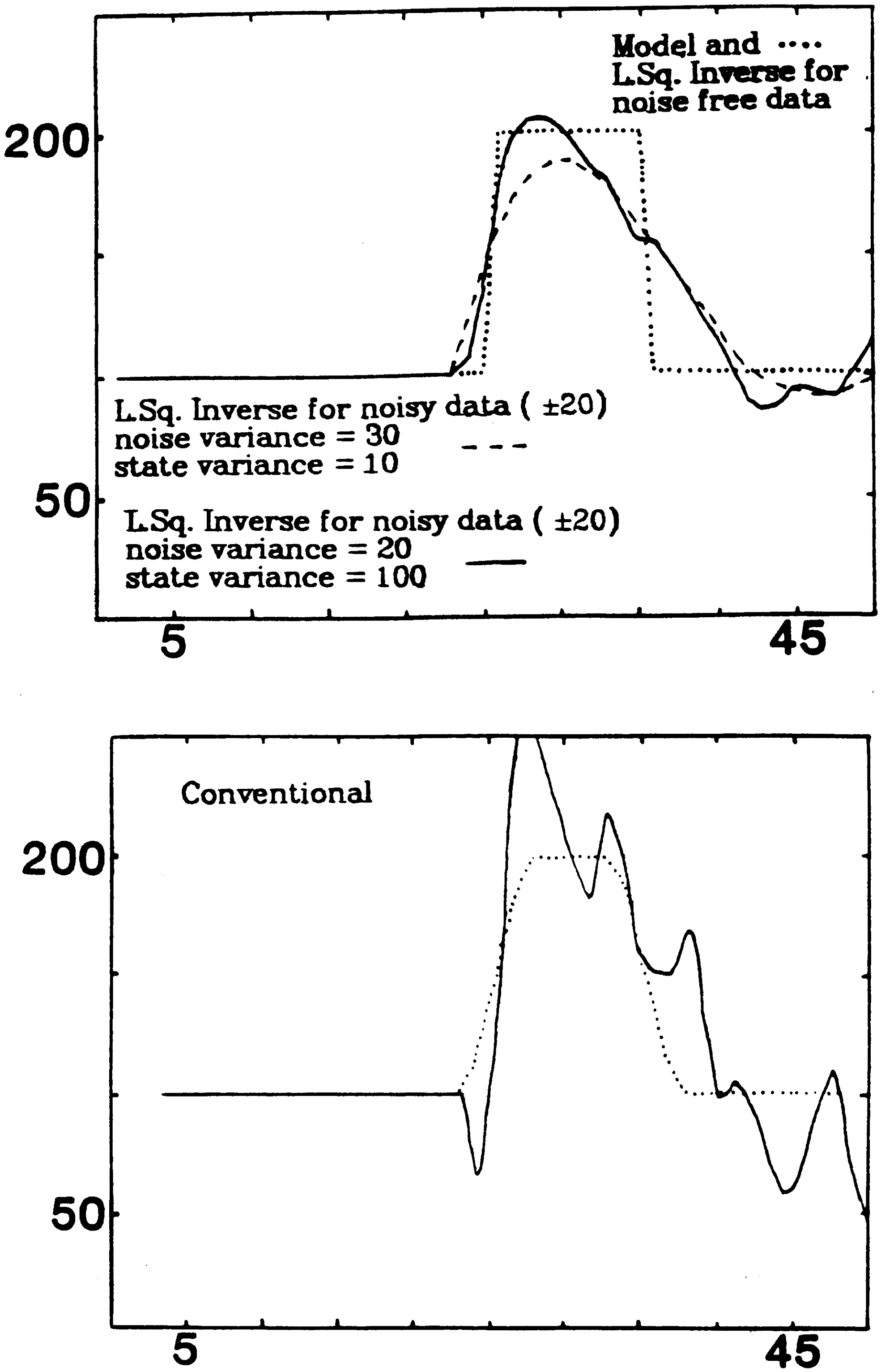

Figure 19 : Results of both conventional and recursive least squares processing for a three layer model. The medium layer is 5' thick.

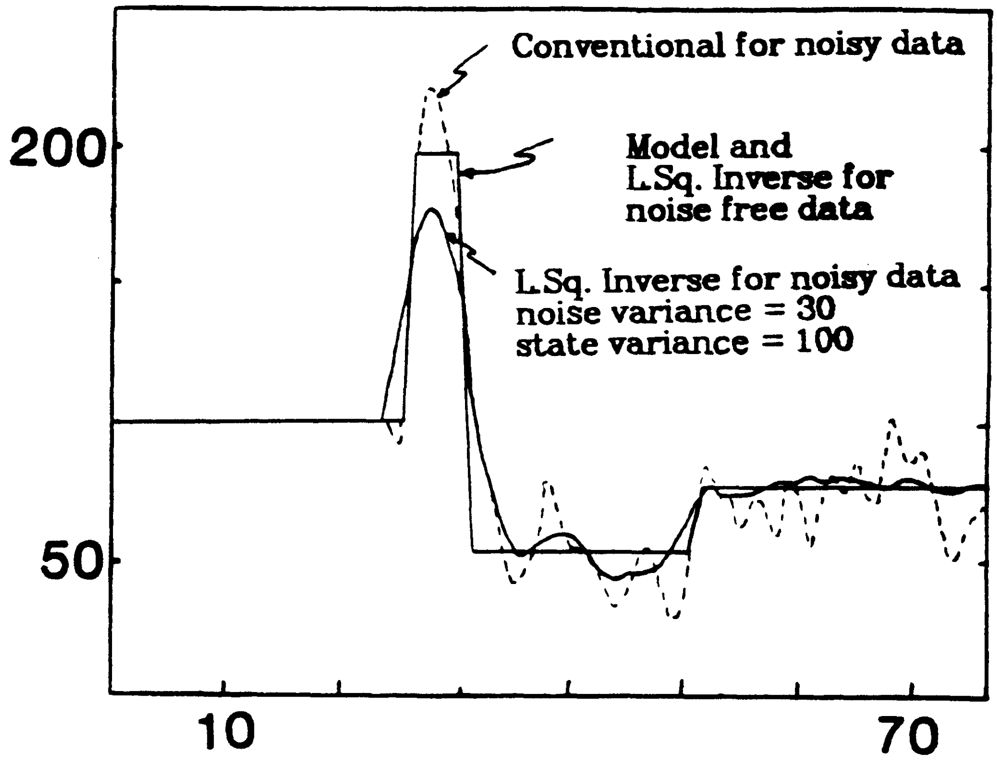

Figure 20 : Results of both conventional and recursive least squares processing for a four layer model. The thinner layer is 2.5' thick.

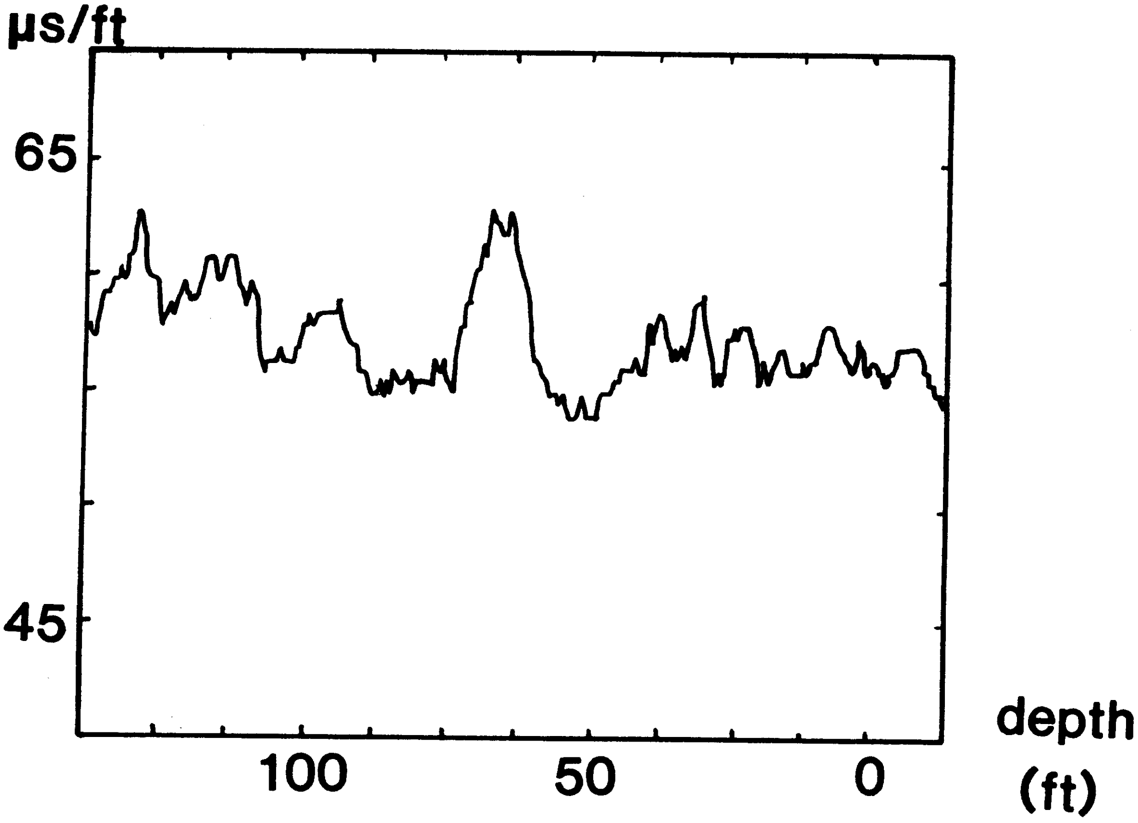

Figure 21 : Arrival time determinations for a 10 foot spacing used as part of the input for the next real data processing examples.

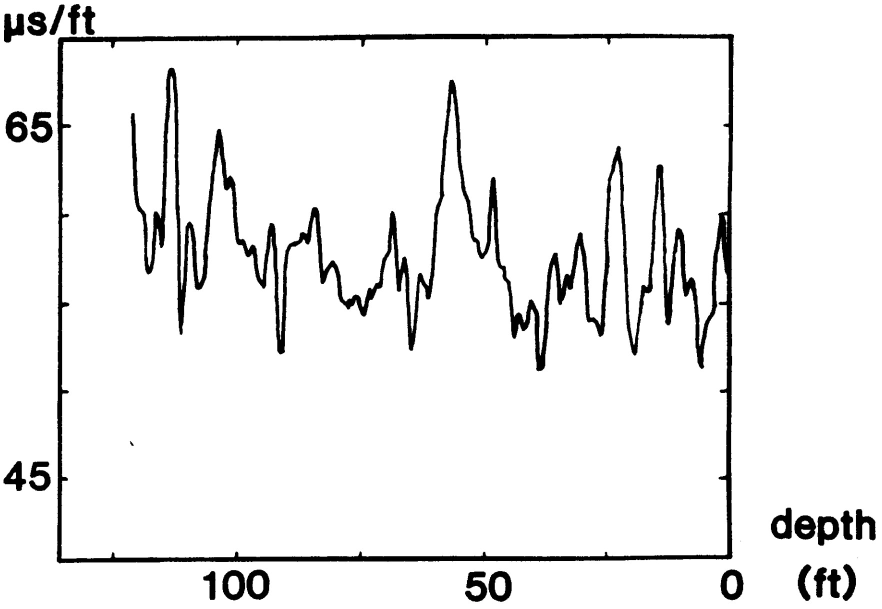

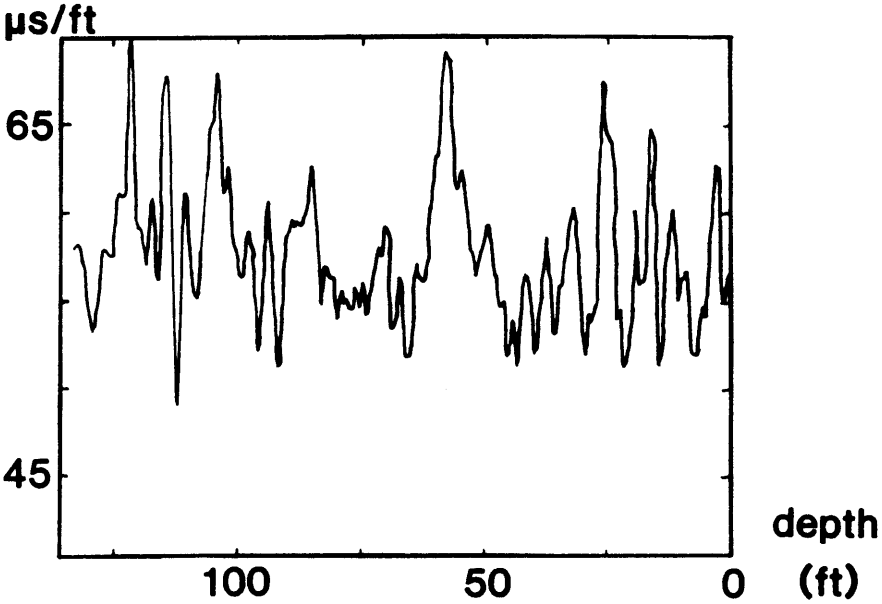

Figure 22 (top) : Conventional processing example on the real data of Figure 21.

Figure 23 (bottom) : Least squares processing of the real data of Figure 21. Q=100 and R=1.

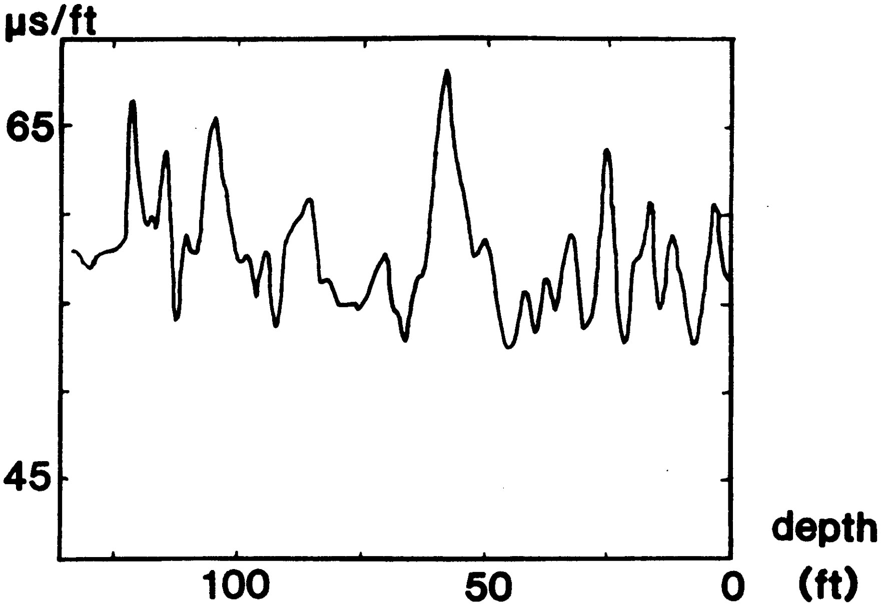

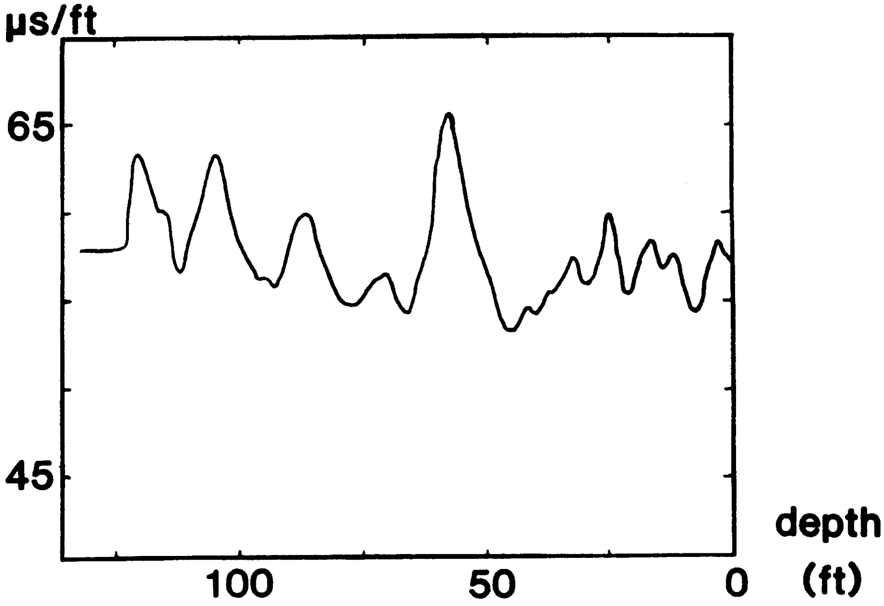

Figure 24 (top) : Least squares processing of the real data of Figure 21. Q=100 and R=10.

Figure 25 (bottom) : Least squares processing of the real data of Figure 21. Q=100 and R=100.

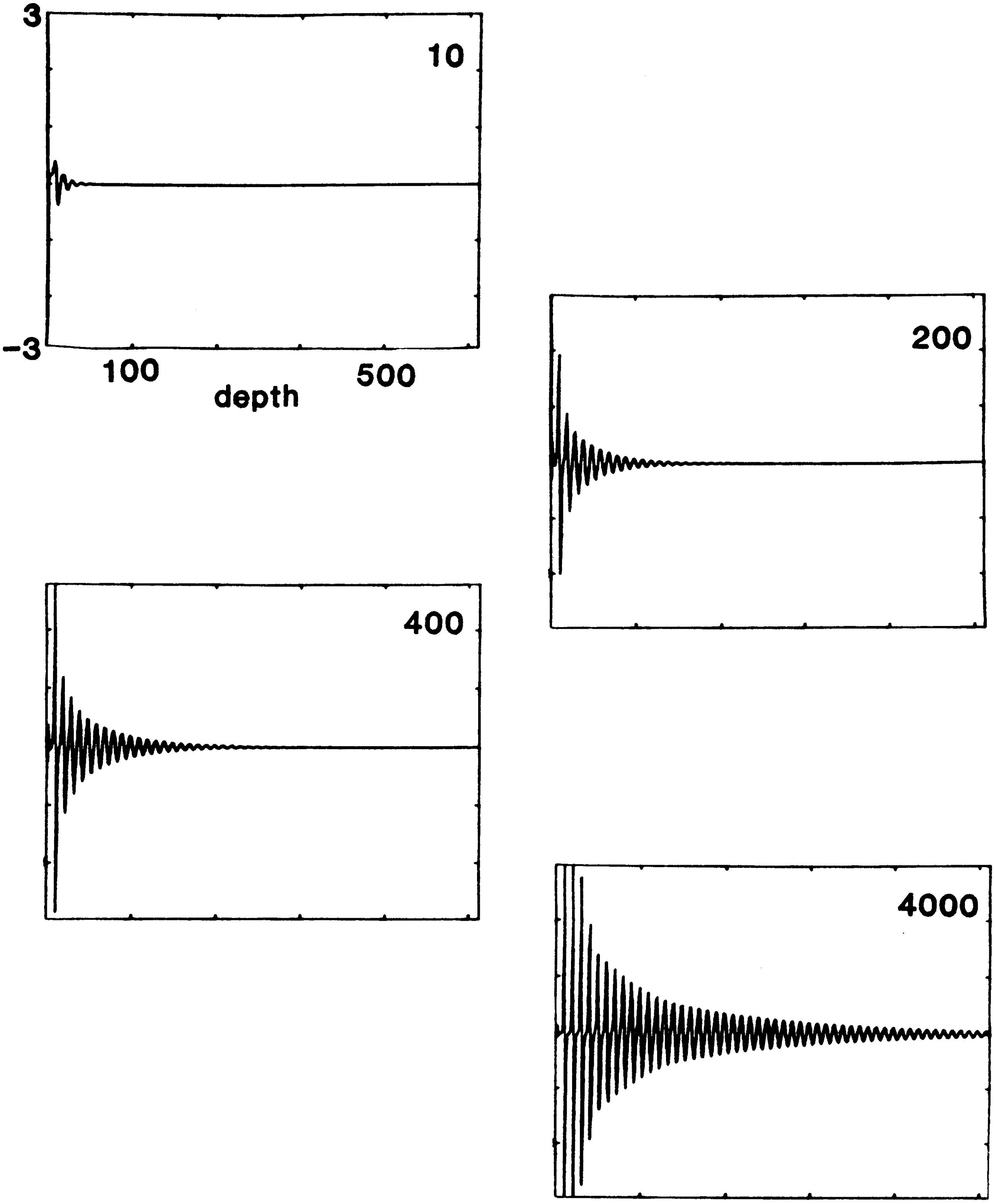

Figure A-1 : Impulse responses of steady-state Kalman filters designed for a tool length of 10 and Q/R values of 10, 200, 400 and 4000.

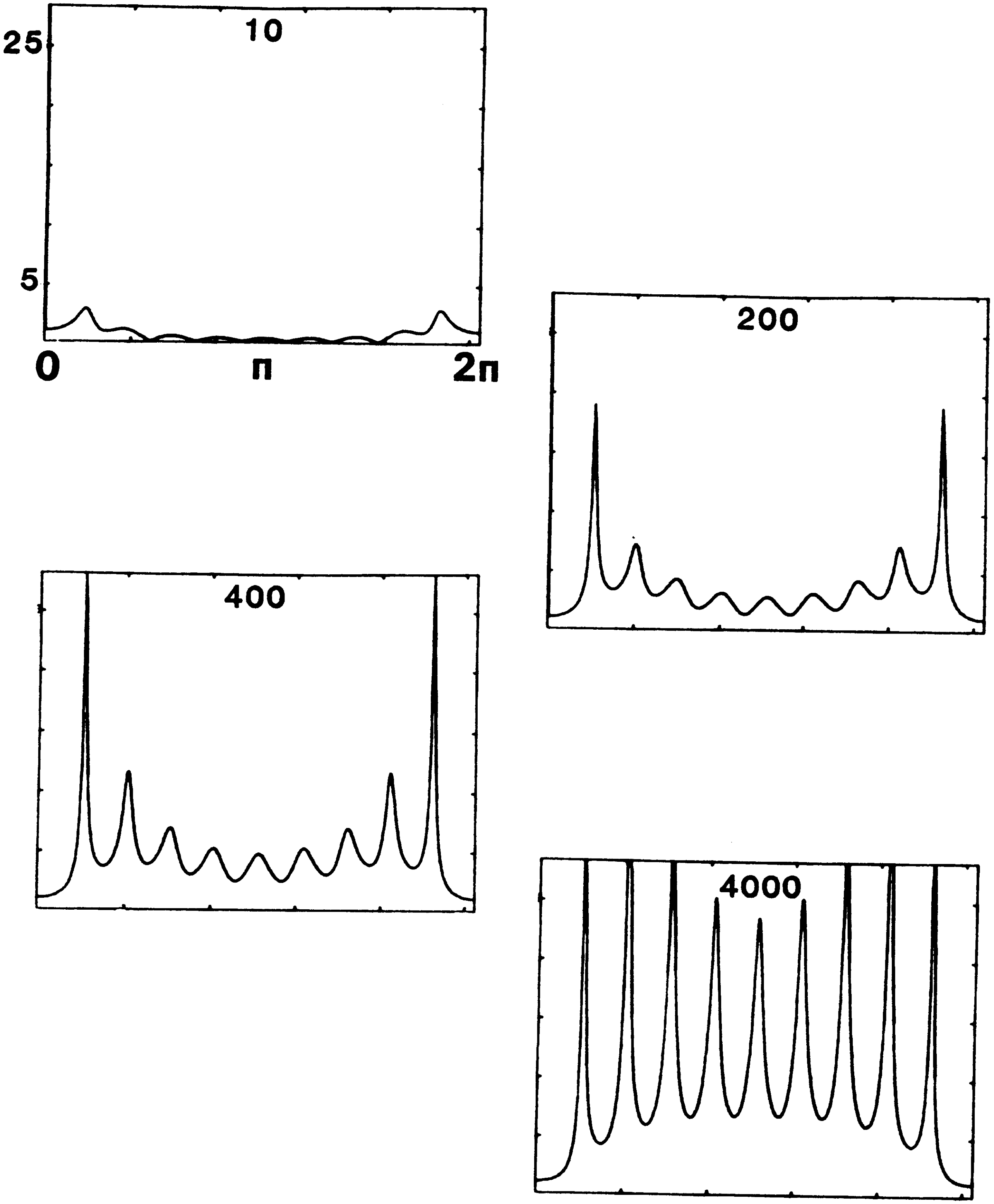

Figure A-2 : Discrete time Fourier transforms of the impulse responses in Figure A-1.

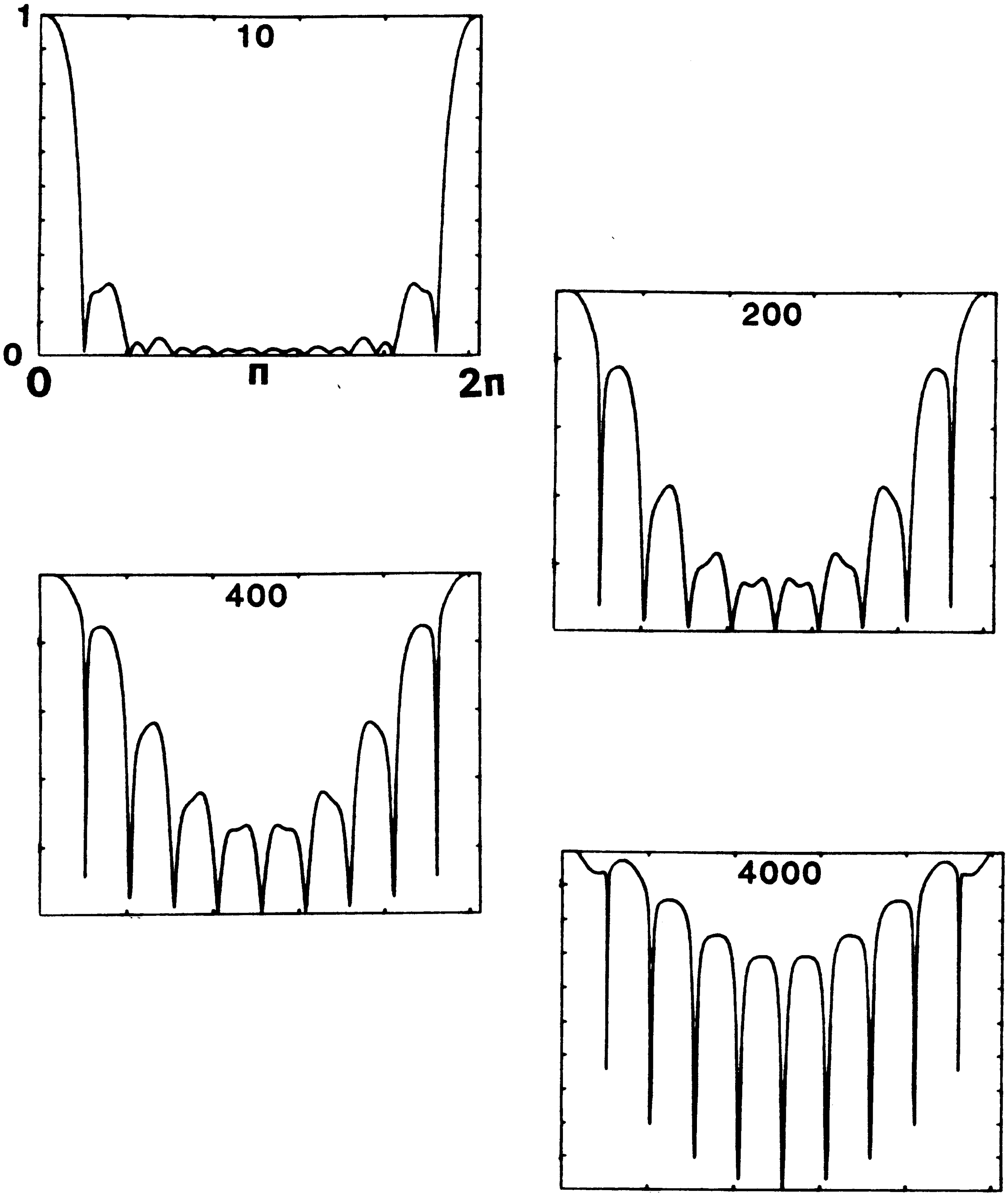

Figure A-3 : Product of the discrete time Fourier transforms of Figure A-2 and the tool response Fourier transform.

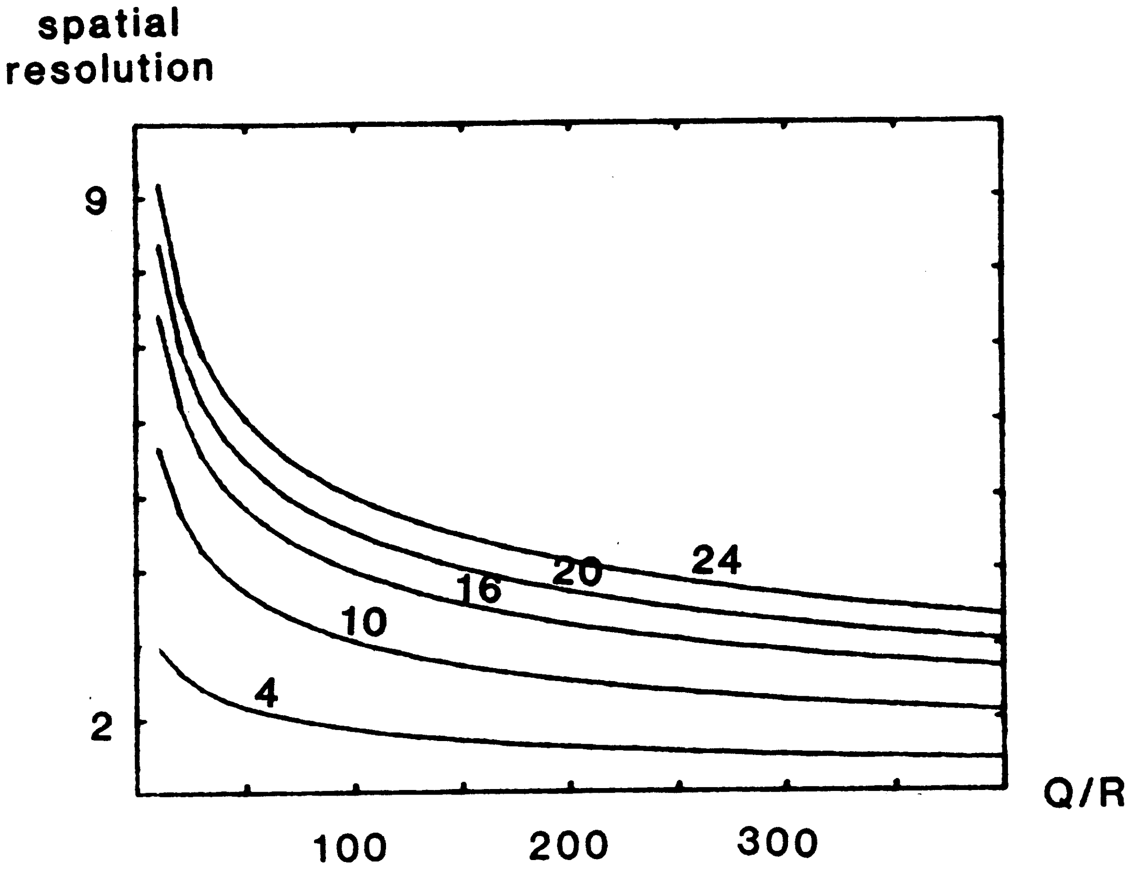

Figure A-4 : Theoretical spatial resolution as defined in text for steady-states filters of length 4, 10, 16, 20 and 24 as a function of the ratio Q/R.

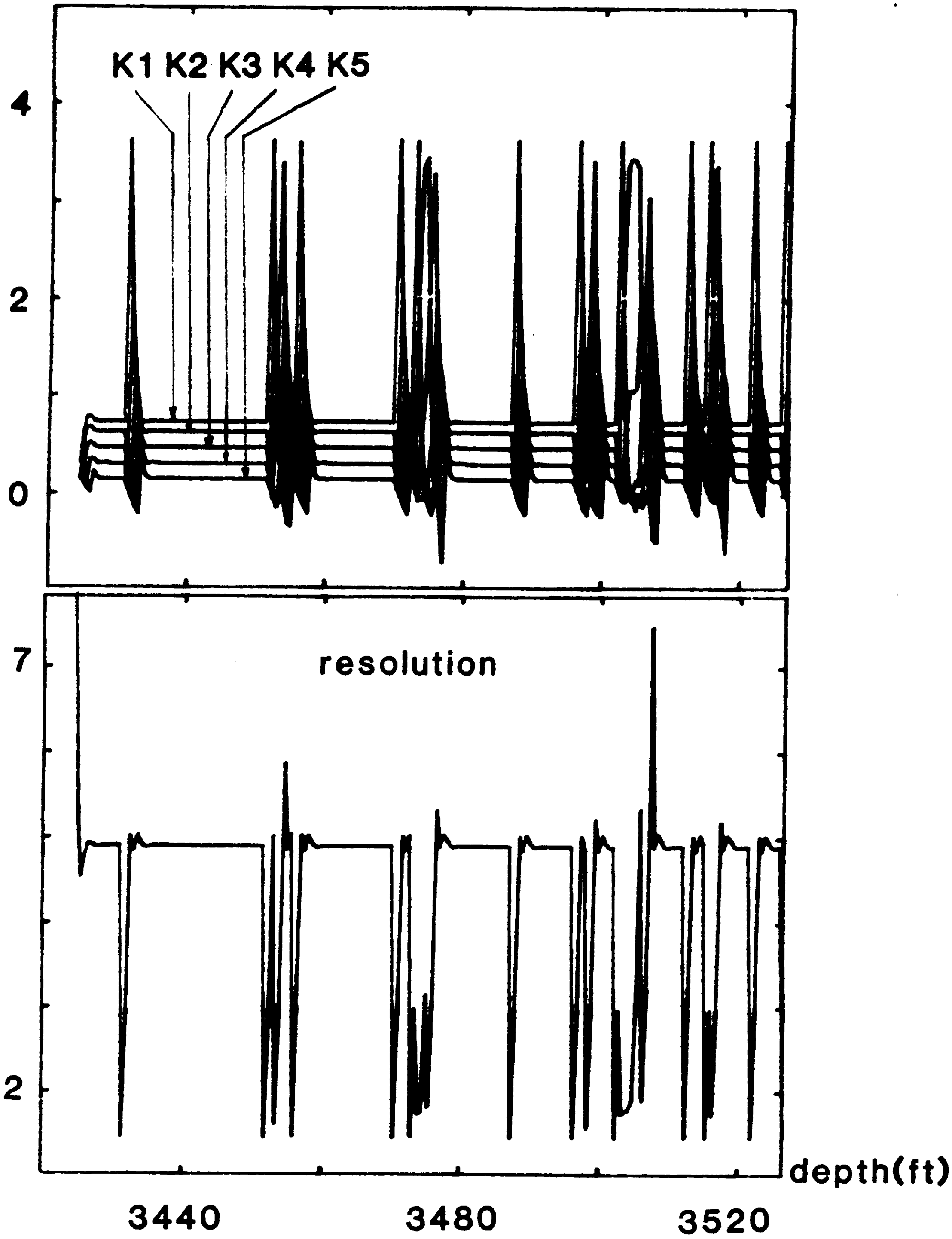

Figure A-5 : The five correction gains corresponding to Figure 11-(c), $K(j)$, are plotted as a function of depth in the top part. The resulting "instantaneous resolution" is displayed in the bottom part.

APPENDIX A :

Spatial resolution for steady-state Kalman filters

In section 2.5 of the text, we mentionned the occurence of a steady state for our inverse filter. Actually, the Kalman filter formulation provides us with theoretical results.

Based upon the properties of the linear system under consideration, namely its *Observability* and *Controllability*, it is possible to conclude the existence of a steady-state filter. Intuitively, observability means that, when the state equation is taken without input noise, one can retrieve the initial state from an exact observation of the system over a finite period of time. Controllability means that it takes a finite period of time to bring the system to any given state through chosen deterministic inputs. Both properties are verified by our single spacing linear system.

Because of the occurence of a steady state, we are able to compare filters for various Q/R ratios in a more general situation.

We first generated impulse responses for Q/R values of, 10, 200, 400 and 4000 for a tool of length N=10. These are displayed Figure A-1. The higher the ratio, the longer the significant part of the impulse response is. Practically, this means that "past" observations bear more importance for the current estimation for higher ratios than for smaller ones. In the limit of high ratios, the impulse response is infinitely long and corresponds to the exact inverse response. In this case, an erroneous start will influence the whole inversion. Another consequence is that the steady state is harder to reach in quick Kalman cases.

The exact inverse impulse response consists of an infinite serie of two $+N,-N$ samples separated by N samples equal to zero. Our impulse responses consist of a succession of peak and trough whose period is 10. Transition between groups of peak and trough is sharper as Q/R is higher.

For completeness, we transformed those impulse responses in the frequency domain. The resulting transforms displayed Figure A-2 shows nine resonances corresponding to the nine poles of the exact inverse for a tool length of 10. As expected, these peaks are finite and all the sharper as Q/R increases. To get an idea of the quality of the inversion we multiplied each of these transforms by the transfer function of the tool. The results are plotted Figure A-3. The exact inverse would yield a constant value of 1 at all frequencies except for null values at pole locations. We see that for a small Q/R ratio, resolution is poor and, once again, as the ratio increases, "resolution" at all frequencies tend to that of the exact inverse.

In order to get a more quantitative idea of resolution in depth, we filtered noise-free data resulting from the simplest model of a sharp interface as in Figure 3 using steady-state gains determined for various Q/R ratios and for various tool lengths. Namely, we took N=4,10,16,20 and 24. We defined the "resolution in depth" as being the number of depth increments that the output would take to reproduce a given transit time contrast extrapolating the steepest rise between two successive samples. These values have been reported Figure A-4 as a function of the Q/R ratio. This figure compares resolutions obtained for different tool lengths at constant firing rate or those obtained for the same tool at different firing rates. Resolution improves very quickly in the range of small Q/R ratios and converges very slowly toward unity at higher values. It is not surprising that longer spacing have more difficulties to improve their "resolution" than shorter ones for a given ratio. However, one should expect a smaller noise content with longer tool than with smaller ones that would enable the former to do a better job in the inversion.

Finally, we may extend this notion of spatial resolution to non steady-state filters. Namely, we define an "instantaneous spatial resolution" by considering the correction gain vector $K(j)$ at each depth increment as one for a steady-state. Consequentely, at each depth we run a filter with these constant coefficients to deconvolve a tool recording for a step formation change. The output yields a value for resolution. In Figure A-5, we plotted the value of each of the gain coefficients at each depth corresponding to the adaptive filter used in Figure 11-(c). The resulting values of "resolution" are displayed in the bottom part of Figure A-5. When starting the filter, resolution decreases rapidly to a value of 5. This part corresponds to the transient state for a filter with Q/R=1. The filter converges quickly toward its steady state. We also note that for such a ratio, the resolution is the same as that of the original field data. This is understandable since variations in the transit time serie and those yielded by error measurement are assumed to be equally likely. Each time the adaptibility criterion triggers an increase in the local Q value, resolution improves and its value suddenly decreases to 1.5, which is close to the theoretical maximum of 1. The former value is even below that for the steady state with Q/R equal to 1000/10 at about 2.1. Afterward, the resulting transient state gives resolution values above those of the steady state for Q/R equal to 1. When, sharp interfaces are closely spaced, the transient state is even more unstable as can be seen in some later sections of the plot.

CHAPTER 4 : SUMMARY

Very finely sampled Full Waveform Acoustic data recorded by the EVA tool revealed unexpected features. These features, related to the stratified structure of subsurface, show that the way from an homogeneous formation as considered in borehole propagation theory to a more realistic earth model is complex. The various modes of propagation are scattered at layer boundaries. Resulting events add energy to the main waveform in a coherent manner so as to produce coherent "oblique events" on iso-offset sections.

Ray modeling of reflections on and transmissions through horizontal layer boundaries proved to be insufficient to account for all observed features. Apparent velocities of some of the "oblique events" were to high to be explained. In addition, body wave conversions at boundaries forced us to consider interfaces that intersect the borehole with an angle.

When modeling such situations, it has been shown that dip angles could significantly increase apparent velocities of "oblique events". Furthermore, advantage of this can be taken to estimate the dip of acoustic interfaces.

After data processing, velocity filtering and separation of events applied to real data iso-offset sections and designed to enhance the "oblique events", the interpretator is able to pick apparent velocities with reasonable accuracy. Results obtained with real data proved to be in satisfactory agreement with the dip-meter data.

Although the azimuth of the dip cannot be determined with present logging tools, such method has the advantage of "sampling" the interface much deeper in the formation than the conventional dipmeters. Typically, with a ten meter offset, acoustic waves can penetrate in the formation as much as two meters. In addition, several events related to the same interface may yield redundancy and improve the quality of the dip estimate. Moreover, in well-bounded cased boreholes dip could be derived with this method, while dipmeters relying on electrical properties fail.

As a result of transmission of acoustic waves through the different layer interfaces encountered on their travel path between source and receiver, travel times are smoothed out. Therefore it may be difficult to estimate the location and amplitude of acoustic contrasts especially in finely-layered geologic units. This problem is even more acute with the longer source-receiver offsets and receiver-receiver spacings used in full waveform logging.

Depth resolution of transit time determinations can be significantly improved when the tool moves between successive shots by increments smaller than its offset. Although an exact solution exists, measurement errors made in determining travel times between source and receiver or moveouts between two common source receivers limit the resolution in depth. In short, noise contamination seriously affects the exact deconvolution process that would remove the tool response.

In addition to multiple travel time or moveout determinations, a stochastic model reasonably representing the statistical behavior of the transit time series can be used to stabilize an inversion for transit times. Such "a priori" knowledge is readily incorporated in a least squares inversion with Kalman's linear dynamic system formalism. In such a formulation, inversion of transit times is implemented in a reccursive algorithm that considerably reduces the amount of storage required to perform a regular least squares inversion of a large section of well data.

This formulation which locates the travel time information as it has been recorded is particularly suited for multi-offset tool data. Moreover, because of the particular formulation choosen, control over the effective resolution in depth is possible. Noise corruption is greater when a fine resolution is sought and inversely. In addition, a data adaptive inversion scheme can be easily implemented in order to locate sharp interfaces without increase of the noise content everywhere else.